LBL--30035

DE91 007647

Kaon Content of Three-Prong Decays of the Tau Lepton*

James Jackson Eastman
Ph.D. Thesis

---

*This work was supported by the Director, Office of Energy Research, Office of High Energy and Nuclear Physics, Division of High Energy Physics, of the U.S. Department of Energy under Contract No. DE-AC03-76SF00098.

Kaon Content of Three-Prong Decays of the Tau Lepton

James Jackson Eastman
Ph.D. Thesis

Department of Physics
University of California, Berkeley, CA 94720
and
Lawrence Berkeley Laboratory,
University of California, Berkeley, CA 94720

December 2, 1990

Abstract

We present a series of measurements involving the production of charged kaons in three-prong hadronic decays of the τ lepton. The data sample was obtained with the TPC/Two-Gamma detector facility at PEP. We set a limit on the branching fraction $BR(\tau^- \to \nu_\tau K^- K^0) < 0.26\%$ at the 95% confidence level. The process $\tau^- \to \nu_\tau K^- K^0$ is related via SU(3) to the second-class current decay $\tau^- \to \nu_\tau \pi^- \eta$. We also present new measurements of the three-prong branching fractions $BR(\tau^- \to \nu_\tau K^- \pi^+ \pi^- + \text{neutrals}) = 0.70\ ^{+0.20}_{-0.17}\%$ and $BR(\tau^- \to \nu_\tau K^- K^+ \pi^- + \text{neutrals}) = 0.16\ ^{+0.10}_{-0.07}\%$.

This work is supported by the United States Department of Energy under Contract DE-AC03-76SF00098.

For Ann.

Acknowledgements

HIGH-ENERGY PHYSICS EXPERIMENTS are great big projects, and I want to express my gratitude to the many scientists, engineers, technicians and programmers who built and ran the PEP4/9 experiment. Without their efforts there would have been no data, and with no data, no thesis.

For their guidance and friendship across the last mumbledy-mumble years let me thank the scientific staff of what used to be called the Kerth Physics Group: my advisor, Roy Kerth; Stu Loken, of the wise thought, the pithy word, and the fine party; Al Clark, who knows everything about the TPC, even when awakened at 3 am; and Bill Wenzel, who'll always offer you another grand design if you didn't like the last one.

The scientific core of this thesis was developed in long consultation with several people, whose contributions I gratefully acknowledge. Bill Moses taught me how to perform an analysis (and later, how to play croquet). Mahiko Suzuki developed the theoretical background for the conclusions of Chapter 5. George Yost (now of the SSC Laboratory) first wrote down the formalism for the Matrix Inversion technique of Chapter 6, and Philippe Eberhard helped me learn how to flesh it out and to interpret my results.

Gerry Lynch, Orin Dahl, Ron Ross, and Mike Ronan taught me a great deal about the way our experiment works. Fred Goozen, Tom Weber, Werner Koellner, Everett Harvey, Jim Dodge and John Waters provided invaluable technical help at every stage. Pat Bronnenberg and Jeanne Miller helped me clear all the bureaucratic hurdles that appeared.

Reading a thesis critically is hard work. Special gratitude is reserved for Ed Wang, Andrea Palounek, and Philippe Eberhard, who examined this thesis in close detail before it was finished, and to Roy Kerth, Gerson Goldhaber, and Selig Kaplan for agreeing to serve on my thesis committee.

One advantage of being in one place so long is that you make a lot of friends. I've enjoyed enormously the lunches and dinners and discussions I've had with mine. Many thanks to Glen Cowan, Lisa Mathis, Hiro Yamamoto, Rem van Tyen, Tim Edberg, Tad Takahashi, Aurelio Bay, Rob Avery, Martin Spahn, Ed Whipple, Ed Wang, Andrea Palounek, Andy Karn, and Linda Yamamoto, for being around.

For their seemingly infinite patience I want to thank my wife, Ann, and my

parents, who never despaired when I admitted that no, I hadn't advanced to candidacy yet, but I was learning all this other interesting stuff instead.

Contents

List of Tables

List of Figures

Chapter 1

Introduction

IN THE STANDARD MODEL of particle interactions, the leptons and the quarks are coupled only by the vector bosons of the electroweak interaction. A charged lepton, in this picture, can decay in one way only: by turning into its associated neutrino and emitting a virtual charged W boson. The W disintegrates into a lighter lepton-neutrino pair or a quark-antiquark pair. The lightest lepton, the electron, has no lighter charged decay products available and is therefore stable. The μ lepton decays to $e\bar{\nu}_e\nu_\mu$ but is too light to decay to hadrons. Thus the τ is the only known lepton heavy enough to decay hadronically.

The decay path $\tau \rightarrow \nu_\tau + hadrons$ offers a unique laboratory for observing details of the weak interaction. It has recently become clear that careful scrutiny of the various hadronic τ decays can give new insight into the couplings of the W to quarks and into the nature of certain mesons, heretofore observed only in hadroproduction experiments. Though much recent work has concentrated on the decays of the τ into one charged particle and assorted neutrals, we shall consider the less common decays to three charged particles, and particularly those rare and little-studied decays in which one or more of the charged decay products is a kaon. These modes will be seen to have bearing on the question of the existence of second-class currents and on the resonant structure of the three-prong system.

Most detectors of charged particles have been built with little or no sensitivity to particle-type. To conventional detectors, charged kaons look exactly like charged pions, and the various three-prong τ decay channels cannot be distinguished. The PEP4/9 detector belongs to a second generation of experiments in which particle identification is important. The investigation of three-prong τ decays which contain kaons is a good match to the PEP4/9 experiment with its current and future data sets. The apparatus' π/K discrimination at high momentum is good enough to distinguish the small kaon populations found in these events, and the present data sample of 147 pb^{-1} is large enough to provide sensitivity to the small ($\sim 0.2\%$) branching fractions involved. Future running promises to yield many hundreds of inverse-picobarns of high-quality data, making invariant mass studies and π^0 analyses possible.

Chapter 2

Phenomenology of Three-Prong Tau Decays

"WHO ORDERED THIS?" asked I.I. Rabi about the μ lepton, the newly-discovered particle that looked just like a heavy electron and was definitely distinct from the greatly anticipated π meson. There was then—and remains today—no obvious reason why there should be a mass-ordered hierarchy of elementary particles, neatly organized in generations that repeat themselves in all fundamental properties except mass. The discovery of the charmed quark in 1974, seeming at first to round out the picture at two complete generations, was followed almost immediately by the discovery of another unexpected item on the menu: the τ, a third lepton.

2.1 The Standard Model of Particle Interactions

The picture of particle interactions that is now known as the Standard Model has as its foundation the unification of the electromagnetic and weak nuclear forces achieved by Glashow [1], Weinberg [2] and Salam [3] in the 1960s. In addition to the description of the electroweak forces in terms of the symmetry groups SU(2) × U(1), the model also incorporates Quantum Chromodynamics (QCD) as a description of the strong interactions, the Higgs mechanism for the generation of particle masses, and Kobayashi-Maskawa generational mixing in the quark sector.

The fundamental fields of the Standard Model are the four electroweak gauge bosons (γ, $W^{\pm}$, and Z^0), the eight gluons of the strong interaction, the conjectured Higgs scalar, and three generations of quarks and leptons. Each generation consists of four left-handed fermions grouped in two weak-isospin doublets, and three right-handed fermions that are weak-isosinglets. Only the doublets couple to the W. Table 2.1 illustrates the generational scheme. The down-type quarks that appear in the weak-isospin doublets of Table 2.1 are not eigenstates of mass; the physical

	Generation			Charge
	1	2	3	
Leptons	$\begin{pmatrix}\nu_e\\ e^-\end{pmatrix}$	$\begin{pmatrix}\nu_\mu\\ \mu^-\end{pmatrix}$	$\begin{pmatrix}\nu_\tau\\ \tau^-\end{pmatrix}$	0 -1
Quarks	$\begin{pmatrix}u\\ d'\end{pmatrix}$	$\begin{pmatrix}c\\ s'\end{pmatrix}$	$\begin{pmatrix}t\\ b'\end{pmatrix}$	$\frac{2}{3}$ $-\frac{1}{3}$

Table 2.1: Schematic view of the generational structure of leptons and quarks.

states are those mixtures of mass eigenstates that couple to the W.

The Standard Model offers no theoretical reason why the number of generations of quarks and leptons in the world should be exactly three (nor does it explain the entire phenomenon of repeated generational structure). Recent experiments [4] have shown that the number of generations with neutrinos lighter than about half the mass of the Z^0 is indeed three. The known neutrinos all have masses that are experimentally indistinguishable from zero; the best limits are [5]:

$$\begin{aligned} m_{\nu_e} &< 18\ \text{eV}; \\ m_{\nu_\mu} &< 250\ \text{keV}; \\ m_{\nu_\tau} &< 35\ \text{MeV}. \end{aligned} \tag{2.1}$$

However, there is also no compelling theoretical reason for all neutrino masses to be zero or even near zero, so one cannot make a firm statement about the total number of generations.

The inability of the Standard Model to explain or predict certain glaringly obvious features of the physical landscape has frustrated the physics community for decades. Nevertheless, no phenomenon has yet been observed that clearly contradicts its predictions. The success of theorists in proposing alternatives and extensions to the Standard Model has been exceeded only by the failure of experimentalists to generate evidence requiring them.

2.2 The Tau in the Standard Model

All available evidence indicates that the τ particle, discovered in e/μ events at SLAC in 1975 [6], is the third-generation sequential lepton, closely related in the Standard Model to the lighter electron and muon. It is produced copiously in e^+e^- collisions with the expected cross section for a massive pointlike particle of unit charge (numerically equal to 136 pb at 29 GeV center-of-mass energy). From the detailed shape of the production cross section near threshold, its spin is known to be $\frac{1}{2}$ [7, 8]. The τ seems not to participate in the strong interaction, and it has no discernible substructure as might be manifested in cross-section distortions at high production energies [9].

The existence of an associated neutrino ν_τ is inferred from the observation of missing momentum and energy in hadronic decays. The nonobservation of neutrinoless decays such as $\tau \to e\gamma$ and $\tau \to \mu\gamma$ [10, 11], together with the strict upper limits on τ production by ν_e and ν_μ beams [12], lead to the conclusion that the τ and ν_τ carry a separately conserved τ lepton number, distinct from the e and μ lepton numbers. The ν_τ itself remains (strictly speaking) undiscovered, in the sense that no direct production reaction of the type $\nu_\tau + n \to \tau^- + p$ has been observed. This experiment is clearly very difficult to perform.

The τ has a weak-decay lifetime of $2.8 \pm 0.2 \times 10^{-13}$ seconds [5], comparable to that of the bottom quark. This corresponds to a lab flight distance $\beta\gamma c\tau_\tau$ of about 700 μm at PEP.

2.3 Decays of the Tau

Unlike the lighter μ lepton, the τ is heavy enough at 1784 MeV to decay not only to purely leptonic systems ($\nu_\tau \bar{\nu}_e e^-$, $\nu_\tau \bar{\nu}_\mu \mu^-$) but also to hadronic states (π^-, ρ^-, K^-, ...). According to the Standard Model, all of the decays of the τ proceed via the emission of a virtual charged W boson. The lowest-order Feynman graphs for these decays are shown in Figure 2.1. The leptonic decay diagram is topologically similar to that governing the decay of the muon to electron and neutrinos, while the hadronic diagram resembles the diagram for leptonic pion decay ($\pi^- \to \mu^- \bar{\nu}_\mu$ via W^-). Thus it is not surprising that the most straightforward τ branching fraction calculations were performed well before the discovery of the τ itself [13].

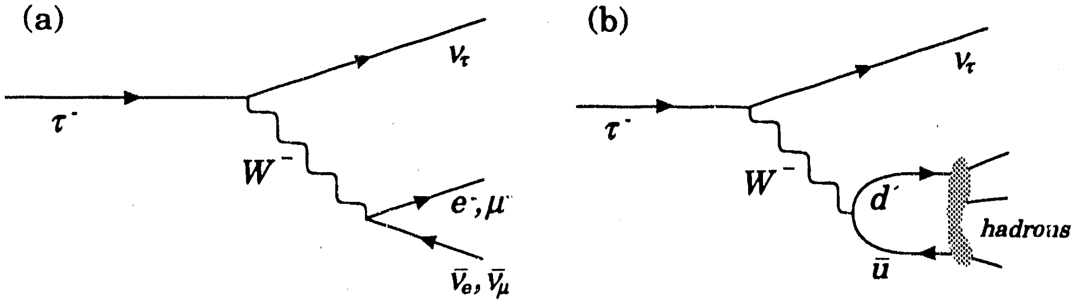

Figure 2.1: Feynman graphs for (a) leptonic and (b) hadronic decays of the τ. The blob refers to the non-perturbative hadronization process.

Table 2.2 gives an overview of the most important known decay modes of the τ. One–prong decays dominate; three–prong decays are also common, but five–prong decays are quite rare, and no higher-multiplicity mode has ever been observed [14].

2.4 Leptonic Tau Decays

The universality of charged-current weak interactions allows a quick estimate of the leptonic and total hadronic branching fractions that is remarkably good. Of the fermion doublets that can couple to the W vertex in Figures 2.1 (a) and (b), two are leptons ((ν_e, e) and (ν_μ, μ)) and three are quarks ((u, d') × 3 colors), the (c, s') and (t, b') doublets being inaccessibly heavy. Thus we estimate each of the leptonic branching fractions $BR(\tau^- \to \nu_\tau e \bar{\nu}_e)$ and $BR(\tau^- \to \nu_\tau \mu \bar{\nu}_\mu)$ to be in the neighborhood of 1/5. A more careful computation, taking account of the τ and

Mode: $\tau \to \ldots$	**Predicted** $BR(\%)$ [15]	**Measured** $BR(\%)$ [5]
1 prong		86.01 ± 0.29
3 prongs		13.19 ± 0.26
5 prongs		0.114 ± 0.027
7 prongs		< 0.019
1–prong modes		
$\nu_\tau \bar{\nu}_e e^-$	18.0	17.7 ± 0.4
$\nu_\tau \bar{\nu}_\mu \mu^-$	17.5	17.8 ± 0.4
$\nu_\tau \pi^-$	10.8	10.6 ± 0.6
$\nu_\tau K^-$	0.7	0.66 ± 0.19
$\nu_\tau \rho^-$	22.7	22.1 ± 1.0
$\nu_\tau K^{*-}$	1.2	1.03 ± 0.28
$\nu_\tau \pi^- \geq 2\ (\pi^0 \text{ or } \eta)$		13.8 ± 1.1
3–prong modes		
$\nu_\tau \pi^- \pi^+ \pi^-$		7.1 ± 0.6
$\nu_\tau \pi^- \pi^+ \pi^- \pi^0$		4.4 ± 1.6
$\nu_\tau K^- \pi^+ \pi^-$	$\sim 0.11 - 0.33$	$0.22\,^{+0.16}_{-0.13}$
$\nu_\tau K^- K^+ \pi^-$	~ 0.4	$0.22\,^{+0.17}_{-0.11}$
5–prong modes		
$\nu_\tau 5\pi^\pm$		0.056 ± 0.016
$\nu_\tau 5\pi^\pm \pi^0$		0.051 ± 0.022

Table 2.2: Some decay modes of the τ.

final state masses, normalized to the measured τ lifetime, and including electroweak radiative corrections yields [15, 16]

$$\begin{aligned} BR_{\mathrm{theor}}(\tau^- \rightarrow \nu_\tau e \bar{\nu}_e) &= 18.0 \pm 1.0 \pm 1.6\%; && (2.2) \\ BR_{\mathrm{theor}}(\tau^- \rightarrow \nu_\tau \mu \bar{\nu}_\mu) &= 17.5 \pm 1.0 \pm 1.6\%. && (2.3) \end{aligned}$$

These agree well with the present world-average measurements of $17.7 \pm 0.4\%$ and $17.8 \pm 0.4\%$, respectively [5].

2.5 Hadronic Tau Decays

Hadronic decays of the τ offer a laboratory of unparalleled cleanliness for observing the coupling of the W boson to quarks. In weak decays of heavy quarks, there are spectator quarks and associated jet particles confusing the picture. In W hadroproduction experiments one has to contend with the underlying event and the lack of kinematic constraints. But in e^+e^- annihilation to τ pairs, one can study the simple Feynman graph of Figure 2.1 (b) exposed and alone.

The rates for certain hadronic τ decays can be calculated from known particle lifetimes ($\tau \rightarrow \nu_\tau \pi$ from τ_π; $\tau \rightarrow \nu_\tau K$ from τ_K). Others can be simply related to isospin-rotated sister processes: $\Gamma(\tau^- \rightarrow \nu_\tau \pi^- \pi^0)$ can be estimated by computing the area under the measured cross section $\sigma(e^+e^- \rightarrow \pi^+\pi^-)$ [15]. These computations are worked out in detail in References [13] and [15].

2.5.1 General properties of the hadronic system

The properties of the hadronic system produced in τ decays are constrained by the simple nature of the diagram of Figure 2.1 (b) and by the couplings of the W. The mass of the hadronic final state must of course be less than that of the τ itself; states involving the charmed quark are inaccessible, as are baryonic states, for although the proton alone weighs less than the τ, the baryon-number-conserving system $p\bar{n}$ does not. The net charge of the hadronic system must match that of the parent τ; therefore the system's isospin cannot be zero. The strange quark couples at the W vertex with a strength dependent on the Cabibbo angle: $s/d = \tan^2 \theta_C$. The total angular momentum J can be 1 or 0, and while the parity P and G-parity G can be either + or −, the combination $GP(-1)^J = +1$ is strongly favored in the Standard Model. States having $GP(-1)^J = -1$ are said to be produced via a *second-class current* [17]; see Section 2.5.4.

The well-studied hadronic τ decays are observed to proceed mainly through the production of mesonic resonances at the W vertex, rather than by multihadron phase space. This is seen clearly in the contributions to the $\pi\pi^0$ final state [5]:

$$\begin{aligned} BR(\tau^- \rightarrow \nu_\tau \rho^-) &= (22.3 \pm 1.1)\% && (2.4) \\ BR(\tau^- \rightarrow \nu_\tau \pi^- \pi^0(\mathit{non\text{-}resonant})) &= (0.30\ ^{+0.30}_{-0.19})\%. && (2.5) \end{aligned}$$

Similarly the three-pion final state appears to proceed via $a_1^-(1260) \rightarrow (\rho\pi)^-$ [18]. We are therefore tempted to assume meson dominance for virtually all hadronic τ decays. It is important to bear in mind, however, that this hypothesis remains untested in many systems and may lead to misleading estimates.

2.5.2 Mesonic decays

The constraints on the hadronic system mentioned in Section 2.5.1 enable us to enumerate the spin-0 and spin-1 mesonic states available to τ decays. Table 2.3 lists some nonstrange meson candidates for τ decay, while Table 2.4 lists several strange candidates. One of the goals of current studies in τ physics is to establish the extent to which these resonances contribute to the observed final states. These measurements are investigations of the mesonic content of the W

Meson	**(formerly)**	$I^G(J^{PC})$	**Final states**	**Comments**
π^-		$1^-(0^{-+})$	π^-	*Important*
ρ^-		$1^+(1^{--})$	$\pi^-\pi^0$	*Important*
$a_0^-(980)$	δ	$1^-(0^{++})$	$\pi^-\eta, (KK)^-$	2^{nd} *class*
$b_1^-(1235)$	B	$1^+(1^{+-})$	$\pi^-\omega, (KK)^-$	2^{nd} *class*
$a_1^-(1260)$	$A_1(1270)$	$1^-(1^{++})$	$(\pi\rho)^- \rightarrow \pi^-\pi^0\pi^0, \pi^-\pi^+\pi^-$	*Important*
$\pi^-(1300)$		$1^-(0^{-+})$	$(\pi\rho)^-$	*Exists?*
$\rho^-(1450)$	ρ'	$1^+(1^{--})$	$(4\pi)^-, \phi\pi^-$	$4\pi, KK\pi$
$\rho^-(1700)$	ρ'	$1^+(1^{--})$	$(a_1\pi)^-, (K^*K)^-, (KK)^-$	$4\pi, KK\pi$

Table 2.3: Some nonstrange meson candidates for τ decay products.

Meson	**(formerly)**	$I(J^P)$	**Final states**	**Comments**
K^-		$\frac{1}{2}(0^-)$	K^-	
K^{*-}		$\frac{1}{2}(1^-)$	$(K\pi)^-$	
$K_1^-(1270)$	Q(1280)	$\frac{1}{2}(1^+)$	$(K\rho)^- \rightarrow (K\pi\pi)^-$	*Admixture*
$K_1^-(1400)$	Q(1400)	$\frac{1}{2}(1^+)$	$(K^*\pi)^- \rightarrow (K\pi\pi)^-$	*Admixture*
$K^{*-}(1415)$		$\frac{1}{2}(1^-)$	$(K^*\pi)^-$	
$K_0^{*-}(1430)$	$\kappa(1350)$	$\frac{1}{2}(0^+)$	$(K\pi)^-$	2^{nd} *class*
$K^{*-}(1715)$		$\frac{1}{2}(1^-)$	$(K\pi)^-, (K\rho)^-, (K^*\pi)^-$	

Table 2.4: Strange meson candidates for τ decay products.

propagator for momentum transfers smaller than the mass of the τ, just as the structure of the photon propagator is elucidated by the observation of resonances among the products of e^+e^- collisions at low center of mass energy. In addition, in some cases the properties of the mesons themselves can be established from their observation in τ decay. Four groups ([19, 18, 20, 21]) have published estimates of the $a_1(1260)$ mass and width based on τ decay data that place it at lower mass and greater width than had been estimated from hadronic production data [5].

2.5.3 Mesonic contributions to $K^-x^+x^-$ decays

Speculation on the origin of kaon-containing three-prong τ decays has been concentrated on a few high-mass mesons. Table 2.5 summarizes the properties [5] of the mesons considered most likely to contribute to the $K^-K^+\pi^-$ and $K^-\pi^+\pi^-$ final states.

Meson	Mass	Width	Decay modes	BR
$K_1^-(1270)$	1270 ± 10	90 ± 20	$K\rho$ ($\rightarrow K\pi\pi$) $K_0^*(1430)\pi$ $K^*\pi$ ($\rightarrow K\pi\pi$) $K\omega$ ...	$42 \pm 6\%$ $28 \pm 4\%$ $16 \pm 5\%$ $11 \pm 2\%$
$K_1^-(1400)$	1401 ± 10	184 ± 9	$K^*\pi$ ($\rightarrow K\pi\pi$) $K\rho$ ($\rightarrow K\pi\pi$) ...	$94 \pm 6\%$ $3 \pm 3\%$
$\rho^-(1450)$	1449 ± 9	220?	4π $\pi\pi$ $\eta\pi\pi$ $\phi\pi$ ($\rightarrow KK\pi$) ...	*seen* *seen* *seen* *seen*
$\rho^-(1700)$	1700 ± 20	235 ± 50	4π *(incl.* $a_1(1260)\pi, \rho\pi\pi$*)* $\pi\pi$ $\bar{K}^*K$+ cc ($\rightarrow KK\pi$) ...	*seen* *seen* *seen*

Table 2.5: Properties of candidate mesons for the $K\pi\pi$ and $KK\pi$ final states.

The broad peak formerly denoted $\rho'(1600)$ now appears [22, 5] to be formed by two broad overlapping excitations of the ρ, called $\rho(1450)$ and $\rho(1700)$. The question of the interference of these two states with each other and with the ρ is unresolved, with conflicting evidence from various experiments investigating different production mechanisms and decay channels ($e^+e^- \rightarrow \pi^+\pi^-$, $e^+e^- \rightarrow 2\pi^+2\pi^-$,

$\gamma p \to 2\pi^+ 2\pi^-$, etc.) The two-kaon final state $K^- K^+ \pi^-$ is reachable either through the $\phi\pi$ decay of the $\rho^-(1450)$ (observed by one group [23]) or through $\rho^-(1700) \to \bar{K}^* K$ or $K^* \bar{K}$. In neither case is the branching fraction measured, though it is clear that both channels are suppressed compared to the dominant 2π and 4π decay modes.

Available theoretical predictions for the branching fraction of the Cabibbo-allowed decay $\tau^- \to \nu_\tau K^- K^+ \pi^-$ are either based on the older single-resonance picture of the excited ρ system (ρ') [24] or are given only in relation to the (unobserved) isospin-related modes $K^- \bar{K}^0 \pi^0$ and $\pi^- K^0 \bar{K}^0$ [15]. In the approach of [24], the ρ' is also supposed to be the most important source of four-pion final states. If the ρ' were responsible for all of the observed $\tau^- \to \nu_\tau \pi^- \pi^+ \pi^- \pi^0$ ($BR = 4.4\%$), arguments of SU(3) symmetry lead one to predict

$$BR(\tau^- \to \nu_\tau \rho' \to \nu_\tau K^- K^+ \pi^-) \simeq 0.6\%. \tag{2.6}$$

However the ARGUS [25] and HRS [26] collaborations have both detected the ω in the four-pion system:

$$BR(\tau^- \to \nu_\tau \omega \pi^-) = 1.5 \pm 0.3 \pm 0.3\%. \tag{2.7}$$

As $\omega\pi$ is not a known branching mode of the ρ', it must be assumed that (2.7) represents a source of four-pion events distinct from the ρ'. Subtracting the $\omega\pi$ contribution yields a revised estimate [24]:

$$BR(\tau^- \to \nu_\tau \rho' \to \nu_\tau K^- K^+ \pi^-) \lesssim 0.4\%. \tag{2.8}$$

Of course the newfound complexity of the $\rho^-(1450)/\rho^-(1700)$ system adds additional uncertainty to this result.

The K_1 mesons (denoted Q prior to 1988) are strange axial vectors. They are known to be quantum-mechanical admixtures of two SU(3) eigenstates belonging to two different meson octets: K_1^a, a member of the $J^{PC} = 1^{++}$ octet containing the $a_1(1260)$; and K_1^b, a member of the 1^{+-} octet along with the $b_1(1235)$ (or "Buddha") meson. $K_1^-(1400)$ couples mainly to $K^*\pi$, while $K_1^-(1270)$ couples mainly to $K\rho$; both of these modes lead to a $K\pi\pi$ final state. In an ideally mixed system (with mixing angle $\theta = 45°$) the lower-mass meson would decouple completely from $K^*\pi$ and the upper from ρK; however the wrong-mode decays are in fact seen, and the mixing angle is found to be in the neighborhood of 55° [27, 28]. The decays of the $K_1^-(1270)$ are complicated by the fact that the meson's mass (1270 MeV) is nearly coincident with the $K\rho$ threshold (1262 MeV). Thus the $K_1^-(1270)$, which in the absence of threshold effects would decay almost exclusively to $K\rho$, actually decays 28% of the time through the low-mass tail of the broad scalar resonance $K_0^*(1430)$ plus a pion, whose combined nominal mass is 300 MeV *higher* than that of the $K_1^-(1270)$ [5].

Tsai [13] makes a prediction for the Cabibbo-suppressed strange axial vector decay $BR(\tau^- \to \nu_\tau K^- \pi^+ \pi^-)$ based on the then-rudimentary (1971) understanding of the $K_1^-(1270)/K_1^-(1400)$ system as represented by a single meson $Q(1313)$. The Das-Mathur-Okubo current-algebra sum rules [29] lead to a relation between the rate for $\tau^- \to \nu_\tau Q^-$ and the well-measured rate for $\tau^- \to \nu_\tau \rho^-$:

$$\Gamma(\tau^- \to \nu_\tau Q^-) = \Gamma(\tau^- \to \nu_\tau \rho^-) \tan^2 \theta_C \frac{m_{K^*}^2}{m_Q^2} \frac{(m_\tau^2 - m_Q^2)^2 (m_\tau^2 + 2m_Q^2)}{(m_\tau^2 - m_{K^*}^2)^2 (m_\tau^2 + 2m_{K^*}^2)}. \tag{2.9}$$

The isospin constraint [15]

$$\frac{1}{3} \le \frac{K^-\pi^+\pi^-}{\text{all } K\pi\pi} \le \frac{2}{3} \tag{2.10}$$

and the uncertainty associated with the existence of two K_1 mesons leads to a range of predictions for the branching fraction [24]:

$$BR(\tau^- \to \nu_\tau K^-\pi^+\pi^-) \simeq 0.11\% - 0.33\%. \tag{2.11}$$

2.5.4 Second-class current decays

Mesons are formed in τ decay as the hadronic condensate of an initial quark-antiquark[1] system:

$$\tau^- \to \nu_\tau + \bar{u} + d \to \nu_\tau + \text{mesons}. \tag{2.12}$$

The hadronization phase of the decay, $\bar{u} + d \to$ mesons, occurs via the strong interaction, so any quantum numbers associated with operators under which the strong interaction is invariant (e.g. P, C) are unaffected by the hadronization phase. Thus the quantum numbers of the final mesonic state are determined at the $W\bar{u}d$ vertex.

The most general spin structure of the weak charged current matrix element connecting free $\bar{u}$ and d fields is (in the notation of [30])

$$\langle u|J_\mu(q^2=0)|d\rangle = \bar{u}\left[\gamma_\mu(f_1 + g_1\gamma_5) + \frac{i\sigma_{\mu\nu}q_\nu}{2m}(f_2 + g_2\gamma_5) + \frac{q_\mu}{2m}(f_3 + g_3\gamma_5)\right] d, \tag{2.13}$$

where $\bar{u}$ and d are quark spinors, q is the momentum transfer, m is the quark mass, and f_1, f_2, f_3, g_1, g_2, and g_3 are coefficients to be determined. In a world without strong interactions, the spin structure of the matrix element reflects the $V - A$ structure of the weak interaction:

$$f_2 = f_3 = g_2 = g_3 = 0; \tag{2.14}$$

$$f_1 = -g_1 = 1. \tag{2.15}$$

The vanishing coefficients of 2.14 can take on nonzero values upon the introduction of strong-interaction corrections to the weak vertex. The lowest-order correction (involving the exchange of one gluon across the vertex) is illustrated in Figure 2.2. These nonvanishing coefficients are said to be *induced* by the strong interaction.

---

[1] This discussion will be simplified by ignoring the existence of the strange quark.

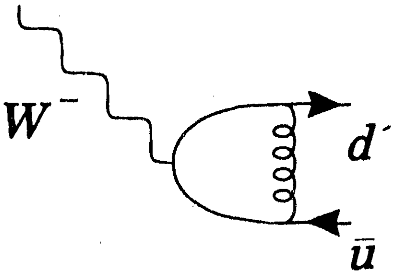

Figure 2.2: Lowest-order strong correction to the quark vertex in hadronic τ decay.

Even allowing for strong effects, however, we expect some of the coefficients to have very small values in the Standard Model. In particular a nonzero value for f_3 would violate the well-established conserved vector current hypothesis (CVC).

We anticipate that in certain cases we will be able experimentally to identify final hadronic states according to their values of the pion-counting quantum number G. We therefore consider the transformation of the six bilinears of Equation 2.13 under the operator $G = Ce^{i\pi I_2}$:

$$\begin{array}{rcll} \bar{u}d & \overset{G}{\rightarrow} & -\bar{u}d & (f_3) \\ \bar{u}\gamma_5 d & \overset{G}{\rightarrow} & -\bar{u}\gamma_5 d & (g_3) \\ \bar{u}\gamma_\mu d & \overset{G}{\rightarrow} & \bar{u}\gamma_\mu d & (f_1) \\ \bar{u}\gamma_\mu\gamma_5 d & \overset{G}{\rightarrow} & -\bar{u}\gamma_\mu\gamma_5 d & (g_1) \\ \bar{u}\sigma_{\mu\nu} d & \overset{G}{\rightarrow} & \bar{u}\sigma_{\mu\nu} d & (f_2) \\ \bar{u}\sigma_{\mu\nu}\gamma_5 d & \overset{G}{\rightarrow} & \bar{u}\sigma_{\mu\nu}\gamma_5 d & (g_2) \end{array} \tag{2.16}$$

The strong interaction is parity-invariant, so we expect the induced coefficients f_2 and f_3 to be related in strength to the dominant vector term f_1, and similarly g_2 and g_3 to the main axial vector term g_1. However, under G–parity the term in f_3 transforms oppositely to those in f_1 and f_2, and the term in g_2 transforms oppositely to those in g_1 and g_3. Therefore to the extent that the strong interaction is invariant under G, the coefficients f_3 and g_2 should vanish. Weinberg [17] characterized these terms, carrying quantum numbers in the combination $GP(-1)^J = -1$, as *second-class.* So far, there has been no convincing experimental observation of any process that proceeds via a second-class current. However the extraction of upper limits on the strengths of second-class currents (based on delicate experiments in nuclear β-decay) has been difficult and somewhat model-dependent [31].

The mesons seen to date in τ decay $(\pi, \rho, a_1(1260), \ldots)$ all carry the quantum numbers of first-class currents. Several authors [32, 31, 33] have pointed out the value of the decays $\tau^- \rightarrow \nu_\tau \pi^- \omega$ (via the axial-vector meson $b_1(1235)$) and $\tau^- \rightarrow \nu_\tau \pi^- \eta$ (through the scalar meson $a_0(980)$) as tests for the existence of second-class vector and axial vector currents. In the Standard Model, second-class currents are present (and CVC is violated) only to the extent that the u and d quarks are nondegenerate in mass. Explicit calculation shows that to lowest nonvanishing order ($\mathcal{O}(\alpha_s)$ and $\mathcal{O}(g_W)$) f_3 and g_2 are suppressed relative to the corresponding first-class induced currents by the ratio of the mass difference between the u and d quarks to their sum [34, 35]:

$$\frac{f_3}{f_2} \simeq \frac{g_3}{g_2} \simeq \frac{m_d - m_u}{m_d + m_u}. \tag{2.17}$$

This relation allows an estimate of the rate for the second-class decay of the τ to $a_0(980)$ [35]:

$$\frac{\Gamma(\tau^- \rightarrow \nu_\tau a_0^-(980))}{\Gamma(\tau^- \rightarrow \nu_\tau \pi^-)} = \left(\frac{f_{a_0}}{f_\pi}\right)^2 \frac{(m_d - m_u)^2}{(m_d + m_u)^2} \left(\frac{m_\tau^2 - m_{a_0}^2}{m_\tau^2 - m_\pi^2}\right)^2, \tag{2.18}$$

where f_{a_0} is the a_0 weak decay constant, defined (by analogy with the pion decay constant f_π) from $\langle 0|J_\mu^{f_3}|a_0(p)\rangle = f_{a_0}p_\mu$. (Here only the scalar, or f_3, term in the hadronic current contributes.) Numerically the branching fraction $BR(\tau^- \to \nu_\tau a_0^-)$ expected from Equation 2.18 ranges from $\lesssim 0.5\%$ (assuming current quark masses) to $\sim 10^{-5}$, with the smaller estimate based on more plausible quark mass assumptions [34, 35]. The second-class axial-vector current decay $\tau^- \to \nu_\tau b_1^-(1235)$ is expected to be present at a similar low level.

These are strong predictions. An observation of either of these decays at an appreciable level could be a signal of a direct non-$(V-A)$ coupling, something not predicted by the Standard Model. Thus the announcement by the HRS collaboration in 1987 that the decay $\tau^- \to \nu_\tau\pi^-\eta$ was present in their data with a branching fraction of 5.1% [36] was met with some excitement (and considerable skepticism). A number of experiments subsequently set stringent limits on this mode (notably ARGUS [37] at $< 0.9\%, 95\%$ CL) that ruled out the HRS claim. (The HRS collaboration itself eventually presented a limit ruling out its earlier measurement.) The analysis of Chapter 5 yields an indirect limit on this mode.

The second-class axial vector current candidate decay $\tau^- \to \nu_\tau\pi^-\omega$ has been observed [25]. The distribution of decay angles in these events is consistent with that expected for the allowed quantum numbers $J^P = 1^-$ associated with a first-class vector current. However with the limited statistics of that measurement no strong limit on second-class decays is possible.

2.6 The One–Prong Problem

Gilman and Rhie [15] first pointed out that there is an apparent discrepancy between the measured one–prong inclusive topological branching fraction of the τ and the sum of measured (and predicted, for unmeasured or poorly-measured modes) exclusive one–prong branching fractions. Table 2.6 summarizes the problem. The sum of exclusive modes is $< 80.2 \pm 1.8\%$, while the inclusive one–prong branching fraction is observed to be $86.0 \pm 0.29\%$; the discrepancy is more than 3σ. The branching fractions called "well-measured" in Table 2.6 are world averages, each representing many experiments. A statistical analysis of the available measurements shows experimental errors are not underestimated on the whole; and while there is some evidence of experimental bias, particularly in the measurements of $BR(\tau \to \nu_\tau\rho)$, there is no reason to believe that this bias is in the direction required to mitigate the problem [39].

The enunciation of the discrepancy in 1985 prompted a flurry of experimental work aimed at measuring and remeasuring the various one–prong branching fractions (see [38] for a histogram of publications by date). Of particular interest have been the modes containing multiple neutral hadrons (π^0, η). Unfortunately these modes, among the most difficult to predict theoretically, are also the most resistant to experimental observation. The limited quality of electromagnetic calorimetry

Decay Mode	**Theory** [38]	**Experiment** [5]
Well-measured modes		
$\nu_\tau \bar{\nu}_e e^-$	18.0	17.7 ± 0.4
$\nu_\tau \bar{\nu}_\mu \mu^-$	17.5	17.8 ± 0.4
$\nu_\tau \pi^-$	10.8	10.6 ± 0.6
$\nu_\tau K^- + (\geq 0 \ neutrals)$	0.7	0.66 ± 0.19
$\nu_\tau \rho^-$	22.7	22.1 ± 1.0
$\nu_\tau K^{*-} \rightarrow \pi^- + neutrals$		0.6 ± 0.1
$\nu_\tau \pi^- \pi^0 \pi^0$	$\leq 6.7 \pm 0.4$	7.5 ± 0.9
Poorly-measured modes		
$\nu_\tau \pi^- (\geq 3\pi^0)$	< 1.4	3.0 ± 2.7
$\nu_\tau \pi^- (\geq 1\eta)(\geq 0\pi^0)$	< 0.8	< 1.3
Sums		
Sum of well-measured modes		78.0 ± 1.7
Theor. limits on poorly-measured modes	< 2.2	
Sum of exclusive modes	$< 80.2 \pm 1.8$	
Inclusive 1-prong BR	86.0 ± 0.29	
Difference	$> 5.8 \pm 1.8$	

Table 2.6: The one–prong problem. Numbers given are branching fractions in %.

available to most experiments makes the isolation of individual modes by photon counting impossible [40]. If one nevertheless allows the current experimental average, $BR(\tau \rightarrow \nu_\tau \pi^- + \geq 2\ (\pi^0 \text{ or } \eta)) = 13.8 \pm 1.1\%$ [5], to be used in place of the theoretical limits on the multiple-neutrals modes, the discrepancy vanishes; one must then explain why the predictions were so wrong.

No present experiment has the calorimetric sensitivity or the large event samples necessary to resolve this question by itself. Reports by individual experiments with modest statistics of internally self-consistent one-prong branching fractions [41, 42] do not solve the problem itself, which belongs to the ensemble of measurements. It remains for high-statistics experiments with excellent calorimetry, such as those proposed for the τ-Charm Factory, to resolve the issue.

The present work is about three-prong decays and makes no attempt to address this subject directly. However we note that many one-prong modes are related by isospin or SU(3) transformations to three-prong states [15]. Measurements of three-prong modes can be used to establish limits on the size of poorly-measured one-prong modes. The analysis of Chapter 5 will be applied in this way.

Chapter 3

The TPC/Two-Gamma Detector at PEP

THE MEASUREMENTS DESCRIBED in this thesis are based upon data taken between 1982 and 1986 with the PEP4/9 TPC/2γ detector at the PEP electron-positron storage ring at the Stanford Linear Accelerator Center. The TPC/2γ experiment is a large multi-purpose particle detector designed to observe long-lived charged and neutral particles over a substantial fraction of the full solid angle surrounding its collision point. With its excellent three-dimensional tracking and particle identification capabilities, the TPC has made important contributions to the study of QCD events, τ decays and two-photon collisions. This chapter outlines the configurations and capabilities of the detector and of the PEP storage ring.

3.1 The PEP Storage Ring

From its turnon in 1980 until its reconfiguration shutdown in 1986, PEP operated at a center of mass energy of 29 GeV and served (at various times) six major high-energy physics experiments at its intersection regions. The PEP storage ring is in a roughly hexagonal tunnel 2.2 km in circumference, located at the end of the two-mile-long SLAC linear accelerator. The linear accelerator delivers electron and positron beams to PEP at 14.5 GeV per beam, their full energy, so PEP need only maintain the beam energy against synchrotron radiation losses. The counterrotating beams are brought together to collide at six positions in the straight sections around the ring. Each of these points is the site of an experimental hall (see Figure 3.1).

In the configuration current during this data-taking, PEP ran with three electron and three positron bunches, each measuring typically 500 μm in the plane of the ring × 50 μm vertically × 1.5 cm in the beam direction. Collisions occurred at a given collision point every 2.45 μs. Typical beam currents of 15–25 μA yielded an instantaneous luminosity on the order of 1.0–2.5 $\times 10^{31}\mathrm{cm}^{-2}\mathrm{s}^{-1}$.

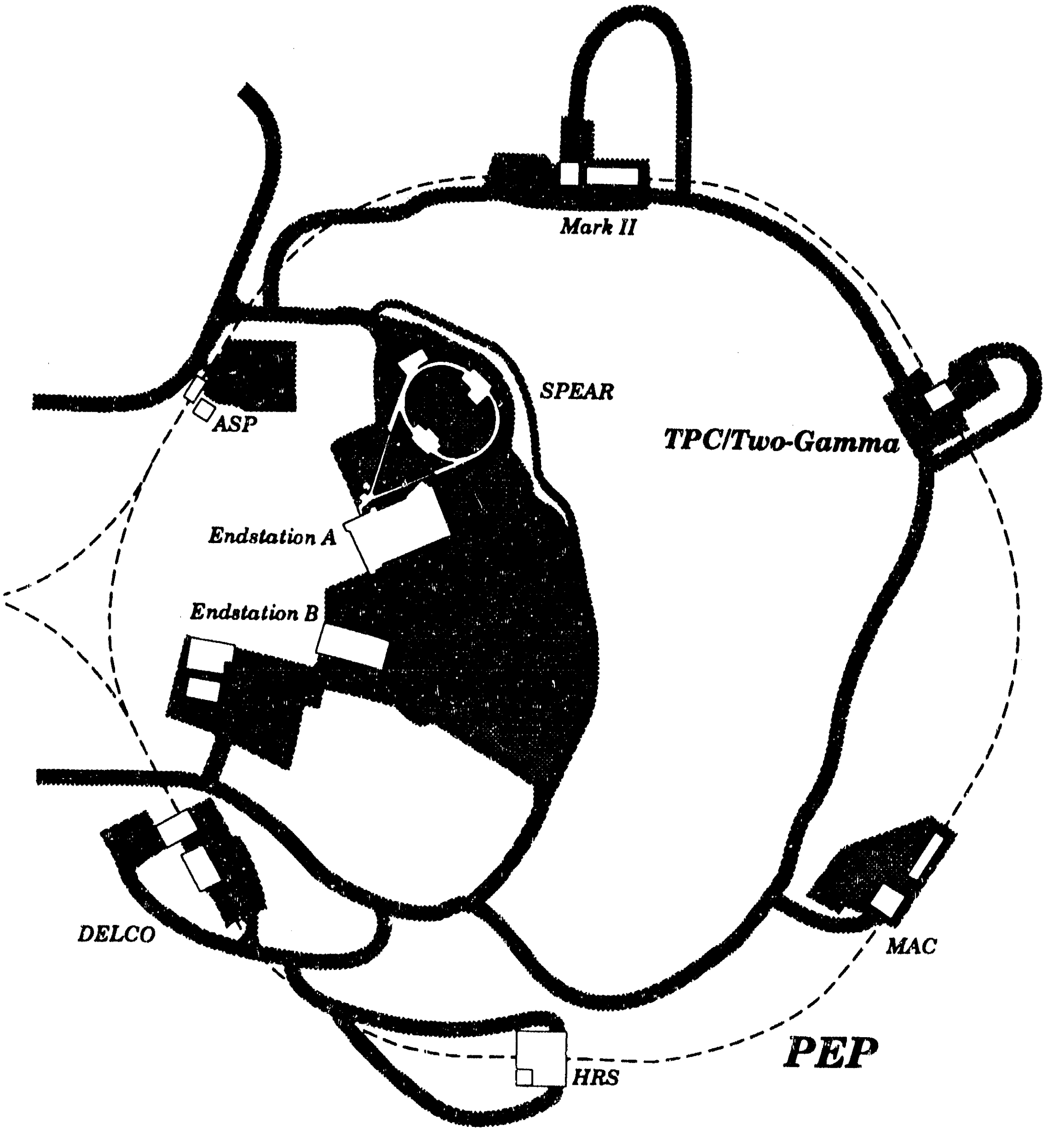

Figure 3.1: Layout of the PEP storage ring.

At this writing PEP has begun a second career in nuclear physics and synchrotron radiation research, as it begins to deliver high-luminosity beams to an upgraded TPC/2γ for a new high-energy physics run. The incorporation of PEP's main competitor, the PETRA storage ring at DESY in Hamburg, into the new electron-proton collider HERA leaves PEP as the only operating accelerator in the 30 GeV energy regime.

3.2 The TPC/Two-Gamma Detector

The second generation of general-purpose particle detectors for e^+e^- accelerators, designed and built in the late 1970s and early 1980s for PEP and PETRA, share a common overall configuration of concentric cylindrical subdetectors: fine tracking at small radii, followed at larger radii by a central tracking chamber extending to about one meter in a solenoidal magnetic field, electromagnetic calorimetry in the barrel and endcaps, and an exterior muon system. While the TPC/2γ detector (also known by its SLAC proposal numbers as PEP4/9) has this general form, it is distinguished by its fully three-dimensional central tracking with particle identification and its low-angle tracking and calorimetry for two-photon physics. The TPC/2γ configuration is illustrated in Figures 3.2, 3.3 and 3.4.

The present analysis relies on measurements made with the central tracking chamber only; we will therefore discuss that device at length, and make only brief mention of the other parts of the detector.

3.2.1 Central Tracking

The most important element of the TPC/2γ detector is its central tracking device, the first large-scale time projection chamber (TPC). TPCs, invented by David Nygren at LBL in the 1970s, have subsequently been built for three large third-generation detectors operating at e^+e^- colliders at higher energy: TOPAZ at TRISTAN, and ALEPH and DELPHI at LEP.

The PEP4 TPC [43] is a large cylindrical drift chamber, 2 m long and 1 m in radius, coaxial with the beam line and centered on the beam collision point. Unlike conventional drift chambers, which have wires throughout their gas volumes, the TPC is nearly empty. All field-shaping wires and sense wires are arrayed on the endcaps. A central membrane is held at a large negative potential with respect to the endcaps (-55 kV). The electric potential is graded by a series of conducting strips at the inner and outer radii, spaced at 5 mm intervals and connected by a precision resistor chain, so that the equipotential surfaces in the gas volume are very nearly planar. A large solenoid just outside the volume maintains a magnetic field parallel to the electric field. The magnetic field was 4.0 kG in the 1982-83 running, and 13.25 kG after 1986.

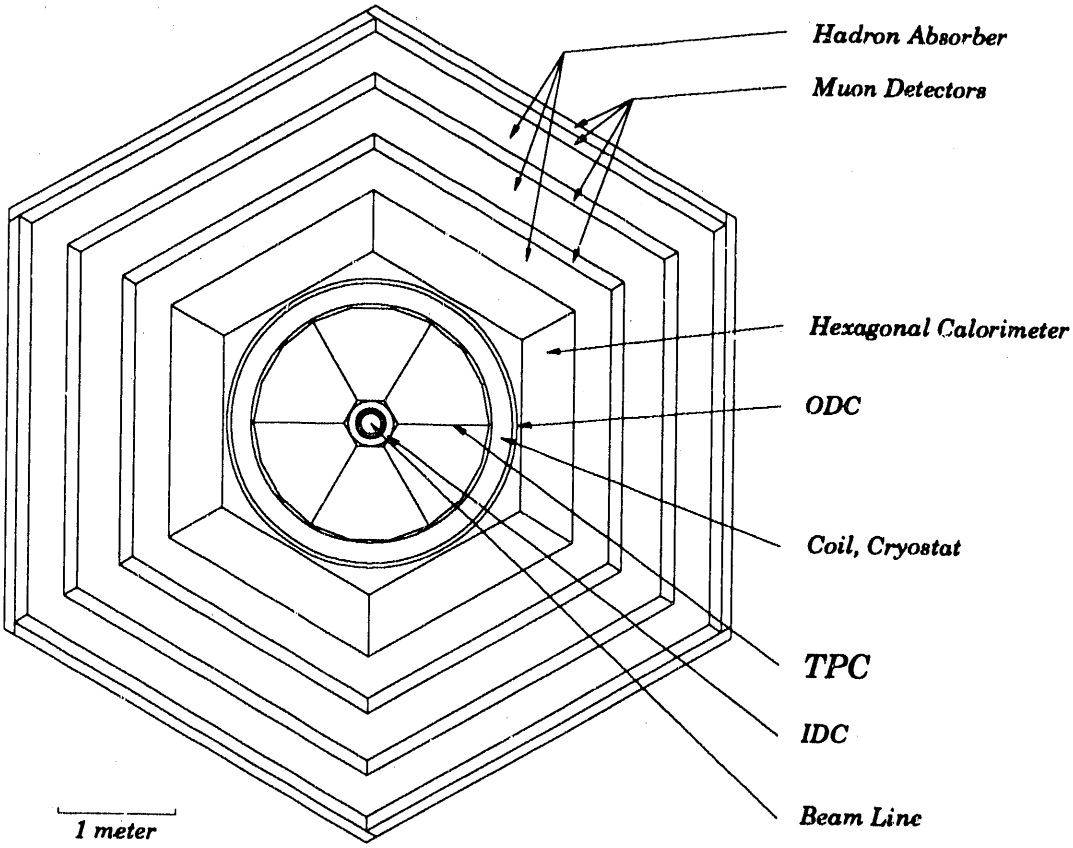

Figure 3.2: Cross-sectional end view of the central region of the TPC/2γ detector. The view corresponds to a slice taken perpendicular to the beam line and containing the beam intersection point. Major detector elements not visible in this view include the Pole Tip Calorimeters and the forward detectors.

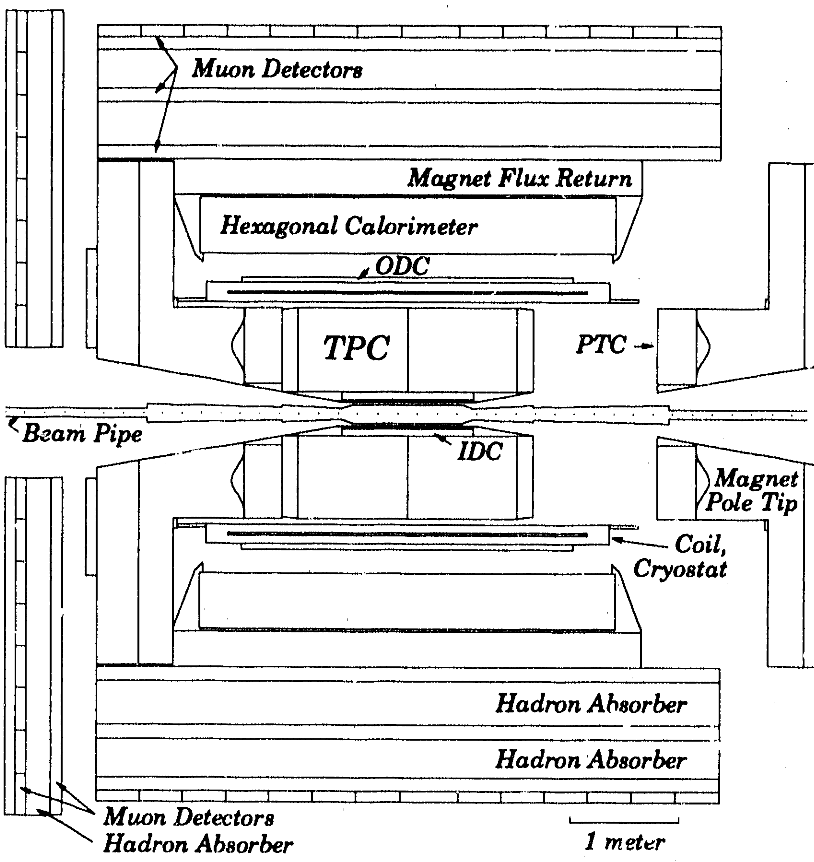

Figure 3.3: Cross-sectional side view of the of the TPC/2γ detector. The view corresponds to a vertical slice containing the beam line. The forward detectors are not shown.

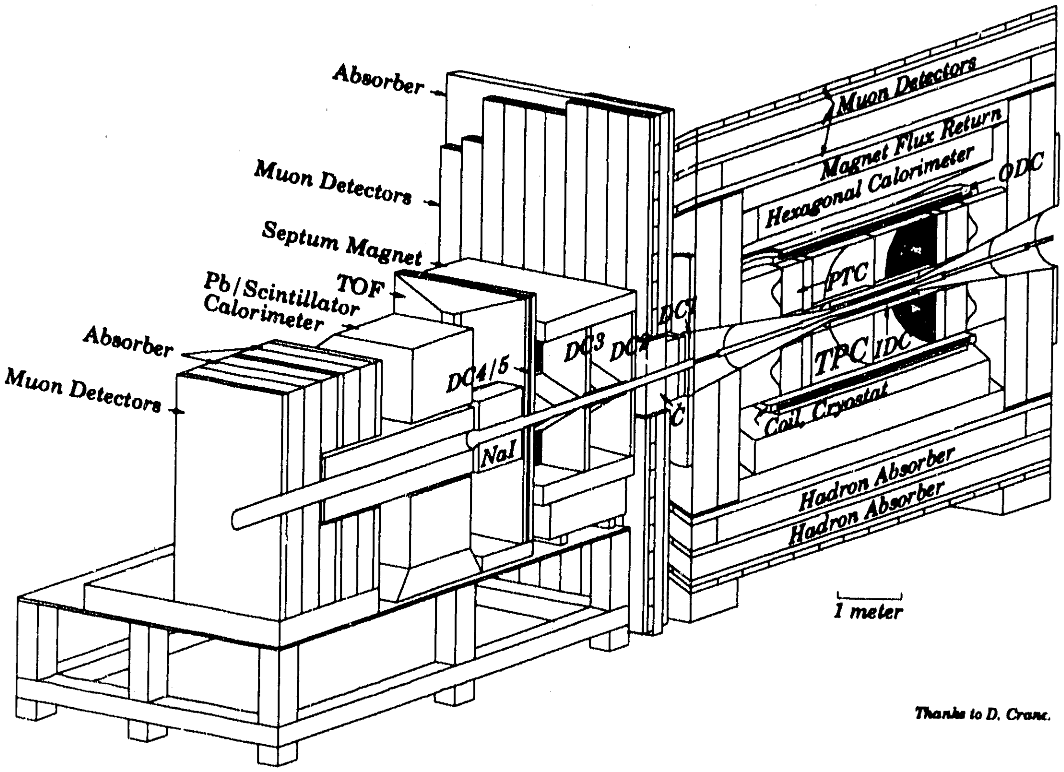

Thanks to D. Crane.

Figure 3.4: Perspective cutaway view of the of the TPC/2γ detector. One-half of the detector has been removed, and only one arm of the forward detector array is shown. The usual little man is omitted.

When a charged track traverses the sensitive volume, it ionizes molecules in the gas (80% argon, 20% methane at 8.5 atmospheres) and leaves a trail of electron-ion pairs in its wake. The strong electric field accelerates the electrons quickly to an asymptotic drift velocity of 3.3 cm/μs, and they drift together along the electric field lines to the endcap, holding the three-dimensional shape of the track. The parallel magnetic field serves not only to bend the primary track so that its momentum may be measured, but also to limit the transverse diffusion of the ionization clusters over their long drift.

The drifting ionization clusters are detected at the endcaps on multiwire proportional chambers called *sectors.* Each sector covers 60° of azimuth on one endcap, and contains 183 sense wires running perpendicular to a radial line drawn from the beamline through the sector's center. The sense wires, 20 μm in diameter, are set 4 mm apart and alternate with 75 μm field-shaping wires. Centered under 15 of the wires lie rows of 7.0 mm × 7.5 mm cathode pads; see Figure 3.5.

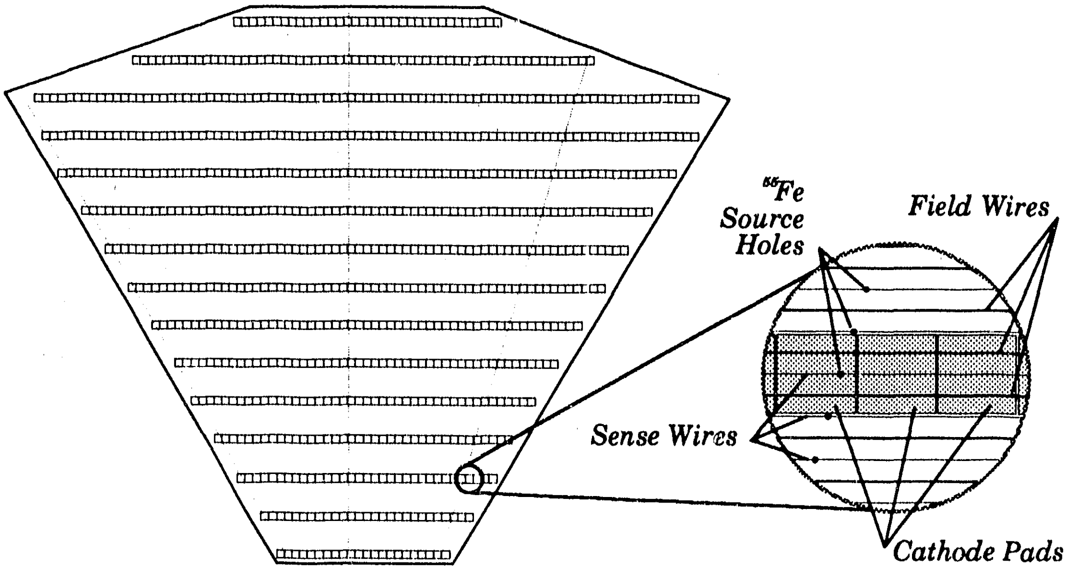

Figure 3.5: A time projection chamber sector. The inset shows the placement of the sense and field wires and the cathode pads in a representative area.

The electric field, constant across the drift volume, rises sharply as the ionization clusters approach the thin sense wires. The accelerated drift electrons themselves ionize gas molecules near the wires and initiate an *avalanche.* In this way a small cluster of drifting electrons can induce a detectable signal on a wire. When a padrow lies behind the wire, the signal is capacitively coupled to the pads nearest the avalanche. In this case, the detector can measure not only the radial location of the ionization cluster (from the padrow hit) but also the azimuthal location (from the centroid of pad hits). The arrival time of the signal, relative to a beam-crossover signal sent by the accelerator, is also recorded. Since the drift velocity is known, the arrival time yields a measurement of the third coordinate of the ionization cluster (the coordinate in the drift direction) for beam-related tracks. In this way, the TPC images tracks in three dimensions. (Most conventional detectors have very poor resolution along the beam direction.) The spatial measurement in the plane of the sectors has a resolution of 150 μm, limited by transverse diffusion. The resolution in the drift direction is 180 μm, limited by knowledge of the drift velocity.

Particle Identification by $\mathrm{d}E/\mathrm{d}x$

The TPC electronics record not only the time of arrival of each pad and wire hit, but also the pulse height. The size of the avalanche signal is proportional to the number of primary electrons released in the original ionization cluster, which is itself proportional to the rate at which the track lost energy to ionization as it traversed the gas. The ionization energy loss rate is called $\mathrm{d}E/\mathrm{d}x$.

At the molecular level, ionization energy loss is not continuous. The process is characterized by frequent collisions in which little energy is transferred to molecular electrons and by rare events with large energy transfers. Successive measurements of $\mathrm{d}E/\mathrm{d}x$ for a track of a given energy traversing a given medium are drawn from a *Landau distribution*, featuring a long tail of high energy losses extending far above the most-probable value (Figure 3.6). Each track in the TPC yields up to 183 measurements of $\mathrm{d}E/\mathrm{d}x$ drawn from such a distribution, each corresponding to the track's traversal of the thin slab of gas monitored by one sense wire. In order to avoid undue dependence on measurements from the fluctuating Landau tail, the TPC analysis uses as a figure of merit the mean of the smallest 65% of ionization measurements. References to $\mathrm{d}E/\mathrm{d}x$ measurements for TPC tracks in most publications should be understood to refer to this truncated mean. The TPC measures $\mathrm{d}E/\mathrm{d}x$ with a fractional resolution of 3.5%–6%, depending on the number of wire samples contributing to the measurement. Wire samples can be lost or rejected if the track is at a high dip angle or near a sector boundary, or if ionization clusters from other nearby tracks confuse the pulse-height measurement.

The mean $\mathrm{d}E/\mathrm{d}x$ for a track passing through a given medium is a function only of its speed, or more precisely, of the relativistic parameter $\eta \equiv \beta\gamma$. Figure 3.7 shows the dependence of $\langle \mathrm{d}E/\mathrm{d}x \rangle$ on η in TPC gas. η is not a measured quantity, but the track momentum p is measured from the curvature of the track in the TPC's magnetic field. Since $\eta = p/m$, where m is the particle's mass, we can redraw Figure 3.7 as a function of $\ln(p)$ by plotting a family of curves corresponding to the stable, observable particles, each offset from the original curve by $-\ln(m)$. These curves are shown in Figure 3.8, along with measured points from the TPC. The masses used to plot the theoretical curves are those of the electron, muon, pion, kaon and proton; in addition one can see in high-statistics data sets another band made up of deuterons ejected from the beam pipe. From Figure 3.7 it is clear that (away from the regions of ambiguity, called *crossovers*) simultaneous measurements of momentum and $\mathrm{d}E/\mathrm{d}x$ suffice to select the mass of a particle,

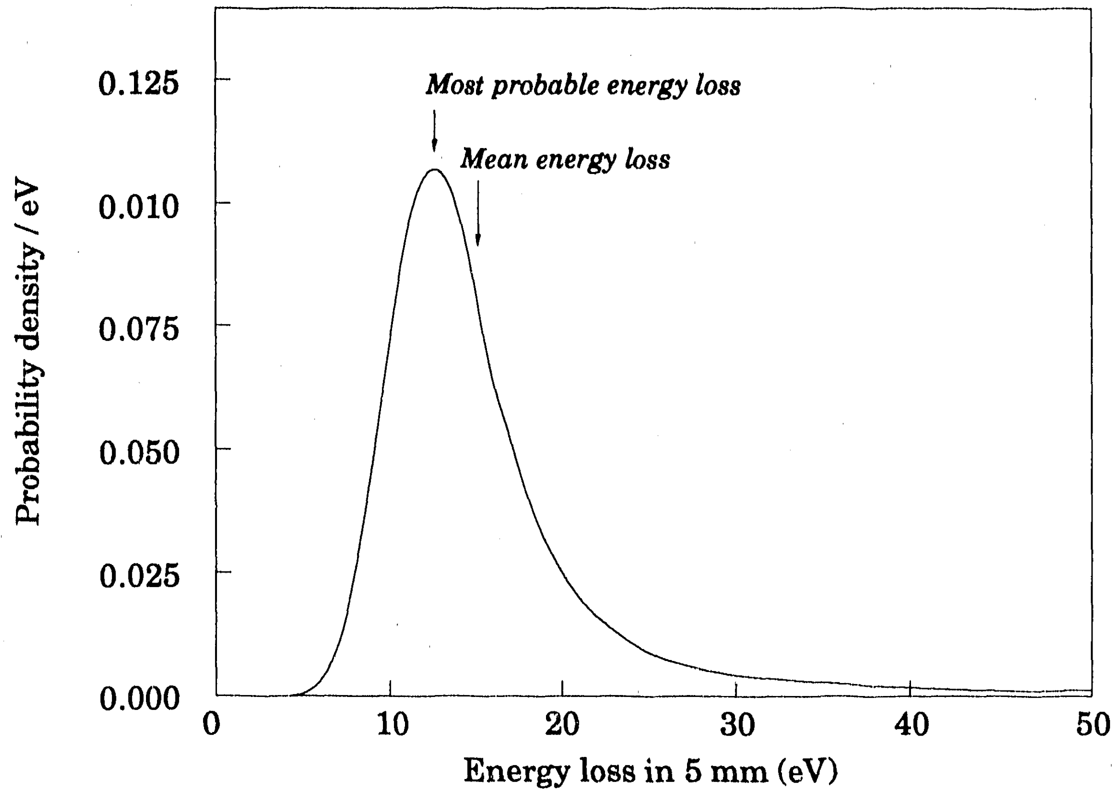

Figure 3.6: The Landau distribution. Shown is the energy loss distribution for a particle with $\beta = 0.96$ traversing 5 mm of TPC gas at 8.5 atm.

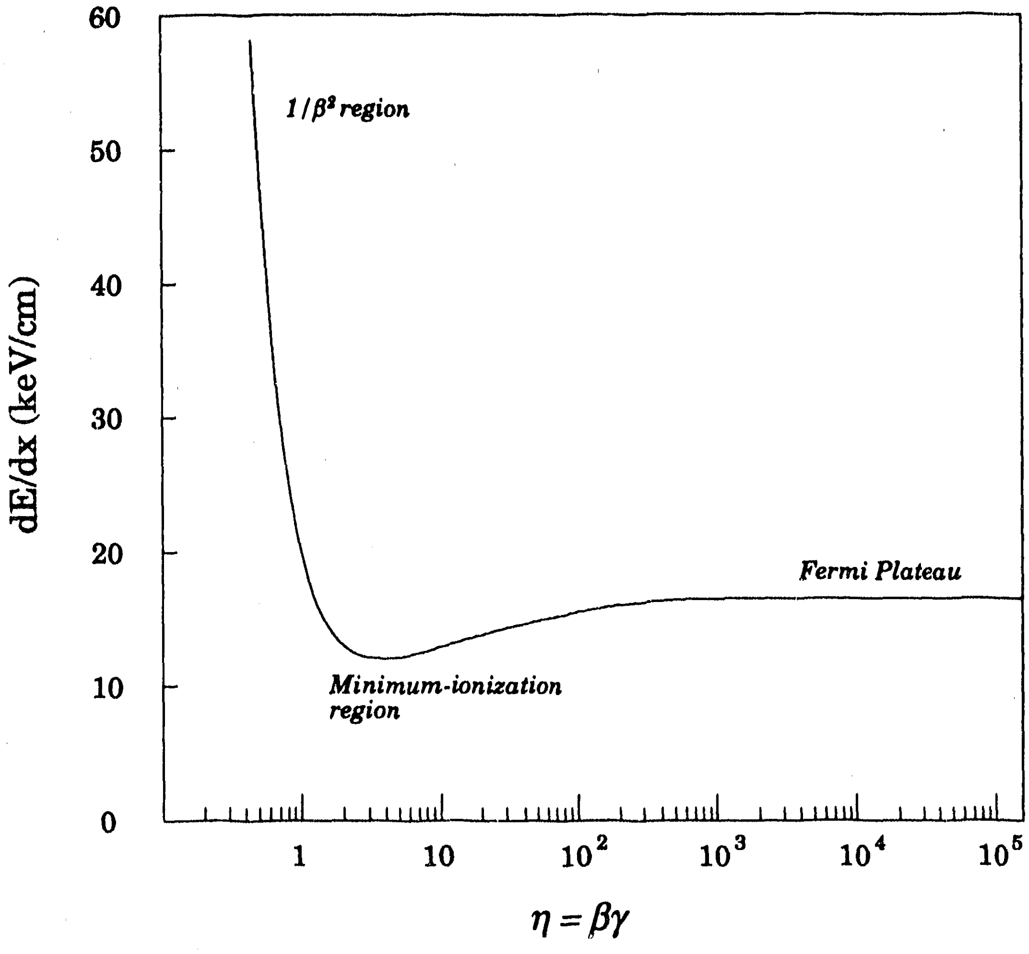

Figure 3.7: Dependence of $\langle \mathrm{d}E/\mathrm{d}x \rangle$ on η in TPC gas.

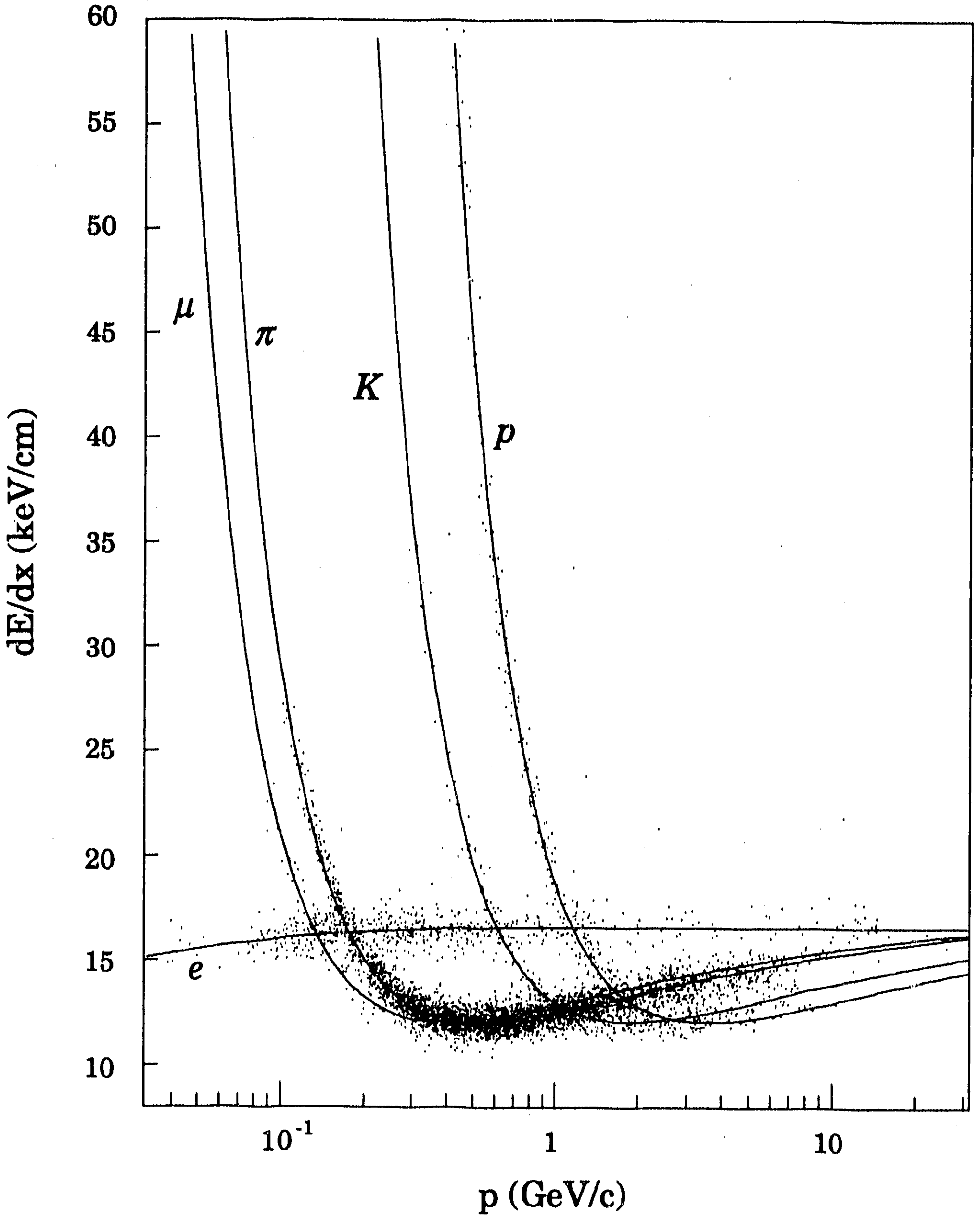

Figure 3.8: Observed and expected loci of $\langle \mathrm{d}E/\mathrm{d}x \rangle$ as functions of track momentum for a small sample of QCD events in the TPC.

and therefore its species, from a short list of possibilities. This ability to identify particle types from tracking data only makes the TPC/2γ device unique among detectors of its generation.

Upgrades to the TPC

When the TPC was first turned on in 1981, it was immediately clear that the reconstructed tracks in the TPC were strongly non-helical. The buildup of positive ions locally along the inner and outer field cages and near the sectors was causing distortions on the order of centimeters in the drifting track images. Although the worst of the distortions could be removed in the analysis software (and by the judicious application of copper tape to the field cages), the TPC's momentum resolution suffered. Of more serious impact on the momentum resolution was the failure in early testing of the proposed 15 kG superconducting coil. An aluminum 4 kG conventional coil was used for the 1982-83 running period. In this configuration, the TPC achieved a momentum resolution of $(\sigma_p/p)^2 = (6\%)^2 + (3.6\% \times p(\mathrm{GeV/c}))^2$.

A group of upgrades to the detector was installed during the 1983-84 hiatus. The inner field cage and pressure wall were rebuilt using lighter materials, reducing the amount of material between the interaction point and the TPC's sensitive volume. A resistive coating was applied to the field cages, preventing charge buildup. In addition, an additional wire plane or "gating grid" was installed on each sector. The voltages on the gating grid are switched to make it transparent to drifting charge only when a pretrigger signal has indicated the presence of tracks in the TPC volume; the rest of the time, the gated grid is opaque to charge, preventing positive ions from the avalanche region from drifting into the main volume.

During the same shutdown period, a new 13.25 kG superconducting coil was installed. The 1984-86 TPC, with its higher magnetic field, thinner inside wall, and controls on ion buildup, achieved a substantially improved momentum resolution of $(\sigma_p/p)^2 = (1.5\%)^2 + (0.065\% \times p(\mathrm{GeV/c}))^2$.

In the chapters that follow, data from the 1982-83 running period will be referred to as the *low-field* data set, and the 1984-86 set will be called the *high-field* set. The PEP4/9 experiment accumulated 77 pb^{-1} of data in the low-field configuration, and 70 pb^{-1} in the high-field. The current run (1989-) is optimistically referred to as the *high-luminosity era.*

3.2.2 Triggering Chambers

The TPC/2γ detector uses drift chambers at its inner and outer radii as part of its charged-particle triggering system. In the 1982-1986 running, these chambers had insufficient spatial measurement resolution to improve the TPC's measurement substantially. For the current high-luminosity running, the Inner Drift Chamber has been replaced with a high-resolution Vertex Chamber for precision vertex measurements.

Inner Drift Chamber

The Inner Drift Chamber (IDC) [44] extended from 11.3 cm to 15.4 cm in radius and ±60 cm in the beam direction, outside the beam pipe and inner pressure wall (and therefore within the TPC gas volume) but inside the TPC's inner field cage. Sense wires were strung axially in four cylindrical layers of 60 wires each. The IDC was used only to provide a fast signal for the charged-particle trigger; because the drift velocity and electronics were not calibrated frequently enough during the running, the spatial measurement resolution for this detector was never better than about 500 μm, too large to improve the TPC's momentum resolution. Prior to 1983 the four layers contributed independently to the trigger; two voltage breakdowns during the 1983 run necessitated the ganging together of adjacent layers, making the IDC a two-layer device.

Outer Drift Chamber

The Outer Drift Chamber (ODC) [44] is a cylindrical device built in six azimuthal segments. The segments are bolted to the outside of the solenoidal coil at a radius of 120 cm and extend ±152 cm along the length of the coil. The ODC contains three layers of 216 cells. Each cell is separated from its azimuthal neighbors by a thin plastic I-beam, and contains one centered sense wire. The wires operate in the exhaust gas of the TPC: 20% methane, 80% argon at 1 atmosphere. The ODC serves not only to deliver a fast signal to the triggering system (the IDC and ODC signals can arrive within 500 ns of beam crossover) but also to identify photons that convert in the material of the solenoid before entering the active volume of the barrel Hexagonal Calorimeter.

Vertex Chamber

For the high-luminosity runs, the IDC has been replaced with a precision Vertex Chamber (VC) [45, 46]. Its package is a tapered spool extending from 4 cm to 16 cm in radius, 39 cm long at the inner radius and 60 cm at the outer radius; the TPC's inner pressure wall has been moved outward to make room. The VC consists of 14 layers of aluminized mylar tubes, called *straws* because they are wrapped like paper soda straws. Each of the 984 straws is strung with a single centered sense wire. The VC, operating in Ar-CO_2 at 4 atm, has achieved spatial resolutions of $\sim 60\mu$m. The data used in this thesis were taken before the installation of the VC.

3.2.3 Calorimetry

The TPC/2γ detector makes use of lead/gas electromagnetic calorimetry to measure the energy carried by photons and electrons over 93% of 4π solid angle.

Hexagonal Barrel Calorimeter

The Hexagonal Calorimeter (HEX) [47, 40] covers 75% of 4π in the central region of the detector with a perpendicular thickness of 10.4 radiation lengths. The HEX is composed of six modules in the form of trapezoidal prisms that meet to form a hexagonal annulus outside the ODC. The modules are bolted to the inner surface of the iron flux-return structure. Each module contains 40 sense-wire planes alternating with lead absorber plates stacked 6 mm apart. The sense wires, spaced 5 mm apart and strung parallel to the beamline, are interwoven with nylon filaments at 10 mm spacing and are held at -1400 V. The filaments depress the electric field locally and limit the extent of avalanches on the sense wires; the result is a grid of independent Geiger cells that fire individually when traversed by charged tracks. Electromagnetic showers are initiated in the 0.14 cm-thick lead absorber plates, which are laminated to aluminum cathode strips that run at ±60° to the wires. The signal from each fired Geiger cell is seen on three channels: the strip crossing above the fired cell, the strip below, and the wire itself. The triple views help to resolve the ambiguities normally incurred in finding two-dimensional patterns from two one-dimensional views. The channels are ganged projectively in two groups in depth, corresponding to the front 27 layers and the back 13.

In 1982-1983 the HEX ran with a gas mixture of argon and ethyl bromide at 1 atmosphere. It became apparent that this was a bad choice when two of the modules were destroyed in a violent autocatalytic chemical reaction involving ethyl bromide and the aluminum in the modules [40]. For the high-field run the two ruined modules were rebuilt and the gas mixture was changed to argon–methylal–nitrous oxide. The two rebuilt modules have not performed very well; their dark currents build up over a number of hours and they have to be turned off or operated at a lower voltage. Nevertheless their energy resolution is no worse than the healthy modules; all modules have $\sigma_E/E \simeq 17\%/\sqrt{E}$ (E in GeV). A major contributor to the energy resolution is the uncertainty in unmeasured components of the total shower energy. At normal incidence, roughly 10% of the energy of a 1 GeV photon escapes from the back of the calorimeter, while 7% is lost in the solenoid package. These quantities are reconstructed on average from the measured energy deposit in the device, but are subject to unmeasured fluctuation.

Pole-Tip Calorimeter

The Pole-Tip Calorimeter (PTC) [48] is contained in two cylindrical cans mounted on the iron pole tips that return magnetic flux from the solenoid. Subtending 18%

of 4π, the 13.5 radiation-length calorimeter modules are inside the TPC gas volume and operate in proportional mode in the 8.5 atm argon-methane mix used by the TPC. The 51 sense-wire planes (interleaved with lead plates) are rotated by 60° in successive layers to provide three stereo views of electromagnetic showers. The PTC serves as a luminosity monitoring system for the experiment but has been used by relatively few physics analyses.

3.2.4 Muon System

The muon system [49] consists of four layers of close-packed triangular drift tubes in the barrel region, and three in the endcap muon "doors", layered with 16 tons of iron absorber. The drift tubes use TPC exhaust gas at 1 atm, and have a 99% efficiency for seeing a hit in at least one tube when a track crosses a layer. Tracks reaching the outer layers in the barrel must traverse between 7 and 11 interaction lengths of iron and lead. This is enough material to stop about 99% of hadronic tracks. Unfortunately in the region near the end of the barrel and the edges of the doors (30-40° in dip angle) the absorber thickness declines to as little as 5 interaction lengths, a depth inadequate to prevent substantial hadronic punchthrough.

3.2.5 Forward Detectors

The small-angle spectrometers [50] are a set of detectors covering a region between roughly 22 mrad and 180 mrad near the beam line. These detectors originally comprised an independent experiment called PEP9, or Two-Gamma; the PEP4 and PEP9 collaborations merged in the mid-1980s to form the present group. The main purpose of the forward detectors is to observe or reject low-angle electrons ("tags") associated with photon-photon collisions. The detectors are arrayed in two identical arms along the beam pipe on either side of the PEP4 apparatus. The main components of each arm of this system are

- a septum magnet of field integral $\int Bdl \simeq 2.6$ kGm
- five planar drift chambers, located in front of, behind and within the septum, for analyzing charged track momenta
- a Čerenkov detector for electron identification
- a time-of-flight scintillator hodoscope
- a high-resolution NaI calorimeter from 22-100 mrad
- a lead-scintillator shower counter covering 100-200 mrad
- an iron/drift-chamber sandwich for muon detection.

For the current high-luminosity running cycle all but the NaI system and one drift chamber plane have been removed to make room for new mini-beta quadrupoles.

3.2.6 Trigger

The PEP4 trigger system [51, 52] is responsible for deciding whether events acquired by the detector are sufficiently interesting to be written to tape. Events may satisfy the trigger by matching any of five sets of requirements:

Charged trigger. The event contains at least two charged tracks, observed in the IDC, ODC, and TPC. The ODC hits must fall in at least two distinct 30° wedges. The TPC tracks must be in at least two different sectors and point toward the origin. TPC tracks are sensed in the trigger logic as *ripples*: sequences of hits on eight-wire groups arranged in radius and z in a way corresponding to a beam-related track.

One charged plus neutral. The event contains at least one charged track in the TPC and a total energy deposition in the calorimeters greater than 1 GeV.

Neutral. The event contains a total energy deposition in the calorimeters greater than 2 GeV.

Two-particle. The event contains either back-to-back hits in the drift chambers with inner-radius TPC ionization and one full TPC ripple; back-to-back IDC hits with outer-radius TPC ionization and one full ripple; or IDC and ODC hits consistent with the charged trigger, with one full TPC ripple and a track segment in the opposite TPC endcap from the ripple. These trigger requirements are designed to be sensitive to two-track events with tracks crossing the barrel, piercing the endcaps, or crossing the midplane, respectively.

Pole-tip Bhabha. The event contains energy deposits greater than 3 GeV in each endcap. This trigger is used to monitor the luminosity and to scale down the acquisition rate for these common events.

The charged trigger is about 87% efficient for $\tau^+\tau^-$ events in general, and 92% efficient for events in the τ_{1+3} topology. The one-charged-plus-neutral trigger is more than 99% efficient for tau decays containing more than 750 MeV of neutral energy [40]. The overall trigger efficiency for events in the data sample described in Chapter 4 exceeds 99%.

3.2.7 Monitoring System

Many elements of the PEP4/9 system have performance characteristics that are sensitive to temperatures, pressures, supply voltages, dark currents, or other external factors. In some cases these factors can be tracked and their effects corrected for in the offline analysis; in other cases environmental conditions can deteriorate to the point that the experimental data is no longer useful. The purpose of the Monitoring System is to measure these critical quantities, to record them and to raise alarms when they exceed certain tolerances.

Some 2000 voltage signals representing temperatures, pressures and other quantities from around the experiment are multiplexed in three bins in the electronics house. The voltage levels are digitized and the digitized signals are polled by a PDP 11/04 computer. Values are compared to preset tolerances; when a monitored element is found to be outside its tolerances, an alarm is registered in the Control Room, where it is ignored by the physicist on duty.

About 400 of the most important monitor values are written to tape as part of the raw data for every event; a more complete set of monitor elements, in a format called CURFIL, are written to tape at the beginning of each run. In addition, run-averages of certain critical elements, including TPC sector temperatures, are written to a database at the end of each run. These quantities are later used to correct the raw data.

3.3 Computing and Data Analysis

The analysis of PEP4/9 data begins online, while the experiment is running. Not all analysis tasks can be completed online, however; various time-dependent detector calibration quantities are not yet available, and the computing power available in the experimental hall is inadequate to finish processing an event before the next arrives. The partially-analyzed data tapes are transported to the Lawrence Berkeley Laboratory, where the power of the LBL computing center can be brought to bear on the analysis.

3.3.1 Computing Resources

Early in the history of the PEP4/9 experiment, it was decided to do all computing on DEC computers, despite the availability of enormously powerful IBM mainframes at SLAC. It was felt that the available VAX cycles at LBL were adequate for the offline analysis, and that the superiority of DEC's software maintenance and development tools justified the choice. The decision was a good one; the simplifying VAX-only assumption allowed the collaboration to take full advantage of VAX Fortran's language extensions and system-dependent calls without having to use a least-common-denominator language and machine-specific code.

The computing power available in the PEP4/9 experimental hall is relatively modest. An elderly DEC PDP 11/04 controls the monitoring system (Section 3.2.7). A PDP 11/70 handles data aquisition tasks, determines the configuration of registers in the electronics house, and performs electronic calibration runs for all subsystems. High-level control of the experiment and online data analysis are handled by a VAX 11/782 (a rare, asymmetric dual-processor system, no longer supported by DEC). A VAX 11/780 provides additional support for the forward detectors. In addition, a vintage Commodore PET is responsible for controlling the HEX gas system.

Offline data processing is handled by the Computing Services VAX cluster at LBL, which comprised (at the time the high-field data were analyzed) five VAX 8650s.

3.3.2 Online Running

The PEP4/9 ONLINE program performs a number of functions.

Run control. ONLINE allows physicist-operators high-level control over data acquisition and processing.

Data quality monitoring. Operators can view events as they are recorded and look for obvious detector problems. Also, diagnostic histograms are prepared following each run.

Preliminary analysis. Every event undergoes some analysis online. Junk events are eliminated before being written to tape by a subprogram called PREANALYSIS [52]; this is essentially a software confirmation of trigger constraints. A "set-up" subprogram for each detector element reorders the raw data extracted from the electronics into a format more useful to later routines. Additionally, the first few steps of the offline analysis chain are performed as time permits.

3.3.3 Offline Data Processing

The PEP4/9 data analysis package is implemented as a series of subprogram modules linked into a backbone program called FULL. The data for each event are contained in a large array divided into sections called blocks. Each FULL subprogram reads its input from and writes its output to well-defined blocks in this array. The data can be written to a storage medium at any point in the analysis, so the analysis of a single event can be performed piecemeal with portions completed at widely different times. In particular, certain phases of the analysis depend on time-dependent detector parameters which are determined from early, incomplete analysis passes. These parameters are typically not available for some weeks after the data are acquired.

The ultimate product of the analysis chain is a file called a *data summary tape*, or DST (a misnomer, as these files more often reside on disk). The DST is a distillation of all the information gathered by the detector about an event, couched (largely) in physics language rather than detector language; that is, to the extent practical, the DST reports trajectories and momenta instead of TPC pad and wire hits, and photon four-vectors instead of calorimeter signals. The DST is enormously more compact than the partially-analyzed data files written by FULL, and therefore more accessible to individual physicists.

The transformation of raw detector signals into DSTs is accomplished by a number of FULL subprograms. The most complicated analyses are required for the TPC and the HEX.

TPC analysis sequence

The TPC analysis sequence converts digitized signals into space points, correlates the space points to identify track orbits, and projects the tracks inward and outward to other parts of the detector.

CLUSTER identifies peaks in the time-sequences of TPC pad and wire channel ADC signals, and associates neighboring pad signals into three-dimensional space points.

PATTERN fits helical tracks to the space points.

HAWIRE associates wire hits with tracks found by PATTERN for later use in the $\mathrm{d}E/\mathrm{d}x$ determination.

DISTORT adjusts space points to account for known time- and position-dependent systematic distortions in the TPC, and refits the tracks accordingly.

DEDX computes the $\mathrm{d}E/\mathrm{d}x$ truncated mean for each track and makes particle species assignments.

TRAGIC makes a final, refined helical fit for each track, adjusting for the (mass-dependent) energy loss experienced by the track as it crosses the TPC gas volume.

VERTEX attempts to improve the momentum resolution by fitting reconstructed tracks to a common event vertex.

EXTRAP extrapolates TPC tracks through the rest of the detector. This information is used later to associate hits seen in other devices with the TPC tracks.

HEX analysis sequence

The HEX analysis sequence [40, 53] adjusts digitized calorimeter data for time- and space-dependent effects, identifies hit-cluster candidates, and assigns an energy to each reconstructed cluster.

CHEX applies calibration constants to the raw HEX data. Each channel's signal is corrected based the measured pedestal and gain on its electronics, and the voltage signal converted to equivalent charge at the module. Malfunctioning (hot, dead or inefficient) channels are taken into account.

PHEX performs HEX pattern recognition. Corresponding projective channels in depth are summed; then the three views (wire channels, +60° cathode strips, -60° cathodes) are scanned for one-dimensional peaks. Each pair of one-dimensional peaks seen by the cathode channels is considered a candidate for a two-dimensional cluster, provided that a plausible candidate for a wire view of that cluster exists. The equations that describe charge balance among the views for each set of two-dimensional cluster candidates are solved by matrix inversion; the cluster candidates with consistent solutions survive.

EHEX performs energy calibration. The total charge assigned to a cluster is converted into an estimated number of fired geiger cells. Corrections are made for inefficient channels near the HEX's structural tie rods, and for shorted-out wire planes whose high voltages have been turned off. The corrected cell count is then used to assign an energy to the cluster. Estimates are made of the energy deposited in the module, leaking out the back, and lost in the coil, based on the cell count, the angular position of the cluster, and the presence of activity in the ODC (indicating a shower initiated in the coil).

Assembling the DST

The subprogram MAKEDST forms the DST based on information contained in the most highly-refined blocks in each subdetector's analysis chain. Some additional processing is done to form DST blocks that reflect input from several detectors. For example, the DST photon block comprises photon candidates from the HEX, PTC and TPC (in the latter case, reconstructed electron pairs); and the DST charged-track block includes not only TPC information but also HEX information that can be used for electron identification.

3.3.4 Production

The process of reducing a large number of raw data tapes to a small number of refined DST files is called *production.* In the early days of the PEP4 experiment, production was a slow and labor-intensive task, involving careful manual record-keeping and constant attention to ongoing batch jobs. For the analysis of the high-field data, an automated dataflow system called the *Production Manager* [54] was installed. Written by Steve Kaye of LBL in the VAX command language DCL, the Production Manager is a sophisticated and flexible system that drives the data reduction process with very little human intervention.

Before the start of a production run, a physicist must describe the Production Manager's task by linking analysis programs, specifying the number and identity of tape output streams, and identifying a temporary staging area on disk where intermediate files will reside. The Production Manager requests an operator to mount input tapes as free disk space becomes available. Input tapes are spooled to disk and analysis begins. An output tape is requested when enough output files have been generated to fill one; when the output has been written successfully to tape the files are deleted to make room for more input. The Production Manager can handle multiple independent output streams and an arbitrary number of analysis passes. Analysis jobs and tape input and output jobs are monitored for failure; in the event of disaster, the production shuts down and mail is sent to responsible humans.

3.3.5 Software Maintenance

The PEP4/9 data analysis code is a very large software system, comprising some one million lines of Fortran. This code is used and modified by nearly seventy physicists. Changes made by anybody anywhere in the system can affect the online data collection or ongoing offline analysis. The PEP4/9 collaboration has an ongoing software maintenance effort designed to prevent or ameliorate some of the disasters that could occur under these conditions.

Software organization

An attempt has been made to organize the PEP4/9 software system in a rational way. One key to this organization is the compartmentalization of software components. Code relating to each well-defined step in the analysis chain of each subdetector is maintained in a separate area. Subprograms for the data analysis, DST analysis, and Monte Carlo program backbones are kept in separate directory trees. Each subprogram's official software lives in a CMS library (see below), and the compiled code resides in an object library; related logical names make the connection between source code and object clear.

By agreement, certain common functions used throughout the software system are handled by standardized packages. For example, user input of program parameters is always performed using the packages called CLI and COM; and diagnostic error messages are generated using the VAX standard mechanism LIB$SIGNAL. Thus individual programmers are not forever reinventing new ways to do things, and features available in one subprogram (like CLI's indirect command input) are available throughout the system.

CMS

All of the source code for the PEP4/9 software system is kept in libraries maintained by DEC's Code Management System (CMS). CMS logs all changes to the files it controls, and keeps all old versions. The benefits of this system are numerous:

- The state of the entire software system at any given past time can be reconstructed.
- Bungled changes can be undone, and the system restored to the last working version.
- Changes are never anonymous; the name of the user making the change and a brief reason for the change are recorded for every transaction.
- Multiple users are prevented from simultaneously making changes to a single source file.

UPKEEP

PEP4/9 software and associated data files are used on several computers at different sites, but each file has an official version that resides in a fixed location. Object libraries, text libraries, executables, calibration files, documentation and other files of general use need to be distributed among computers at LBL and SLAC and those belonging to PEP4/9 collaborators at UCLA, UC Riverside, and UC San Diego. A table-driven automated procedure called UPKEEP, initiated nightly from LBL, updates all of these critical files from their parents over DECNET. UPKEEP begins by copying all out-of-date files in a list of non-LBL original sources from their parent nodes to the CSA cluster at LBL; then it copies those files and files whose originals reside at LBL to all other nodes. The result is that no software on any of the nodes is ever more than one day out of date.

Ongoing upgrades

Small software-maintenance-related accidents and inconveniences continue to occur within the collaboration. From time to time, a collaborator will make a change in the official source code but forget to add the compiled object to the proper object library; then the associated executable will fail to reflect the change until some time in the future, when the library is rebuilt from sources. Occasionally, too, an absent-minded user will alter a CMS-archived source file directly with a text editor, corrupting it in a way that is difficult to recover. An ongoing effort at LBL is aimed at eliminating such problems by making the software maintenance system simultaneously bulletproof and easier to use. It is hoped that the eventual system can serve as a model for other large collaborations.

CMS improvements. All CMS source libraries are now shadowed by CMS reference copy directories in a parallel directory structure. This makes it possible for users to find keywords in source files with a simple textfile search, an approach made difficult before reference copies by the presence in CMS archives of all old versions of each file. The CMS libraries and reference copies are now write-protected to prevent accidental alteration of sources, and we have prepared a 'CMS shell' application that temporarily subverts the write-protection so that users still have access to these files through the CMS mechanism.

MMS. In an attempt to ensure that object libraries and executables correspond to the current versions of their sources, the collaboration is in the process of describing the relationships among its source files to DEC's Module Management System (MMS). MMS, like its UNIX counterpart MAKE, is a system for automatically updating target files (libraries and executables) from their sources without unnecessarily compiling sources that haven't changed since the last build. We envision having the CMS shell prompt the user when an MMS build is necessary, and checking the integrity of the system with periodic MMS jobs submitted automatically.

MMS retrofit. MMS needs to know about all the dependencies among sources and objects in the entire software system, including the cases in which sources in one library refer to included files in another. The scale of the effort required to establish (and maintain) these links by hand is prohibitive. We have therefore created an application called AUTOMMS that scans source code automatically and produces complete MMS descriptions for each object library.

Chapter 4

Tau-pair Event Selection

In 1982-84 and 1985-86 the TPC/2γ experiment collected about 147 pb^{-1} of e^+e^- annihilation data at a center of mass energy of 29 GeV. The τ pair production cross section at this energy (with radiative corrections) is 136 pb, so we expect to have produced nearly 20000 τ pairs during these running periods. All but those produced at the very lowest angles with respect to the beamline pass the TPC's trigger requirements and the lowest level of event-verification software and are recorded on magnetic tape. In the high-field data set, these events are scattered among 1024 raw data tapes.

For reasons more related to simplicity of analysis than to fundamental physics, τ decays are traditionally categorized by counting the number of charged tracks in the final state. The tracks included in the count are all those associated with the primary τ decay and with relatively short-lived secondaries, but not those associated with interactions in the material of the detector or with long-lived secondaries that decay beyond the main tracking volume of the TPC. For example, the decay $\tau^- \to \nu_\tau K^{*-} \to \nu_\tau \pi^- K^0_S \to \nu_\tau \pi^- \pi^+ \pi^-$ is called a three-prong decay, because the K^0_S decays before or within the TPC gas volume, whereas the closely related decay chain $\tau^- \to \nu_\tau K^{*-} \to \nu_\tau \pi^- K^0_L \to \nu_\tau \pi^- \pi^+ \pi^- \pi^0$ is called a one-prong decay, because it is unlikely that the K^0_L decay will be observed. Similarly the decay $\tau^- \to \nu_\tau \rho^- \to \nu_\tau \pi^- \pi^0 \to \nu_\tau \pi^- \gamma e^+ e^-$, where the electron pair comes from a photon conversion in the material of the TPC, is called a one-prong decay.

The analyses that follow depend on the observation of τ decays to three charged tracks plus neutrals. Not all three-prong decays are useful to us. Events in which both τ^+ and τ^- decay to three charged tracks (which are said to belong to the *3+3 topology*) are too similar to QCD two-jet events to be easily isolated. Events in the 3+5 topology are even worse. We therefore restrict ourselves to the set of events in which one τ has decayed to three charged tracks and the other to one: the *1+3 topology*. The branching fraction to one charged track is 86%, and to three is 13.2% [5], so about 23% of all τ-pair events are in this category. In the sections that follow we will refer to events in the 1+3 topology as τ_{1+3} events, and events in which both taus decay to one charged track as τ_{1+1} events. Figure 4.1 shows

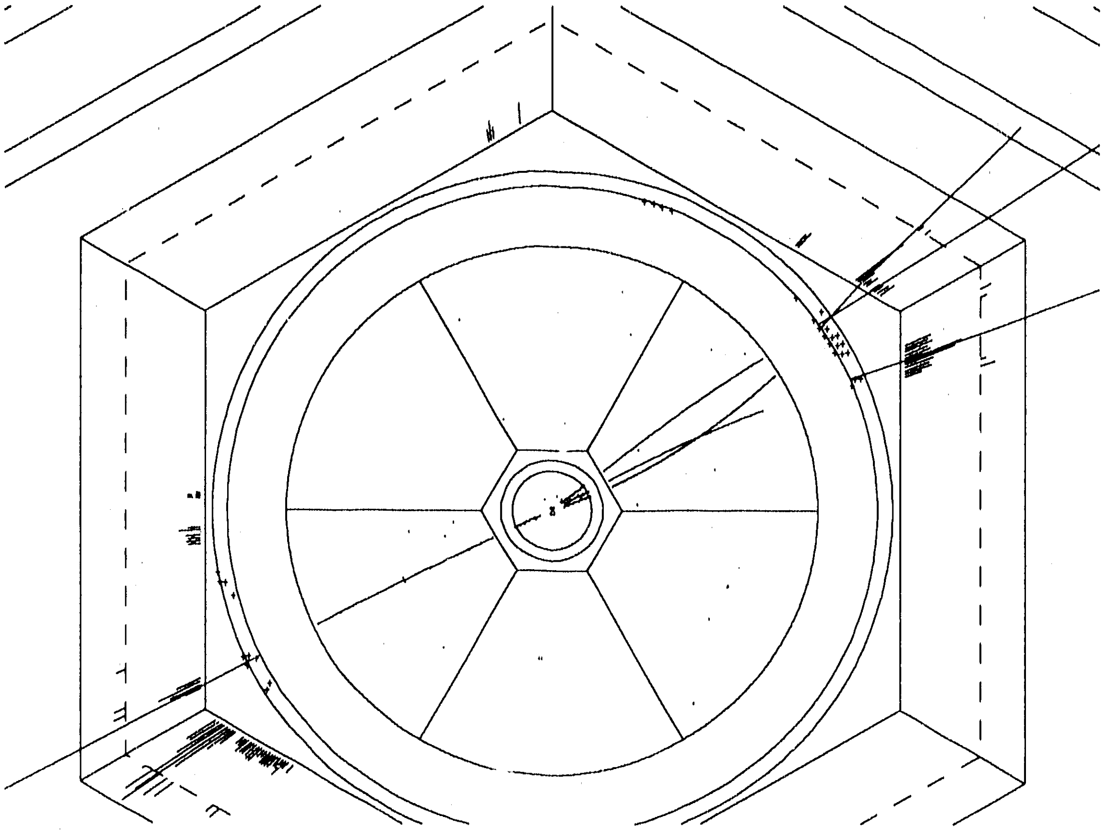

Figure 4.1: TPC event display showing a candidate τ_{1+3} event.

a candidate for a τ_{1+3} event in the TPC. The cleanliness of the event topology is striking.

The cuts described in this chapter were chosen for use with the low-field (1982-84) data set, and were applied without change to the high-field set when it became available in order to facilitate the eventual joining of the two. The efficiencies of the cuts differed somewhat between the data sets because of the different detector configurations (see Chapter 3). Some of the problems encountered in combining the data sets are discussed in Section 4.5.

The cuts are applied to the data in three passes. During the first offline data analysis pass, a selection routine called SELQQTAU is called. This routine tries to select e^+e^- events mediated by a single virtual photon; this class includes many physics processes not related to the τ. The first set of τ-specific cuts (called loose cuts) are designed to select events consistent with the 1+3-prong topology while maintaining a high efficiency for detecting those events. The purity of the sample thus obtained is very low. The second set (called tight cuts) are intended to select true 1+3-prong τ-pair events with reasonable efficiency while eliminating almost all of the background. These cuts yielded an event sample of sufficient purity for the analysis of Chapter 5. For the purposes of the analyses of Chapter 6, however, additional cuts are required. These analysis cuts are described in Section 6.3.

The cuts applied during each pass over the data are described in the next three sections. Each pass reapplies and tightens the cuts of the previous passes while adding new restrictions. The final data sample is defined by the tight cuts of Section 4.3; the intermediate cuts of Sections 4.1 and 4.2 are described only to document the data reduction process.

4.1 Annihilation Event Selection

All events passing PREANALYSIS are written to raw data tapes. The event-selection cuts in PREANALYSIS are deliberately loose; one does not want to throw away potentially interesting exotic events without writing them to tape at all. The cost of making this conservative choice is the size of the output. The PEP4/9 experiment generated over 4000 6250 bpi raw data tapes between 1982 and 1986. Clearly it is prohibitive to mount and read all those tapes for each analysis project.

Many PEP4 physics projects are concerned with e^+e^- annihilation events mediated by a single virtual photon: $e^+e^- \rightarrow \gamma^* \rightarrow q\bar{q}$, e^+e^-, $\mu^+\mu^-$, or $\tau^+\tau^-$. These events are accompanied on the raw data tapes by events from other sources: the various two-photon reactions, $e^+e^- \rightarrow \gamma^*\gamma^* \rightarrow X\bar{X}$; cosmic rays; and beam-gas or beam-pipe interactions. An event selection subprogram, SELQQTAU, attempts to separate the single-photon population from the remaining events. In addition, it applies modest cuts against Bhabha and $\mu^+\mu^-$ events that are no longer interesting for physics analysis. The cuts rely only on the gross features of reconstructed TPC tracks; generally at the time SELQQTAU is run, the TPC analysis sequence has only progressed as far as HAWIRE, and no other subdetector data has been analyzed, so no particle identification information is available.

Events passing SELQQTAU satisfy these criteria:

1. The number of good tracks $\geq$ **2**. Here a good track is defined by
   (a) Track momentum > **150 MeV**.
   (b) The track extrapolates to the interior of an imaginary cylinder **5 cm** in radius and **10 cm** long, coaxial with the beam and centered at the nominal collision point. This removes tracks associated with secondary interactions in the material of the detector and tracks from beam-gas interactions and other non-annihilation sources.
   (c) Track dip angle (i.e. the complement of the polar angle, measured from the e^- beam direction) $\leq$ **60°**. Tracks closer to the beamline tend to be poorly measured; they lack the lever arm for a proper momentum measurement, and they have fewer wires sampling their ionization rates.

   (d) For tracks of momentum < 3.3 GeV/c, the momentum error is smaller than the momentum.

2. Events with two good tracks are kept if
   (a) The tracks have acollinearity $> \mathbf{2^\circ}$ in dip and $> \mathbf{5^\circ}$ in azimuth.
   (b) At least one track has transverse momentum $\geq$ **1.5 GeV/c.**

3. Events with three good tracks are kept if
   (a) No two tracks have acollinearity $> \mathbf{2^\circ}$ in dip and $> \mathbf{5^\circ}$ in azimuth.
   (b) The sum of track transverse momenta $\geq$ **1.5 GeV/c.**

4. Events with $\geq$ four good tracks are kept if
   (a) The sum of track transverse momenta $\geq$ **1.5 GeV/c.**

SELQQTAU reduced the data from the high-field run to 193 tapes.

4.2 Loose Cuts

The loose selection cuts are intended to reduce the total data set to a manageable level. Events in the loosely-selected sample satisfy these criteria:

1. The total number of reconstructed charged tracks in the event is between **4** and **11** inclusive. This cut removes the most obvious background events with low multiplicity (Bhabha scatters, muon pairs, $\gamma\gamma \rightarrow 2$ prongs, τ_{1+1}) and high multiplicity ($q\bar{q} \rightarrow$ jets).

2. The number of good tracks $\geq$ **4.** Here a good track is defined by
   (a) Track momentum $>$ **150 MeV.**
   (b) The track misses the nominal collision point by $\leq$ **5 cm** in radius and $\leq$ **10 cm** in the beam direction.
   (c) Track dip angle $\leq \mathbf{60^\circ}$. Tracks closer to the beamline tend to be poorly measured; they lack the lever arm for a proper momentum measurement, and they have fewer wires sampling their ionization rates.

3. The event contains one good track (the one–prong candidate) separated by at least $\mathbf{120^\circ}$ from at least three good tracks (the three–prong candidates). Cuts (2) and (3) define the 1+3 topology.

4. The scalar sum of the momenta of all reconstructed charged tracks is greater than **4.0 GeV/c.** This requirement removes low-energy background events from two-photon collisions and beam-gas interactions.

These loose τ_{1+3} cuts reduced the high-field sample to 41 tapes containing 14842 events, or about 2% of all events passing PREANALYSIS.

Despite the leniency of these cuts, a substantial portion of the true τ_{1+3} sample is lost at this stage; the acceptance is only about 55%. Most of these events are lost in the geometrical cuts because the $\tau^+\tau^-$ axis is too close to the beam line, so some tracks are not found or have such a short projection on the TPC endcap that their momenta and ionization energy loss rates are poorly measured. About 1.7% of the events in the remaining sample are τ_{1+3} events. This purity is estimated by comparing the size of the sample to the product of the number of τ_{1+3} events expected in our run and the Monte Carlo acceptance for τ_{1+3} events.

4.3 Tight Cuts

The surviving events are subjected to rigorous cuts designed to remove most of the remaining background. The tightly-selected sample is small enough to reside easily on disk. Events in the tightly-selected τ_{1+3} sample satisfy these criteria:

1. The total number of reconstructed charged tracks in the event $<$ **10.** Note that up to six stray tracks can remain in the event, in addition to the four 1+3 candidates. These extra tracks are typically conversion electrons.
2. The number of good tracks = **4.** In this case a good track satisfies
   (a) Track momentum $>$ **300 MeV.**
   (b) The track misses the nominal collision point by $\leq$ **5 cm** in radius and $\leq$ **10 cm** in the beam direction.
   (c) Track dip angle $\leq$ **60°.**
   (d) The momentum measurement error is smaller than the momentum itself.
3. The scalar sum of the momenta of all reconstructed charged tracks is greater than **4.5 GeV/c** and less than **24.0 GeV/c.** Some missing energy is required as a cut against QCD events, muon pairs, and showering Bhabhas.
4. The event contains exactly one good track at least **140°** from the other three good tracks. This is a tighter topological constraint.
5. The angle between the one-prong candidate and each of the other good tracks is less than **178°.** This acollinearity requirement avoids radiative muon pairs and Bhabhas accompanied by conversion electrons.
6. The sum of the charges of the four good tracks is **zero.** This is a reality check against higher-multiplicity events with missing tracks.

7. The invariant mass of the four good tracks $\geq$ **3 GeV/c^2** (assuming pion masses). This is a cut against $\gamma\gamma$ events.
8. The invariant mass of the three-prong candidates $\leq$ **2.0 GeV/c^2**, assuming pion masses. This discriminates against QCD events.
9. None of the three-prong candidates is well-identified as an electron by dE/dx. (By "well-identified" here we mean $\chi^2_e < 9.0$ and $\chi^2_{\text{hadron}} > 9.0$.) This avoids showering Bhabhas and other two-prong events with associated conversion pairs. This is a mild requirement; a more rigorous one would be to require that one (or all) of the three-prong candidates be well-identified as a hadron. (The one-prong candidate can be an electron.)

The tight selection cuts yielded 585 τ_{1+3} candidates in the low-field data set and 783 in the high-field.

4.4 Efficiencies

Table 4.1 summarizes the efficiencies of the tight selection cuts for retaining true τ_{1+3} events in various modes. The efficiencies depend the one-prong and three-prong decay modes involved, and also on the experimental period. Section 4.5 discusses the reasons for the discrepancies among data sets. Selection efficiencies range from 22% to 31% in the low-field data and from 30% to 40% in the high-field.

Three-Prong Mode	**One-Prong Mode**			
	e	$\mu/\pi/K$	ρ	$\pi\pi^0\pi^0$
Low-field data set				
$\pi\pi\pi$	28.4%	31.1%	26.9%	24.0%
$\pi\pi\pi\pi^0$	26.7%	29.5%	24.9%	22.7%
$K\pi\pi$	30.0%	31.3%	28.0%	26.7%
$KK\pi$	27.8%	31.8%	27.5%	24.5%
KKK	26.2%	27.1%	24.3%	22.6%
High-field data set				
$\pi\pi\pi$	36.7%	40.1%	36.3%	34.9%
$\pi\pi\pi\pi^0$	33.1%	37.8%	32.6%	31.3%
$K\pi\pi$	38.1%	39.1%	36.7%	33.6%
$KK\pi$	37.9%	39.2%	36.0%	34.0%
KKK	32.5%	35.8%	31.3%	30.0%

Table 4.1: Selection efficiencies for the tight cuts.

The most important inefficiencies come from the basic topological cuts; in low-field Monte Carlo simulations, 48% of true τ_{1+3} events fail tight cut 1, the requirement that four good tracks be identified. The angular distribution of τ pair production, $1+\cos^2\theta$, favors production near the beamline, where the track dip angle requirement 2c makes the selection inefficient. This cut is nevertheless essential for providing a sample of well-measured tracks.

4.5 Comparing and Combining the Data Sets

The number of τ_{1+3} candidate events remaining after the application of the tight selection cuts is smaller in the low-field data set than in the high-field data, despite the fact that the low-field data represents somewhat more integrated luminosity. Table 4.1 reveals that the overall selection efficiencies for all modes, computed using Monte Carlo simulations, are lower in the low-field data set than in the high-field. If we are to present results based on the sum of the data sets, we must understand this discrepancy and account for it in our calculations.

Figure 4.2 shows the number of events remaining after the application of each tight selection cut to events in Monte Carlo samples. (For simplicity we show results for one three-prong decay channel only; others are similar.) The most dramatic drop results from the requirement that the event contain at least four good tracks. This cut also shows a marked difference between the two data sets. In the low-field experimental configuration, the amount of material between the interaction point and the TPC gas volume was substantially higher than in the high-field configuration (see Chapter 3). The resulting increase in multiple scattering makes low-field tracks more likely to fail the good-track criteria 2b and 2d. For reference, Figure 4.3 shows the distributions of fractional track curvature error ($\delta C/C \propto \delta p/p$) for the two data sets. The effect of criterion 2d on the high-field data is negligible. Overall, the efficiency for labelling tracks as good is 74% in the low-field data set and 81% in the high-field.

Another difference between the low- and high-field data sets is in the analysis software. When the low-field data were first analyzed the estimate used for the $\mathrm{d}E/\mathrm{d}x$ resolution (a quantity that depends on the track parameters but is not measured directly) was correct on average but left some uncorrected systematic effects. In the course of analyzing the newer high-field data set, new estimates were prepared that corrected for effects of track dip angle and removed a spurious nonlinear correction based on the ionization value itself [55]. These new corrections yield resolution estimates that differ by as much as 20% from the earlier version for some tracks. Because there is no reason to believe that the TPC's $\mathrm{d}E/\mathrm{d}x$ resolution changed between the experimental periods, and because the new resolution estimates are in closer agreement to the observed distribution of measured track ionization values, the new (high-field) resolution formulas have been applied to the low-field data in the current analysis.

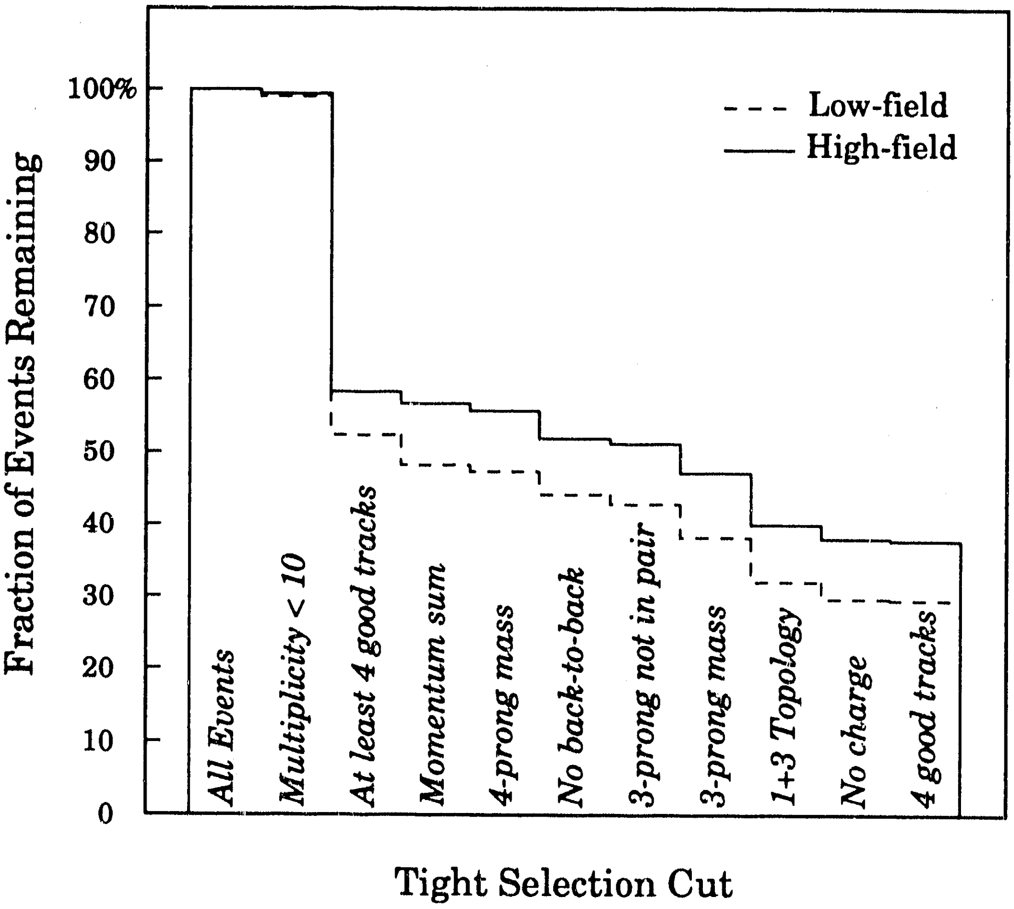

Figure 4.2: Events remaining after the application of successive cuts in the low-field (dashed) and high-field (solid) data sets. Based on Monte Carlo simulations of the decay chain $\tau \to \nu_\tau \rho(1700) \to \nu_\tau \pi\pi\pi\pi^0$.

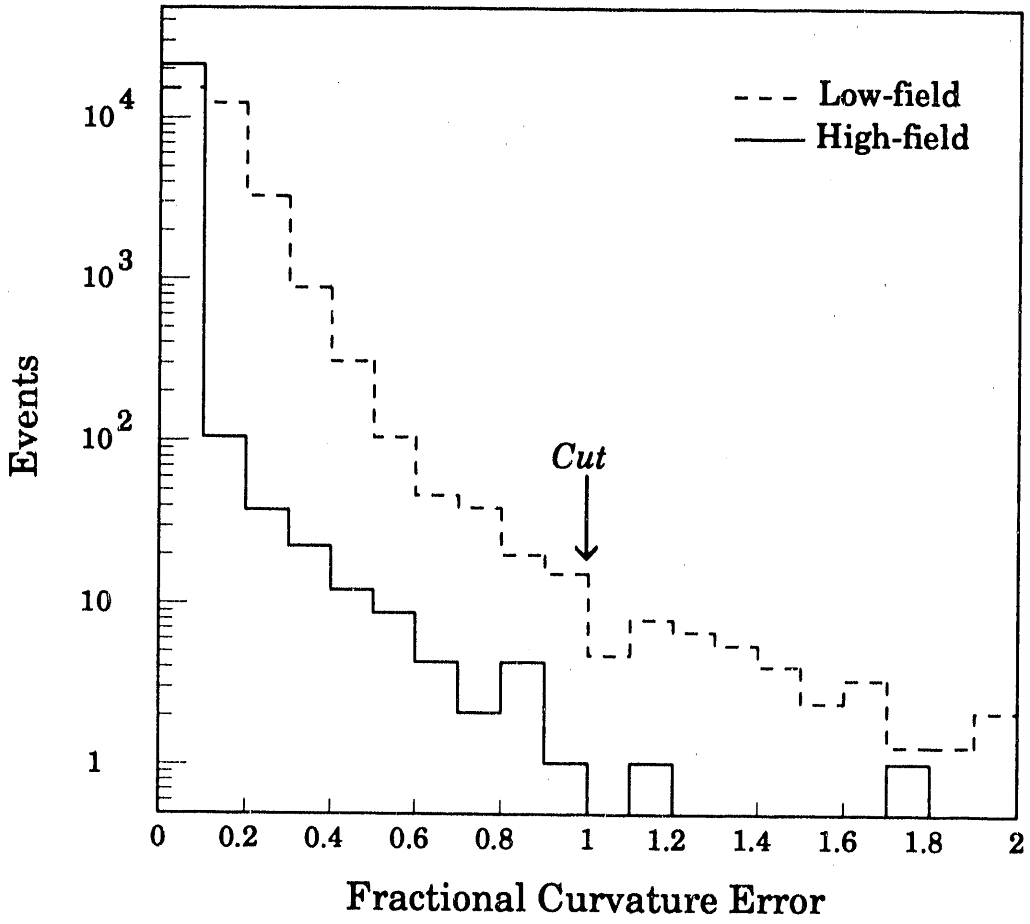

Figure 4.3: Fractional curvature error in low-field (dashed) and high-field (solid) Monte Carlo simulations. Note the five-decade vertical log scale; beyond the first bin, the spectra differ dramatically.

4.6 Backgrounds

The principal background processes to the τ_{1+3} sample are

QCD: $e^+e^- \rightarrow q\bar{q} \rightarrow$ jets. The average charged multiplicity of these events at PEP is 10, but events in which much of the energy is carried away by neutral hadrons (π^0, n, K_L) or which contain many unobserved tracks close to the beam line can fake the 1+3 topology.

τ_{1+1}: $e^+e^- \rightarrow \tau^+\tau^-(\gamma)$. These are τ-pair events in which a decay normally classified as 1-prong has faked a 3-prong. Examples include $\tau \rightarrow \nu_\tau \rho$ with a converted photon from the π^0; or $\tau \rightarrow \nu_\tau \bar{\nu}_e e$ accompanied by a converted bremsstrahlung photon.

$\gamma\gamma$: $e^+e^- \rightarrow e^+e^- X$, where X represents some low-multiplicity state. The cross section is large, but these events are produced with low visible energy, and the 1+3 topology is not typical.

Bhabha scatters: $e^+e^- \rightarrow e^+e^-(\gamma)$. A converted photon from bremsstrahlung or initial- or final-state radiation can provide two extra prongs on one side of the event. The tight selection cuts are very good at discriminating against these events, but the cross section is enormous (technically infinite when integrated down to zero polar angle).

Radiative muon pairs: $e^+e^- \rightarrow \mu^+\mu^-\gamma$. Again a converted photon provides the third and fourth prongs.

The tight selection cuts are very efficient at rejecting these backgrounds. The backgrounds remaining in the selected sample are estimated using Monte Carlo simulations that include the details of the event generation and the electromagnetic and hadronic interactions of particles in the material of the detector. The estimates are summarized in Table 4.2. On the basis of these Monte Carlo background estimates, the sample is estimated to be 95% pure. The most significant surviving backgrounds are QCD and τ_{1+1} events.

Source	**Low-field**	**High-field**
$q\bar{q}$	14.7	19.8
$\tau^+\tau^-(1+1)$	12.6	16.9
$\gamma\gamma$	1.9	2.5
Bhabha	1.1	1.4
$\mu^+\mu^-\gamma$	$<< 1$	$<< 1$
Total	30.3	40.6

Table 4.2: Estimates of the numbers of background events in the tightly-selected sample.

Chapter 5

Limit on the Decay $\tau^- \rightarrow \nu_\tau K^- K^0$

THE QUESTION OF THE MAGNITUDE of second-class currents [17] in weak interactions is an open one. Several authors [32, 31, 33] have pointed out the value of the decays $\tau^- \rightarrow \nu_\tau \pi^- \eta$ and $\tau^- \rightarrow \nu_\tau \pi^- \omega$ as tests for the presence of second-class axial vector and vector weak currents; to date neither of these modes has been observed. While the ARGUS collaboration has established an upper limit on the second-class axial vector current in tau decays by studying the decay $\tau^- \rightarrow \nu_\tau \pi^- \omega$ [25], the HRS collaboration presented evidence in 1986 for a second-class vector current interaction by measuring a branching ratio of $(5.1 \pm 1.0 \pm 1.2)\%$ for the decay $\tau^- \rightarrow \nu_\tau \pi^- \eta$ [36]. The final state $K\bar{K}$ is related by an SU(3) rotation to $\pi\eta$, so if $\pi\eta$ was indeed present in τ decays we would expect to see $K\bar{K}$ also [35, 56]. With good charged particle identification this final state is easily reconstructed and relatively background-free. The HRS result, since ruled out by other experimental groups as well as by subsequent studies by the HRS collaboration itself, was the immediate motivation for the present study. In this chapter we present an upper limit on the branching fraction $BR(\tau^- \rightarrow \nu_\tau K^- K^0)$. Our result limits the size of the second-class vector current.

The results of this analysis have been published in Phys. Rev. Lett. **59**, 751 (1987).

5.1 Method

In this analysis we are looking for decays of the type $\tau^- \rightarrow \nu_\tau K^- K_S^0$, proceeding via $K_S^0 \rightarrow \pi^+ \pi^-$ to three charged tracks. The search begins with the sample of 1372 low-field and high-field τ_{1+3} candidates selected by the cuts described in Chapter 4. On the three-prong side of each event in this sample, we make loose cuts on vertex position and invariant mass to identify track-pairs consistent with the decay $K_S^0 \rightarrow \pi^+ \pi^-$. We then look for evidence of a charged kaon population among the sample of third tracks from each event containing a K_S^0 candidate. The nonobservation of kaons leads to an upper limit on the $\tau^- \rightarrow \nu_\tau K^- K^0$ decay rate. As a check on the various acceptances involved in the limit calculation, we present a parallel measurement of the (nonzero) branching fraction $BR(\tau^- \rightarrow \nu_\tau K^{*-})$.

5.1.1 K_S^0 selection

The opposite-sign track pairs on the three-prong sides of our τ_{1+3} event sample are examined for consistency with the decay $K_S^0 \rightarrow \pi^+\pi^-$. Individual tracks are required to satisfy the following criteria (in addition to the good-track criteria of Chapter 4):

1. The track's dE/dx is consistent with the pion hypothesis: $\boldsymbol{\chi^2_\pi < 7.0}$.
2. The distance of closest approach to the nominal event vertex is greater than $\mathbf{(0.04 + 0.02/p^2)^{1/2}}$ **cm**. (This corresponds to a miss of 1.7 cm at 3 GeV/c^2.)

Track pairs are labeled as K_S^0 candidates if

1. The tracks have opposite sign.
2. The tracks approach each other within **0.5 cm**. The point of closest approach is called a secondary vertex.
3. The vector momentum sum of the pair differs from the vector connecting the nominal event vertex to the secondary vertex by less than **5°**.
4. At least one of the tracks has dE/dx inconsistent with that of an electron.
5. The flight path from the event vertex to the reconstructed pair vertex is at least **1.5 cm**.
6. The invariant mass of the pair (assuming pion masses) matches the K_S^0 mass to within **±80 MeV/c^2**.

The K_S^0 mass resolution of the detector is typically 35 and 16 MeV/c^2 in the low- and high-field data sets respectively, making the 80 MeV/c^2 window very loose. Figure 5.1 shows the invariant mass of the $\pi^+\pi^-$ track pairs passing all but the mass cut 6; a clear population of K_S^0 is seen on a falling background. The 37 events containing K_S^0 candidates that pass the mass cut are represented by the shaded area. The efficiency for finding K_S^0 events with these cuts is 46% in the low-field data and 57% in the high-field. These efficiencies include the effects of the vertex-association cut in the τ_{1+3} event selection (criterion 2b in Section 4.3).

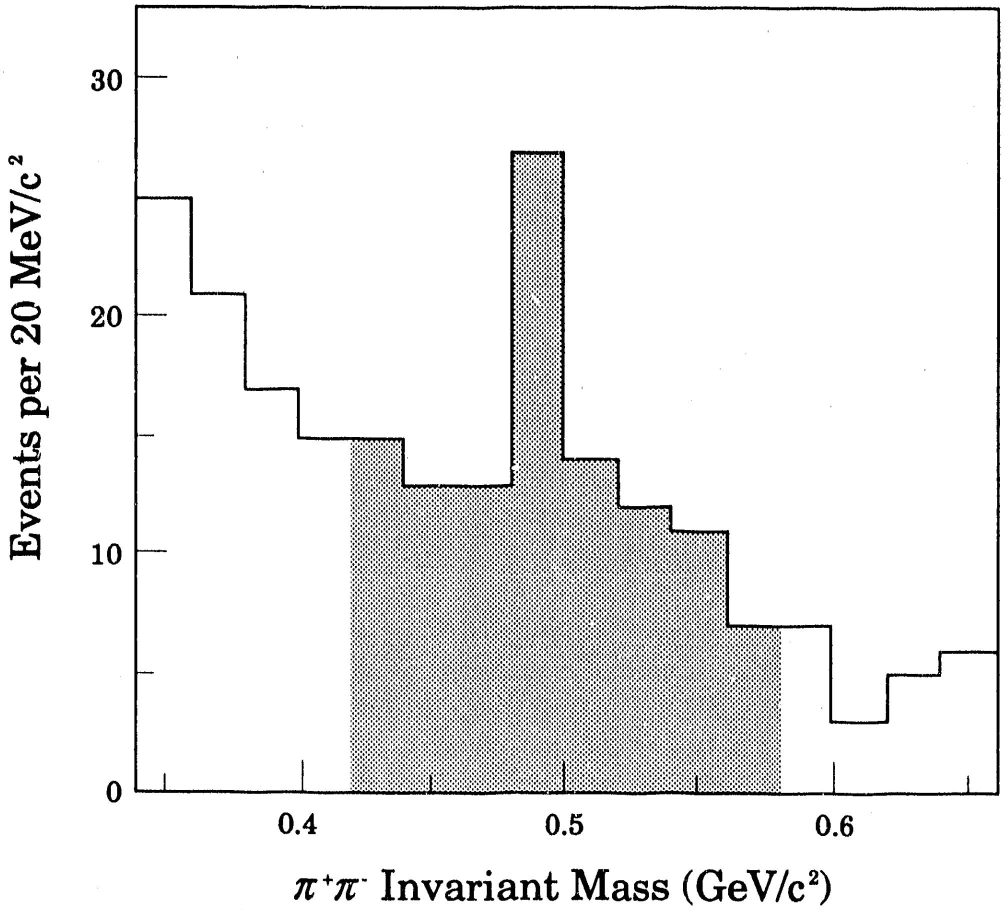

Figure 5.1: Invariant mass of $\pi^+\pi^-$ pairs passing the loose secondary-vertex cuts used in establishing the $\tau^- \to \nu_\tau K^- K_S^0$ branching fraction limit.

5.1.2 $K^{\pm}$ candidates

The sample of third-prong tracks in events containing K_S^0 candidates is now examined for kaon content. The species determination requires a reliable $\mathrm{d}E/\mathrm{d}x$ measurement, so events in which the candidate track has fewer than 60 wires contributing to its $\mathrm{d}E/\mathrm{d}x$ measurement are rejected. Figure 5.2 shows the measured values of $\mathrm{d}E/\mathrm{d}x$ and $\ln(p)$ for the remaining well-measured tracks. There is no evidence for a kaon population among these tracks.

An upper limit on the number of kaons in this sample is obtained by eliminating tracks in the ambiguous region and performing a species-hypothesis fit on the remainder. Figure 5.2 shows a π/K crossover region in the neighborhood of 1 GeV/c; we avoid this region by cutting away tracks with $0.9\ \mathrm{GeV}/c < p < 1.4\ \mathrm{GeV}/c$. The 37 surviving track measurements are the input to an extended maximum likelihood fit [57, 58] whose variable parameters are the number of pions and the number of kaons in the sample. The fit takes into account the momentum and $\mathrm{d}E/\mathrm{d}x$ resolutions and their variations with momentum and angle; a similar fitting procedure will be discussed in more detail in the next chapter.

The best fit to the number of kaons in the sample is zero. Simple Poisson statistics give an upper limit of 3.0 events at 95% CL from zero observed; we prefer to quote the more conservative limit of 4.4 charged kaons at 95% CL, based on the likelihood contour found by the fit.

5.1.3 Branching fraction limit

The corresponding branching fraction limit is computed by comparing the upper-limit number of decays to the number of events in the τ_{1+3} sample, taking into account the effects of our K_S^0 reconstruction efficiency and charged kaon identification cuts. These effects were evaluated with a Monte Carlo simulation of τ production and decay, including initial- and final-state radiation [59], and the effects of interactions of subsequently created particles in the material of the detector, including momentum and $\mathrm{d}E/\mathrm{d}x$ errors, tracking inefficiencies, and nuclear and electromagnetic showering. The Monte Carlo is also used to correct for slight differences in event selection efficiencies among the various hadronic final states. The mechanics of extracting a branching fraction when the acceptance varies from mode to mode on both the one- and three-prong sides and from experiment to experiment are described in Section 6.9.

The τ_{1+3} data sample consists of 1372 events, of which 71 are estimated to be background (see Table 4.2). The upper limit of 4.4 events in this sample corresponds to the branching fraction limit

$$BR(\tau^- \rightarrow \nu_\tau K^- K_S^0) < 0.13\%\ (95\%\ \mathrm{CL}), \tag{5.1}$$

or

$$BR(\tau^- \rightarrow \nu_\tau K^- K^0) < 0.26\%\ (95\%\ \mathrm{CL}). \tag{5.2}$$

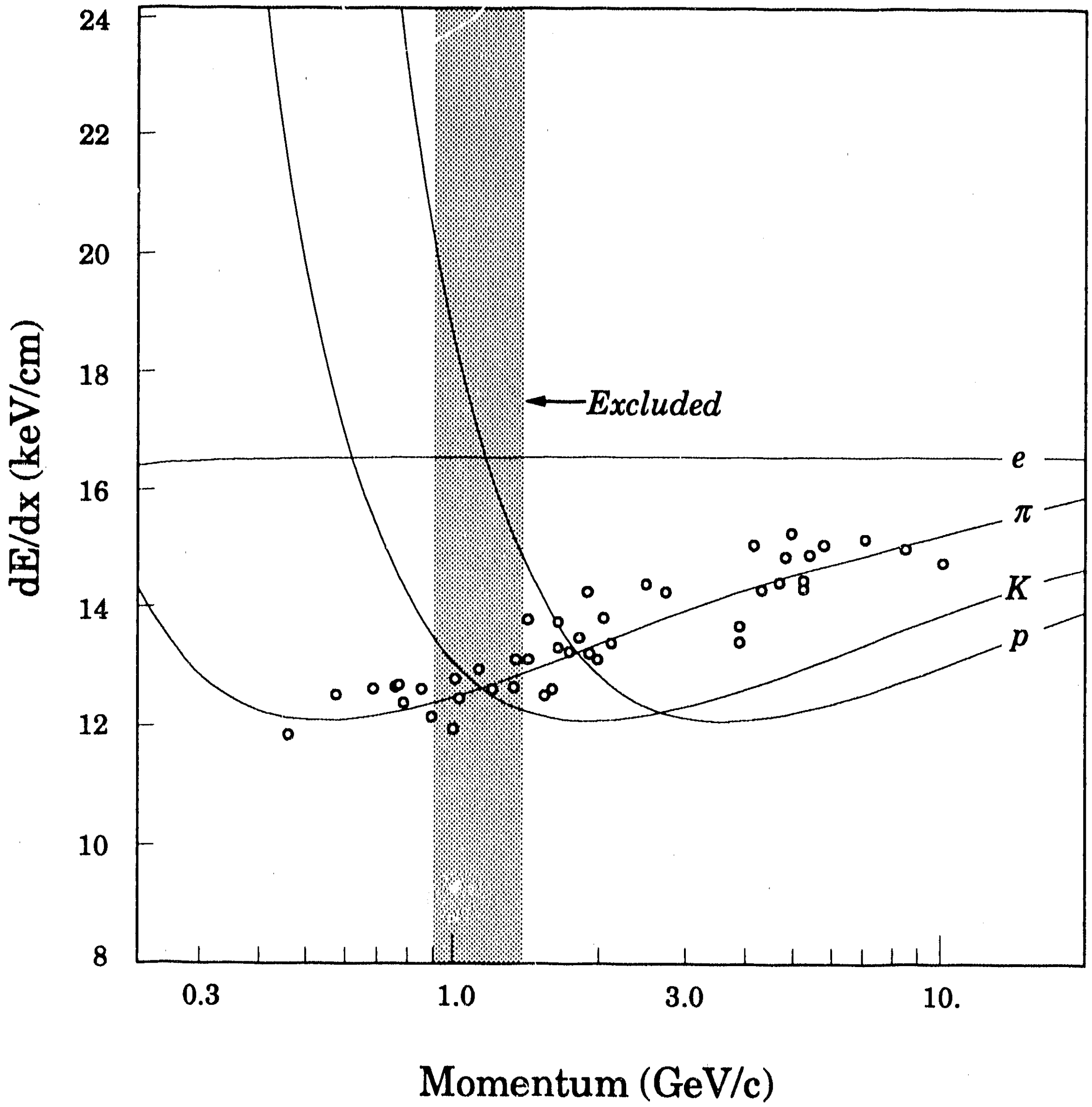

Figure 5.2: Scatter plot of $\mathrm{d}E/\mathrm{d}x$ vs. $\ln(p)$ for well-measured tracks accompanying K_S^0 candidates on the three-prong side of events in the τ_{1+3} sample. The solid lines represent the expected values for various particle species.

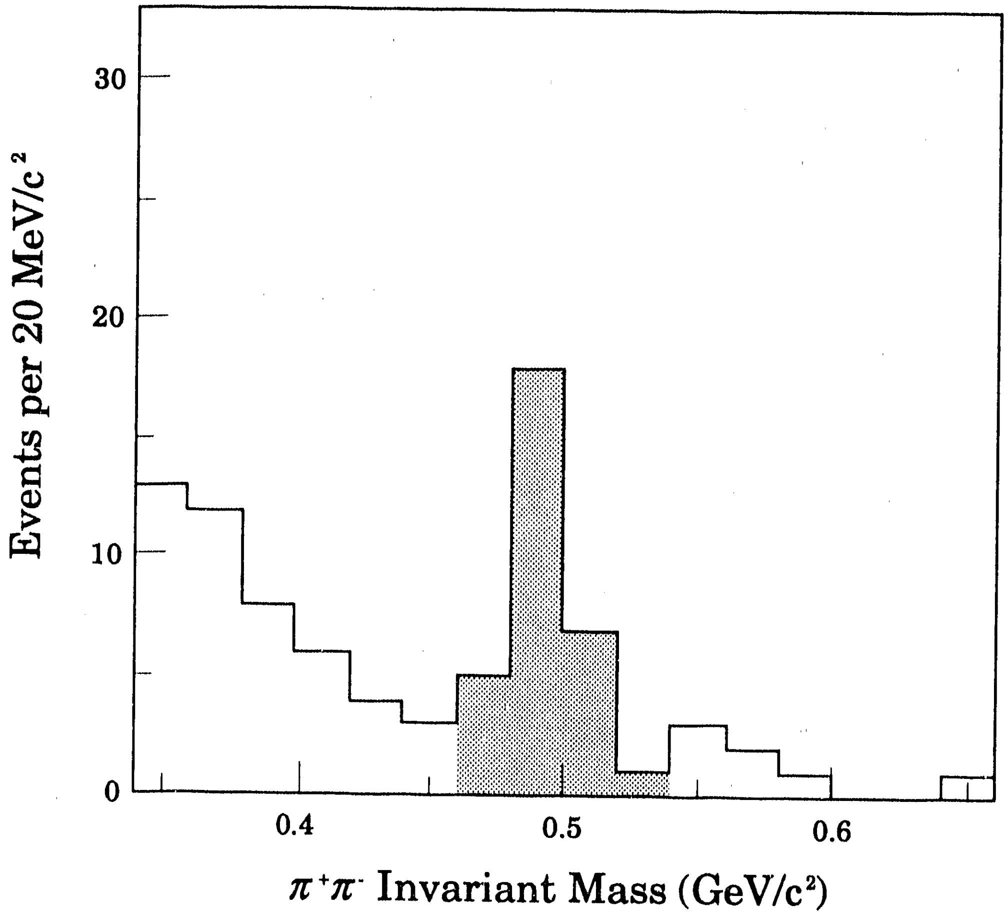

Figure 5.3: Invariant mass of $\pi^+\pi^-$ pairs passing the tight secondary-vertex cuts used in the K^* branching-fraction measurement.

5.2 K^* Branching Fraction Measurement

This null result is more credible if we can demonstrate that the PEP4/9 detector can observe K^0_S-containing tau decays and that our Monte Carlo simulations correctly reproduce the various analysis and detection efficiencies. We check our efficiency estimates by measuring the branching fraction of the decay $\tau^- \rightarrow \nu_\tau K^{*-}$ and comparing to the world average of $(1.39\ ^{+0.18}_{-0.20})\%$ [5, 60, 61]. We measure this branching fraction by observing the decay chain $K^{*\pm} \rightarrow \pi^\pm K^0_S$, $K^0_S \rightarrow \pi^+\pi^-$, which tests our ability to identify K^0_S in τ_{1+3} events.

K^0_S candidates are selected using the procedure described in Section 5.1.1, with tighter decay distance (> 3 cm) and momentum vector alignment ($< 2°$) cuts applied to reduce the number of accidental combinations. The resulting invariant mass combinations are plotted in Figure 5.3. Opposite-sign pion pairs with invariant masses within ± 40 MeV/c^2 of the K^0_S mass (the shaded region) are selected

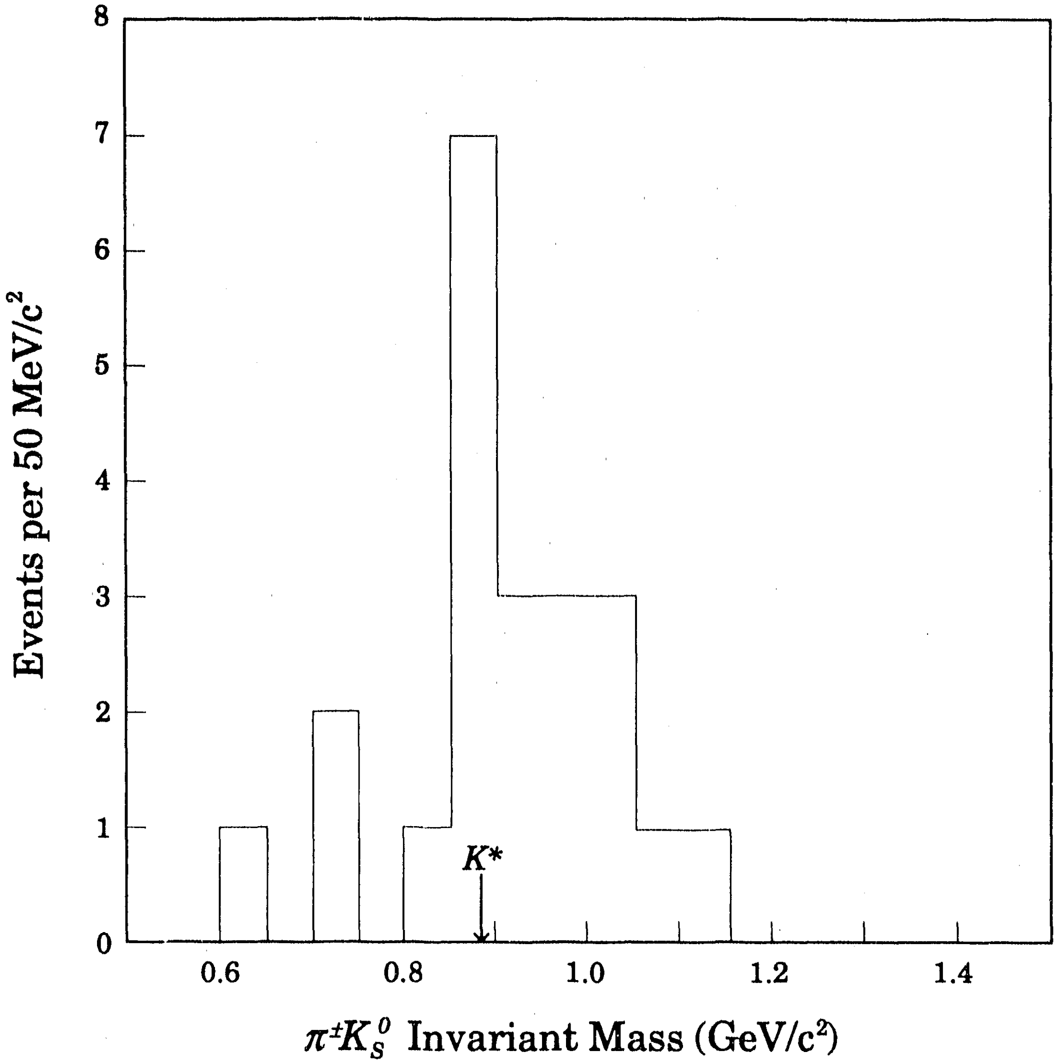

Figure 5.4: Invariant mass of πK_S^0 combinations. The K^* is visible on a low background.

as K_S^0 candidates.

Each K_S^0 candidate is combined with the remaining charged track in the same hemisphere and the invariant mass computed. A clear K^* peak with a width consistent with the expected width is visible in the resulting invariant mass distribution, shown in Figure 5.4. The 18 combinations with invariant mass between 0.8 and 1.1 GeV/c^2 are labeled as K^* candidates, of which 3 ± 3 are estimated to be background. This leads to a measured branching fraction $BR(\tau^- \to \nu_\tau K^{*-})$ of $(1.5 \pm 0.4 \pm 0.4)\%$, where the errors are statistical and systematic, respectively. The systematic error is dominated by uncertainty in the background estimation. This measurement agrees with the world average.

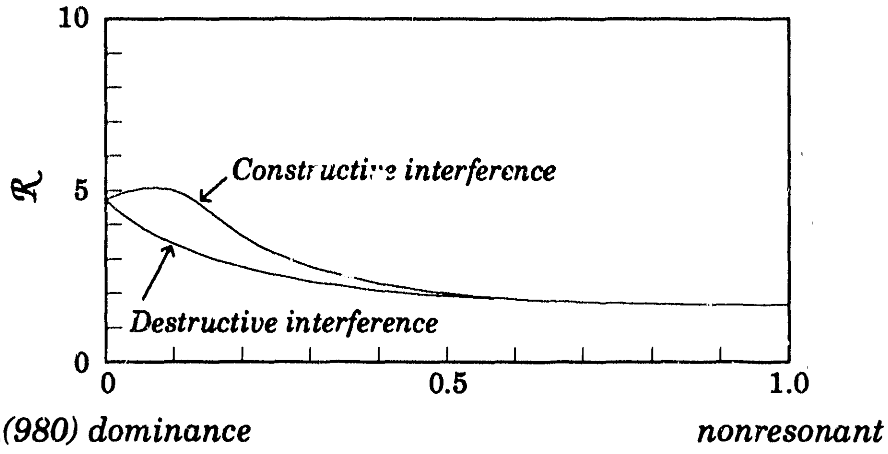

Figure 5.5: The variation of the rate-ratio $\mathcal{R} \equiv \Gamma(\tau \to \nu\pi\eta)/\Gamma(\tau \to \nu K\bar{K})$ as a function of the ratio of nonresonant and resonant production amplitudes [56]. In no case does $\mathcal{R}$ exceed 5.1.

5.3 Implications for Second-Class Currents

The τ-decay s-wave final states $a_0^-(980)$, $\pi^-\eta$, and K^-K^0 are fed by the scalar quark density term $(\bar{u}d)_s$, labelled by the second-class coefficient f_3 in the matrix element of Equation 2.13. We recall from Chapter 2 that in the Standard Model these scalar states are expected to be present in τ decay only at an exceedingly low level; any substantial branching fraction to any of these states (such as the measurement $BR(\tau^- \to \nu_\tau \pi^- \eta) = 5.1\%$ reported by the HRS collaboration in 1986 [36]) would signal physics beyond the Standard Model.

We first consider the consistency of our result (Equation 5.2) with that of HRS. M. Suzuki has examined the relative production of $\pi\eta$ and $K\bar{K}$ in τ decay [56]. The final states can be reached nonresonantly or resonantly via the a_0, and the real parts of the resonant and nonresonant amplitudes can interfere constructively or destructively. The behavior of the ratio $\mathcal{R} \equiv \Gamma(\tau \to \nu\pi\eta)/\Gamma(\tau \to \nu K\bar{K})$ as the importance of resonant production varies is shown in Figure 5.5. Using quite general SU(3) arguments it is shown that for all mixtures of amplitudes,

$$\mathcal{R} < 5.1. \tag{5.3}$$

This estimate is obtained under the assumption that SU(3) symmetry is broken only by final-state phase space, and with the η treated as a pure octet state. Equation 5.3 is consistent with observed a_0 branching fractions [62]. Additional considerations, including p-wave production and $\eta - \eta'$ mixing, serve only to decrease the maximum value of $\mathcal{R}$. If the η is considered to be a mixed state and the nonet assumption [63] is used to relate the octet and singlet amplitudes, cancellations between those amplitudes tend to reduce the $\nu\pi\eta$ branching fraction and hence $\mathcal{R}$ [56]. Nonresonant production lessens the phase space suppression of $K\bar{K}$

imposed by the a_0, and results in predictions for the value of $\mathcal{R}$ near 2. Allowed production of $K\bar{K}$ in a p-wave via a first-class vector current would also reduce $\mathcal{R}$; SU(3) forbids $\pi\eta$ in states of odd relative angular momentum.

Therefore, although neither the branching fractions of the a_0 nor the relative importance of resonant and nonresonant production are well known from experimental evidence, general theoretical arguments allow us to consider the relationship between our limit (5.2) on the branching fraction for $\tau^- \to \nu_\tau K^- K^0$ and the HRS measurement of $\tau^- \to \nu_\tau \pi^- \eta$. Consistency between Equation 5.2 and the HRS central value would require a ratio

$$\mathcal{R} > 19. \tag{5.4}$$

Reducing the HRS value by 2σ gives

$$\mathcal{R} > 12. \tag{5.5}$$

Neither value is achievable under the simple theoretical assumptions that led to the conservative limit of Equation 5.3.

Armed with a theoretical relationship between the major candidates for scalar hadronic final states, we can transform the limit (5.2) into a general limit on the scalar component of the weak interaction in τ decay. Again following Suzuki [56] we introduce a hypothetical scalar part to the effective four-fermion interaction hamiltonian that links the τ to quark densities:

$$\mathcal{H}_{int} = \frac{G\cos\theta_C}{\sqrt{2}} \left[\left(\bar{d}\gamma_\lambda(1-\gamma_5)u\right) \left(\bar{\nu}_\tau\gamma^\lambda(1-\gamma_5)\tau\right) + \epsilon_s \left(\bar{d}u\right) \left(\bar{\nu}_\tau(1+\gamma_5)\tau\right) \right] + h.c., \tag{5.6}$$

where ϵ_s parameterizes the strength of the scalar interaction. The total hadronic decay rate of the tau through the scalar interaction is related to the electronic decay rate by [56]

$$\frac{\Gamma(\tau^- \to \nu_\tau (hadrons)^-_{scalar})}{\Gamma(\tau^- \to \nu_\tau e^- \bar{\nu}_e)} = \frac{3}{8}\,\epsilon_s{}^2 \times (phase\ space\ factor) \simeq 0.2\,\epsilon_s{}^2. \tag{5.7}$$

Current-algebra and nonrelativistic quark model calculations [56] lead us to believe that other possible final states (5π, $\rho\omega$, $K\bar{K}\pi\pi$) are not competitive with $\pi\eta$ and $K\bar{K}$. Assuming therefore that resonant and nonresonant production of the $\pi\eta$ and $K\bar{K}$ modes saturate the decay of $(u\bar{d})_s$, we can limit the strength of a such a scalar contribution. Using the experimental value $BR(\tau^- \to \nu_\tau e^- \bar{\nu}_e) = 17.7\%$ [5] and the conservative value for $\mathcal{R}$ given in Equation 5.3, we find

$$\epsilon_s{}^2 < 0.5. \tag{5.8}$$

5.4 Additional Results Involving the a_0

If we continue to assume that that the $\pi\eta$ and $K\bar{K}$ modes are the only important decay modes of the a_0, then the conservative bound on the rate-ratio $\mathcal{R}$

(Equation 5.3) implies a branching ratio $BR(a_0 \to K\bar{K}) > 16\%$. Then our limit (Equation 5.2) leads to

$$BR(\tau^- \to \nu_\tau a_0^-(980)) < 1.6\%. \tag{5.9}$$

The weak decay constant of the a_0, f_{a_0}, may be defined by analogy with the pion decay constant from the hadronic matrix element

$$< 0|J_\mu^s|a_0^+(p) >= f_{a_0} p_\mu, \tag{5.10}$$

where J^s is the hadronic second-class vector current. The expected rate for the second-class decay $\tau \to \nu a_0$ is then related to that for the allowed decay $\tau \to \nu\pi$ by [32]

$$\frac{\Gamma(\tau^- \to \nu_\tau a_0^-)}{\Gamma(\tau^- \to \nu_\tau \pi^-)} = \frac{(1 - m_{a_0}^2/m_\tau^2)^2 f_{a_0}^2}{(1 - m_\pi^2/m_\tau^2)^2 f_\pi^2} = 0.70 \frac{f_{a_0}^2}{f_\pi^2}. \tag{5.11}$$

In this expression the small expected rate for $\tau \to \nu_\tau a_0$ is reflected in a small value of f_{a_0}; that is, a small rate for a_0 decaying to leptons only (a reaction that has never been observed.) Thus the ratio f_{a_0}/f_π is a measure of the relative size of the second-class current. Using Equation 5.9 and the current world average $BR(\tau \to \nu_\tau \pi) = 11.0\%$, we arrive at

$$\frac{f_{a_0}^2}{f_\pi^2} < 0.3. \tag{5.12}$$

Chapter 6

Measurements of Three-Prong Branching Fractions

THE SO-CALLED ONE-PRONG PROBLEM of τ-lepton decays (see Chapter 2) has dominated the discussion of τ physics for several years. Yet there are other areas of the field that remain relatively unexplored. To date the smallish branching fractions of the τ to three-prong modes containing kaons have been only poorly measured, with only one limit and one low-statistics measurement published. These kaon-containing modes are interesting because they can shed light on the mesonic content of the W propagator (see Chapter 2). This chapter reports an attempt to add a new measurement of comparable quality to the existing one.

The analysis reported in this chapter uses exclusively the charged-track information reported by the TPC central tracking chamber, and explicitly excludes information from the PEP4/9 calorimeters; the statistics of this experiment are so low as to preclude their effective use. When reference is made to the $K\pi\pi$ branching mode, we mean a final state composed of three charged tracks, two of which are pions and one a kaon, and an unspecified number of associated neutral particles.

6.1 History

In 1984 the TPC/2γ collaboration published a limit [64, 65] on the sum of all kaon-containing three-prong modes:

$$BR(\tau^- \to \nu_\tau K^- + 2\text{ charged} + \text{neutrals}) < 0.6\%\ (90\%\ \text{CL}). \tag{6.1}$$

This limit was based on the low-field TPC data set of 77 pb^{-1} (see Chapter 3). These data were consistent with a measurement

$$BR(\tau^- \to \nu_\tau K^- + 2\text{ charged} + \text{neutrals}) = 0.3\% \pm 0.2\% \pm 0.1\%, \tag{6.2}$$

at a level of significance deemed insufficient for publication.

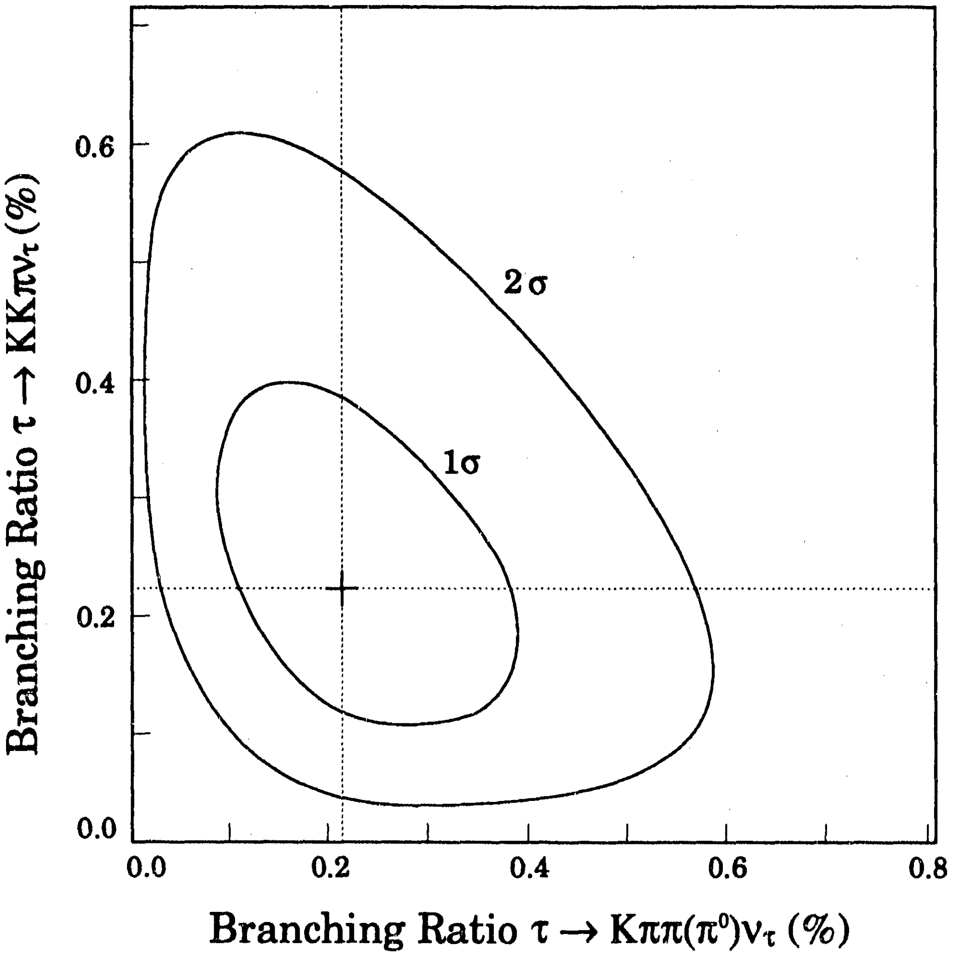

Figure 6.1: Probability contour for the 1986 DELCO measurements of $BR(\tau^- \rightarrow \nu_\tau K^-\pi^+\pi^-(\pi^0))$ and $BR(\tau^- \rightarrow \nu_\tau K^-K^+\pi^-)$; from Ref. [66].

The only published measurement to date of these kaon-containing modes is that of the DELCO collaboration in 1986 [66] based on 150 pb^{-1} of e^+e^- data taken at PEP. They presented the central values

$$\begin{aligned} BR(\tau^- \rightarrow \nu_\tau K^-\pi^+\pi^-(\pi^0)) &= (0.22^{+0.16}_{-0.13})\% \\ BR(\tau^- \rightarrow \nu_\tau K^-K^+\pi^-) &= (0.22^{+0.17}_{-0.11})\% \end{aligned} \tag{6.3}$$

and a confidence contour for these correlated values (see Figure 6.1). In addition, based on four well-identified events in the high-mass mode $\tau^- \rightarrow \nu_\tau K^-K^+\pi^-$, they published what was then the best upper limit on the mass of the tau neutrino [67]. The TPC/2γ collaboration now has on hand a dataset comparable in size to that which DELCO had in 1986, with superior tracking and particle identification information.

6.2 Plausibility

The 1984 TPC/2γ paper [64] fell short of reporting a statistically significant signal for kaon-containing three-track τ decays. The addition of the 1986 high-resolution data set makes such a measurement possible. Figure 6.2 shows a map of the distribution of ionization energy loss rate vs. momentum for the three-prong tracks in high-field events passing the τ_{1+3} event selection cuts described in Chapter 4. There is a clear population of tracks in the kaon region at high momentum.

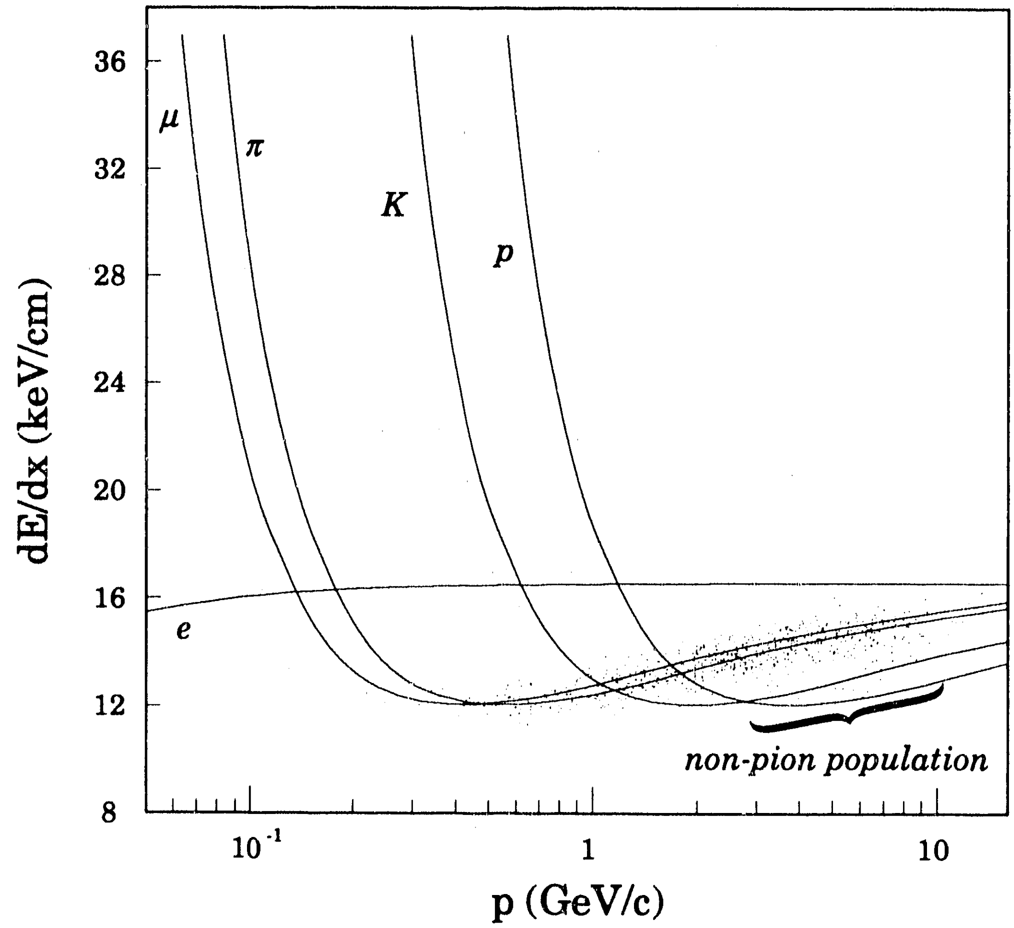

Figure 6.2: $\mathrm{d}E/\mathrm{d}x$ vs. $\log(p)$ for three-prong tracks in events passing τ_{1+3} event selection cuts. A population of kaon candidates is visible below the pion line at high momentum.

A rough estimate of the number of non-pion tracks in this region can be found by histogramming the quantity $\Delta = (I - I_\pi)/(I_K - I_\pi)$ computed for each track in the sample. Here I is the ionization rate $\mathrm{d}E/\mathrm{d}x$ measured for the track, and I_π and I_K are the expected ionization rates for true pions and kaons at the track's measured momentum. A population of pions will peak at $\Delta = 0$; kaons will peak at $\Delta = 1$. The distribution of Δ for the three-prong tracks in the high-field sample (excluding tracks that lie too close to the π/K crossover, where $I_K = I_\pi$) is shown in Figure 6.3. The histogram exhibits a pion peak at $\Delta = 0$ and a non-pion shoulder near $\Delta = 1$. If we subtract the bins for which $\Delta < 0$ from those for which $\Delta > 0$, we are left with a peak in which there are about 21 non-pions.

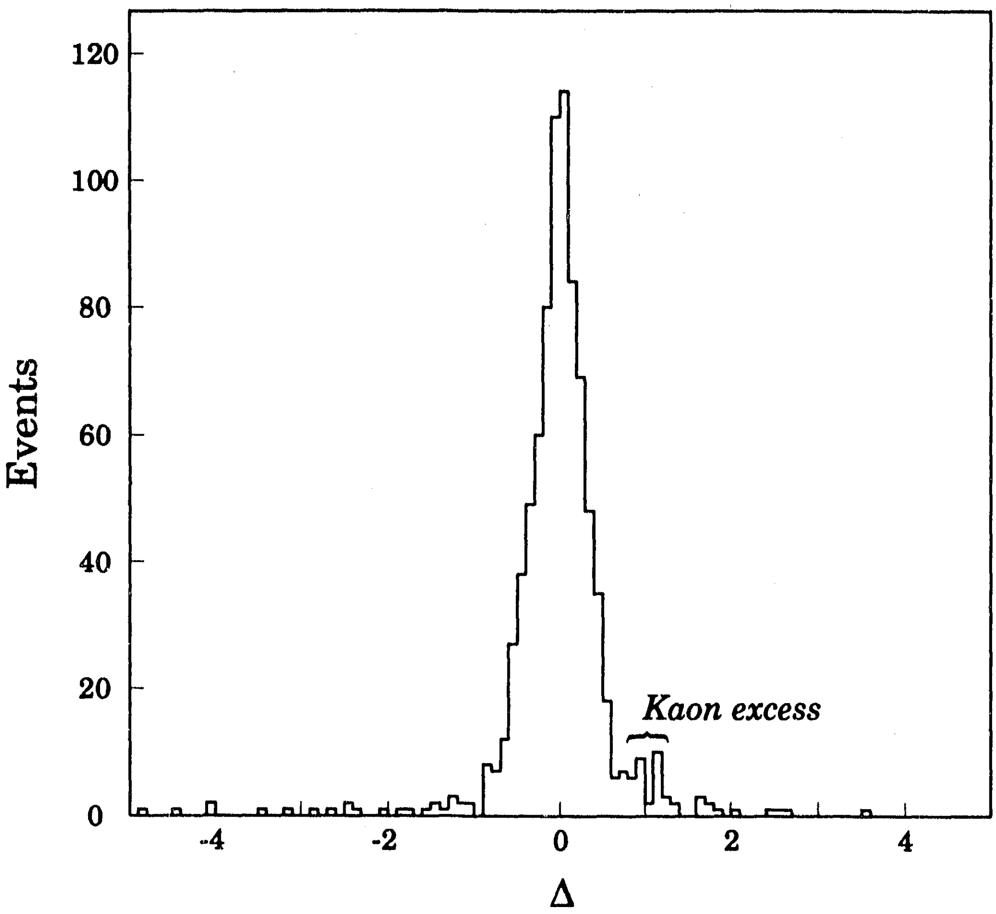

Figure 6.3: $(I - I_\pi)/(I_K - I_\pi)$ for three-prong tracks in the high-field τ_{1+3} sample.

In this sparsely populated region of high-momentum tracks, it is not altogether clear that these non-pion tracks are all kaons, and not protons produced in some background process[1]. One could imagine, for example, that these tracks could contain protons generated in $q\bar{q}$ events of unusually low multiplicity. However a Monte Carlo simulation of such events shows that we expect less than one event from this source. Another mechanism by which this sample might be contaminated would be the ejection of protons from the material of the beam pipe or TPC inner

---

[1] Recall from Chapter 2 that the τ mass is insufficient to allow proton pair-production among its decay products, while the production of single protons is forbidden by baryon number conservation.

pressure wall by incident pions. These would be positively charged protons, never antiprotons, because they originate in the nuclei of ordinary matter. But of the tracks in the ambiguous region below the kaon line in Figure 6.2 six are positively charged and ten are negative; there is clearly no excess of protons. In addition, Monte Carlo simulations of this process show that the momentum spectrum of ejected protons ends below the π/p crossover. These arguments lead us to believe that the estimate of 21 kaons in the high-field data set is reasonably good.

The pion population in this data sample is so large, and the π/K separation in the high-momentum region so small, that one cannot hope to obtain a large, pure sample of kaon-containing events by the application of strong particle identification cuts. In particular, when one requires that two or three tracks each be well-identified as one species or another, the efficiency for this selection is so small that only a few events remain. Therefore we attempt instead to make use of all of the information present in the dataset and show a *statistical* separation between the track species and among the possible decay modes. In the remainder of this chapter we will present two statistical counting methods by which we intend to account for the kaons in the three-prong track sample at the single-event level. Certain mathematical details of the counting methods are left to the appendices.

6.3 Analysis cuts

The selection cuts described in Chapter 4 provide adequate background rejection for analyses (such as that of Chapter 5) in which sensitivity to backgrounds is limited. In this analysis, however, the signal will consist of a very few events, and the mathematical formalism will rely heavily on the assumption that the analyzed event sample contains no tracks that are not pions or kaons and no events that are not tau decays. We therefore impose additional cuts that define a restricted sample of well-measured and background-free events. The events in the restricted sample meet the following criteria:

1. Each event contains exactly **four** reconstructed tracks. (Recall that under the topological selection cuts of Chapter 4, events could contain up to 10 reconstructed tracks if the additional tracks missed the event vertex or were members of geometrically reconstructed e^+e^- pairs.)

2. Each of the three-prong track candidates must be a reasonable match to either the kaon or the pion mass hypothesis; we require $\chi^2_\pi < 9$ or $\chi^2_K < 9$.

3. Each of the three-prong track candidates must have at least **80** useable wire clusters contributing to its $\mathrm{d}E/\mathrm{d}x$ measurement. There is an exception to this cut: if a track has momentum < 1.2 GeV/c, and $\chi^2_e > 4$, it is considered to be unambiguously identified as a pion and is exempt from the cut on the number of wires.

These cuts are important in reducing the QCD background to reasonable levels. 206 low-field events and 283 high-field events remain in the restricted sample. The estimated purity of the restricted sample is 99.5%; Monte Carlo background estimations are given in Section 6.8.

6.4 Matrix Inversion Technique

6.4.1 Overview of the method

The measurement of three-prong branching ratios begins with the restricted event sample described in Section 6.3. Each three-prong track in the restricted sample is called either a pion or a kaon according to a criterion defined in Section 6.4.8 below. Each event is then assigned to a branching mode based on its track assignments. The track assignments incur an error that depends on the detector resolution, the measured parameters of the track and the details of the assignment algorithm. Nevertheless the resolution of the detector is well enough understood and the assignment algorithm simple enough that this error can be unfolded and estimators of the true branching fractions extracted.

6.4.2 True populations

In hadronic decays of the τ, each daughter track actually seen in the detector can only be (barring decays in flight and photon conversions) a charged pion or a charged kaon. This means that the possible three-prong hadronic decay modes of the τ^- are easily enumerable:

$$\begin{array}{l}
\nu_\tau \pi^- \pi^+ \pi^- + \text{neutrals} \\
\nu_\tau K^- \pi^+ \pi^- + \text{neutrals} \\
\nu_\tau \pi^- K^+ \pi^- + \text{neutrals} \\
\nu_\tau K^- K^+ \pi^- + \text{neutrals} \\
\nu_\tau K^- K^- \pi^+ + \text{neutrals} \\
\nu_\tau K^- K^+ K^- + \text{neutrals.}
\end{array} \tag{6.4}$$

(Obviously some of these modes are highly suppressed for physics reasons. A test of the method will be to show that these modes vanish in the unfolded final sample.)

In each event in the sample we index the tracks on the three-prong side and consider them in order, without regard to sign. The ordering of the three tracks is arbitrary, but since the parameters of the track measurement vary from track to track, we must examine them individually. In this scheme there are eight possible combinations of the three tracks' species. Table 6.1 shows how indices can be assigned to each of these modes. We can define an eight-component vector $\boldsymbol{N}$

Index	0	1	2	3	4	5	6	7
Track 1	π	π	π	π	K	K	K	K
Track 2	π	π	K	K	π	π	K	K
Track 3	π	K	π	K	π	K	π	K

Table 6.1: Correspondence of mode indices to possible 3-prong decay modes. Charged tracks are indexed by their (arbitrary) order of appearance in the data record.

whose elements represent the true populations of the possible decay modes:

$$N = \begin{pmatrix} N(\pi\pi\pi) \\ N(\pi\pi K) \\ N(\pi K\pi) \\ N(\pi KK) \\ N(K\pi\pi) \\ N(K\pi K) \\ N(KK\pi) \\ N(KKK) \end{pmatrix} \tag{6.5}$$

where e.g. $N(\pi K\pi) = N_3$ represents the true number of events in the data set in which the first and third indexed tracks are pions and the second is a kaon. For each event a we define a vector N^a that contains only one nonzero element corresponding to the true decay mode. Then the total populations are the sum of the single-event populations:

$$N_j = \sum_{a=1}^{n} N_j^a, \tag{6.6}$$

where n is the number of events in the sample.

6.4.3 Track confusion matrix

Each of the tracks on the three-prong side of an event is assigned to the kaon or pion species according to some criterion (to be described in Section 6.4.8). In making that assignment there is some probability of misidentification. Consider track number $\alpha \in [1,2,3]$ in event number $a \in [1,\ldots,n]$, where n is the number of events in the τ_{1+3} sample that pass all analysis cuts. All the measured quantities for that track, including the momentum and dE/dx resolution, are referred to collectively as p_α. Then the probability of labeling track track α as belonging to species i' when it in fact belongs to species i is denoted by $Q^a_{ii'}(p_\alpha)$, or $Q^{a\alpha}_{ii'}$. The 2×2 matrix of values $Q^{a\alpha}_{ii'}$ in which i and $i' \in [0,1] = [\pi, K]$ each take on values corresponding to pion and kaon hypotheses is written $Q^a(p_\alpha)$. This matrix Q is known as the *track confusion matrix* for track α. Conceptually we assign the code-values π and K to the indices i and i' such that $Q^a_{K\pi}(p_\alpha)$ is the probability that a true pion with measurement variables p_α would be misidentified by our criteria as a kaon, and so forth. It should be emphasized that we will need to compute the elements of Q separately for every track in the sample, as they will depend in general on the measured track quantities and their resolutions.

6.4.4 Event confusion tensor

The confusion among track species represented by Q leads to a confusion among decay modes when the track assignments are used to assign the event to a decay mode. This confusion about the identity of the event is represented by a six-dimensional tensor $\underline{\boldsymbol{P}}$ that is related quite simply to the matrices $\boldsymbol{Q}$:

$$\underline{\boldsymbol{P}}^{a}{}_{ii'jj'kk'} \equiv Q^{a,\alpha=1}_{ii'} \times Q^{a,\alpha=2}_{jj'} \times Q^{a,\alpha=3}_{kk'}. \tag{6.7}$$

Here again a is the event index, α is the track index, and i, i', j, j', k, and k' are species indices running from 0 to 1 for π and K. Here we are making the implicit assumption that the track identification algorithm has been chosen in such a way as to make the misidentification probabilities for the three tracks in an event mutually independent.

The definition 6.7 can be reexpressed in tensor notation as an *outer product* of the matrices $\boldsymbol{Q}$:

$$\underline{\boldsymbol{P}}^{a} \equiv \boldsymbol{Q}^{a}(p_{\alpha=1}) \otimes \boldsymbol{Q}^{a}(p_{\alpha=2}) \otimes \boldsymbol{Q}^{a}(p_{\alpha=3}). \tag{6.8}$$

We anticipate that in order to unfold the confusion represented by $\underline{\boldsymbol{P}}$, we will need to form its inverse. Once $\underline{\boldsymbol{P}}$ is written in the form of Equation 6.8, its inverse is manifest because of the inversion property of the outer product:

$$(\underline{\boldsymbol{P}}^{a})^{-1} = (\boldsymbol{Q}^{a}(p_1))^{-1} \otimes (\boldsymbol{Q}^{a}(p_2))^{-1} \otimes (\boldsymbol{Q}^{a}(p_3))^{-1}. \tag{6.9}$$

Here it is clear that we will need to avoid situations in which the track confusion matrices $\boldsymbol{Q}$ become singular, as might occur in the ambiguous regions of $\mathrm{d}E/\mathrm{d}x$ space. The resolution of this problem is discussed in Section 6.4.7.

The tensor $\underline{\boldsymbol{P}}$ has $2^6 = 64$ elements. Our choice of mode indices listed in Table 6.1 allows us to collapse the sextupally-species-indexed $2 \times 2 \times 2 \times 2 \times 2 \times 2$ tensor $\underline{\boldsymbol{P}}$ to an 8×8 doubly-mode-indexed matrix $\boldsymbol{P}$ by use of binary encoding:

$$P^{a}_{rs} \equiv Q^{a,\alpha=1}_{ii'} \times Q^{a,\alpha=2}_{jj'} \times Q^{a,\alpha=3}_{kk'} \tag{6.10}$$

with

$$\begin{aligned} r &= 4i + 2j + k \\ s &= 4i' + 2j' + k'. \end{aligned} \tag{6.11}$$

$\boldsymbol{P}^{a}$ is called the *event confusion matrix* for event a. In actual computation, we use the matrix form 6.10 to arrive at an estimator of the true branching modes based on a measured sample, and the tensor form 6.9 to find the inverse, as it involves the trivial inversion of three 2×2 matrices rather than a more difficult 8×8.

6.4.5 Observed population

The experimentally observed population in each decay mode is represented in exact analogy to 6.5:

$$\boldsymbol{M} = \begin{pmatrix} M(\pi\pi\pi) \\ M(\pi\pi K) \\ M(\pi K\pi) \\ M(\pi KK) \\ M(K\pi\pi) \\ M(K\pi K) \\ M(KK\pi) \\ M(KKK) \end{pmatrix} \tag{6.12}$$

where each M is the *observed* population of events assigned to the corresponding mode. Then the expected value of $\boldsymbol{M}$ (for a given event) is related to $\boldsymbol{N}$ by

$$\boldsymbol{M}^a = \boldsymbol{P}^a\boldsymbol{N}^a; \tag{6.13}$$

that is, the vector of observed mode populations is the vector of true populations confused by the event confusion matrix $\boldsymbol{P}$.

6.4.6 Branching mode estimator

The estimator of the true population vector $\boldsymbol{N}^a$ is obtained from Equation 6.13 by matrix inversion:

$$\widehat{\boldsymbol{N}}^a = (\boldsymbol{P}^a)^{-1}\boldsymbol{M}^a. \tag{6.14}$$

Event by event, the elements $\widehat{N}_j^a$ can be positive or negative, but they must sum to 1.

The estimator of the branching mode population vector for the sample as a whole is by analogy with Equation 6.6

$$\mathrm{E}[\boldsymbol{N}] \equiv \widehat{\boldsymbol{N}} = \sum_{a=1}^{n} \widehat{\boldsymbol{N}}^a. \tag{6.15}$$

In a sufficiently large sample the negative elements N_j^a should cancel against positive ones to give estimators $\widehat{N}_j$ that are statistically positive for all nonzero branching modes. (This assertion is borne out in Monte Carlo runs.)

6.4.7 Covariance matrix

The errors on and correlations among the estimators $\widehat{N}_j$ are expressed in the covariance matrix

$$\mathrm{V}[\widehat{N}_j^a, \widehat{N}_{j'}^a] = \sum_{\text{modes } k} (P^a)^{-1}_{jk}(P^a)^{-1}_{j'k}M_k^a. \tag{6.16}$$

(This form is derived in Appendix B.) In each event a, only one element M_k^a is nonzero, since the event is assigned to only one branching mode. Thus we can assign the symbol k_a to the nonzero element's index and collapse the sum, using $M_k^a = \delta_{kk_a}$:

$$\mathrm{V}[\widehat{N_j^a}, \widehat{N_{j'}^a}] = (P^a)^{-1}_{jk_a}(P^a)^{-1}_{j'k_a}. \tag{6.17}$$

From the form 6.17 it is clear that only column k_a in the inverse event confusion matrix $(\boldsymbol{P}^a)^{-1}$ need be computed.

Since the inverse event confusion matrix elements P_{jk}^a appear in the square in 6.17, it is important that the matrix $\boldsymbol{P}^a$ depart from the unit matrix as little as possible. (This is why the track identification criterion described in Section 6.4.8 is chosen to represent a reasonable guess about the true species of each track, despite the fact that any arbitrary but well-defined criterion would have worked.) Highly ambiguous events (such as those in which one or more tracks fall very close to the π/K crossover in $\mathrm{d}E/\mathrm{d}x$ space) can contribute large errors to the population estimators $\widehat{N_j}$. Our original approach was to exclude events with tracks in the ambiguous region from the sample, at the cost of lowering statistics and adding systematic differential acceptance effects; see Section 6.9. In this case there is a tradeoff between increased statistics and decreased ambiguity, leading to some optimum cut at which the total error is minimal. However in practice we discovered that no kaon-production mechanism we modeled generated kaons below 1.2 GeV/c in momentum, so that all tracks falling in and below the crossover region can be safely called unambiguous pions. Figure 6.4 shows the distribution of inverse matrix elements $(P^a)^{-1}_{jk}$ in the events in the restricted high-field sample. The distribution is strongly peaked at zero and one and has no high-weight outliers. The sharply-peaked structure reflects the lack of ambiguity in most events; the proper event-class assignment is usually clear.

6.4.8 Track classification algorithm

The track classification algorithm is in principle arbitrary; all that is required is that the track confusion matrix $\boldsymbol{Q}^a$ be calculable in some way based on the measurement parameters p_α. In order to minimize the overall errors associated with the unfolding procedure, however, we choose a classification procedure that makes the correct choice most of the time. In addition, by choosing a procedure based on the well-understood properties of $\mathrm{d}E/\mathrm{d}x$ measurement in the TPC, we can derive an analytical expression for the elements of $\boldsymbol{Q}^a$ without resort to a Monte Carlo calculation.

Each track is measured in the TPC with a momentum p and ionization energy loss rate I (see Chapter 3). The momentum and $\mathrm{d}E/\mathrm{d}x$ resolutions σ_p and σ_I can also be estimated from the track measurement. The trajectory $I_s(p)$ of the expected ionization rate for track species s is well known for the TPC. Armed with this information we compute a χ^2 measure χ_s^2 that represents the distance of the

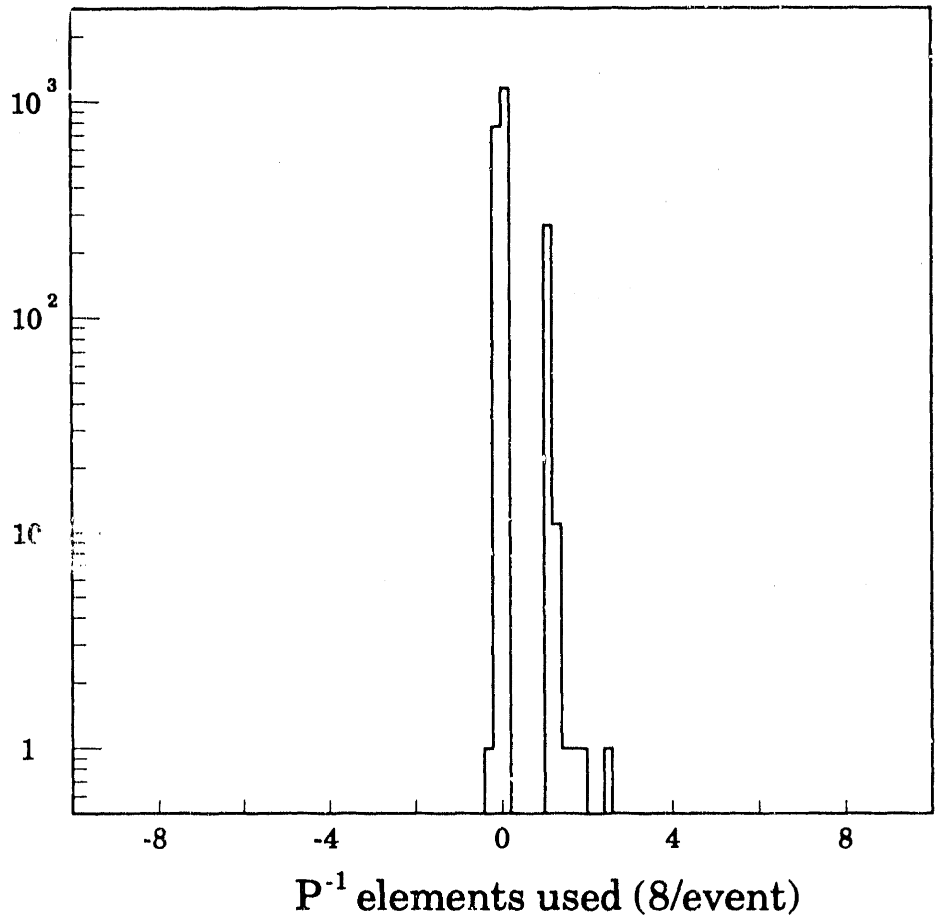

Figure 6.4: Histogram of the elements of the inverse event-confusion matrix $(P^a)^{-1}_{jk}$ used in computing the covariance matrix for events in the restricted high-field sample. Eight matrix elements from each event contribute to the total combinatoric error. No element exceeds 3.

measured point (p, I) from the species trajectory $I_s(p)$ for each species hypothesis s, measured in units of the measurement resolution.

A track is called a kaon if it satisfies

$$\chi^2_K + b^2 < \chi^2_\pi; \tag{6.18}$$

that is, if the kaon hypothesis is sufficiently more attractive than the pion hypothesis. Here b^2 is a parameter whose value is arbitrary; in practice the best results (smallest overall errors) are obtained with $b^2 \approx 2$. The sign of b^2 is taken to be positive because of our *a priori* knowledge that pions are more common than kaons in our sample.

The measurement of ionization energy loss $\mathrm{d}E/\mathrm{d}x$ in the TPC is known to be gaussian to more than 3σ with a resolution that is well understood as a function of the measurement parameters p_α [55]. The detailed shape and position of the expected $\mathrm{d}E/\mathrm{d}x$ trajectories $I_s(p)$ are also well known. Changes in the values of χ^2_s arising from the small momentum resolution σ_p can be safely ignored compared to the effects of the $\mathrm{d}E/\mathrm{d}x$ resolution in the momentum range that contains most of the tracks in our sample (see Section 6.10). Therefore to an excellent approximation we may compute the track confusion probabilities $Q^{a\alpha}_{ii'}$ as integrals under a gaussian probability distribution centered at $\langle I_s(p_m)\rangle$, where p_m is the measured track momentum. The analytical forms of the track confusion probabilities are derived in Appendix A.

Application of the matrix inversion technique to the high-field and low-field data samples yields estimates of the numbers of events in each decay mode. The populations found in each decay mode are listed below in Table 6.2. The results are stable with respect to changes in the cut quantity b^2 over the range $1 < b^2 < 8$, and are insensitive to changes in the analysis cuts. In Section 6.7 we will compare the numbers of events obtained with the matrix inversion method to those found using another technique.

6.5 Weighted Physics Distributions

The matrix inversion method provides in addition to event-counting the ability to generate estimators for the distributions of arbitrary physics quantities broken down by event or track type. One can find (for example) the estimated momentum spectrum for kaons in our sample by histogramming each track's momentum weighted by a kaon weight calculated for that track. The kaon weight is just the appropriate element in the inverse track confusion matrix $\boldsymbol{Q}^{-1}$. Similarly one finds an estimate of the invariant mass spectrum for $KK\pi$ events by weighting each event's three-prong invariant mass by the appropriate elements in the inverse event confusion matrix $\boldsymbol{P}^{-1}$.

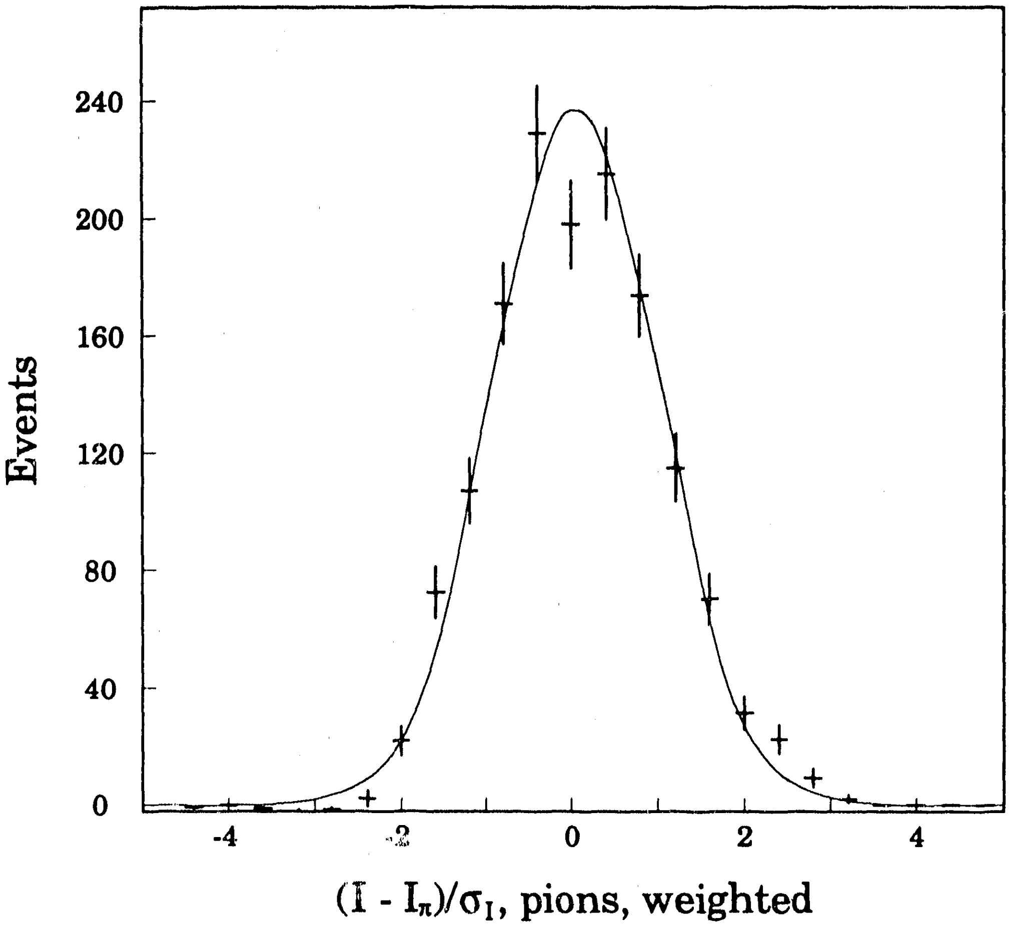

Figure 6.5: Weighted distribution of dE/dx measurements for pions in the restricted sample. The quantity shown is $(I - I_\pi)/\sigma_I$.

6.5.1 dE/dx distribution

This powerful technique allows us to make certain checks on the matrix inversion method. For example, the method relies heavily on the assumption that the distribution of dE/dx measurements is gaussian for any single species. Event weighting allows us to display an estimate of the distribution of dE/dx measurements for pions only; the weighted distribution is shown in Figure 6.5. The quantity histogrammed is $(I - I_\pi)/\sigma_I$, ideally a gaussian of width 1 centered at the origin. A gaussian fit to the histogram has its center at 0.06 ± 0.04 and width 1.02 ± 0.1.

6.5.2 Sign correlations

A second check on the method comes from weighted track-sign correlations. In $K\pi\pi$ decays, we expect a τ^- to decay via W^- to $u\bar{s}$ and thence to $K^-\pi^+\pi^-$; the

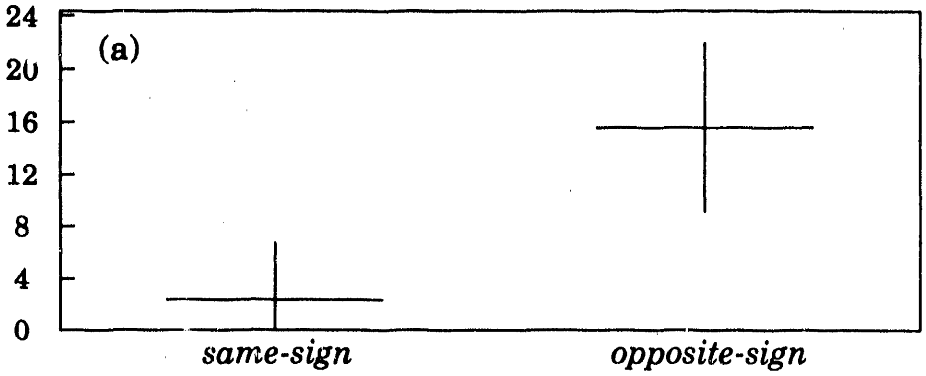

Pion pairs in Kππ events

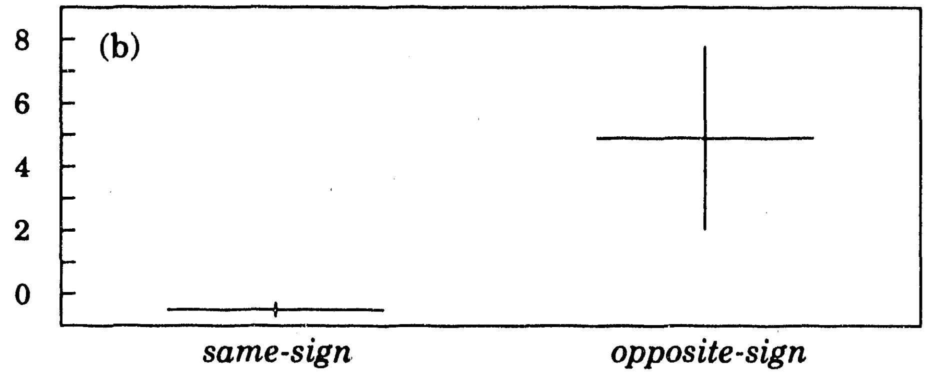

Kaon pairs in KKπ events

Figure 6.6: Sign anticorrelation of (a) pion pairs in $K\pi\pi$ events and (b) kaon pairs in $KK\pi$ events.

sign of the kaon should always match that of the parent τ, and the signs of the pions should balance. Similarly $KK\pi$ final states arise from an $s\bar{s}$ pair pulled from the vacuum, so we expect the kaon signs to be opposite while the pion carries the sign of the τ. The track-species and event-mode assignments were made without reference to the sign of the tracks; thus an observation of sign correlations will serve as a check on the matrix inversion algorithm. Figure 6.6 shows the weighted track sign behavior of pion pairs in $K\pi\pi$ events in the restricted sample. The number of same-sign pion pairs in these events is consistent with zero, as expected from our simple quark-model argument. Kaon pairs in weighted $KK\pi$ events also are consistent with our expectation of 100% sign anticorrelation (Figure 6.6).

6.5.3 Invariant masses

Another application of weighted physics distributions is the display of invariant mass spectra for particular branching modes. Of particular interest are various spectra in the $K\pi\pi$ system. (The $\pi\pi\pi$ system is already well-studied, and we see only ~ 4 events in $KK\pi$.) In Figures 6.7 through 6.9 we show weighted invariant mass spectra for $K\pi\pi$ events in our data set, juxtaposed with simulated spectra from various Monte Carlo-generated processes. In each figure (a) represents the weighted mass spectrum from the data; (b) is a Monte Carlo run simulating the process $\tau^- \rightarrow \nu_\tau K^-\pi^+\pi^-$ via phase space; (c) is a Monte Carlo simulation of the resonant decay chain $\tau^- \rightarrow \nu_\tau K_1^-(1270) \rightarrow \nu_\tau K^-\rho^0 \rightarrow \nu_\tau K^-\pi^+\pi^-$; and (d) is a simulation of $\tau^- \rightarrow \nu_\tau K_1^-(1400) \rightarrow \nu_\tau K^{*0}\pi^- \rightarrow \nu_\tau K^-\pi^+\pi^-$. Note that because event weights can be negative, bin occupancies may fall below zero; this is seen particularly in the low-statistics true data sample.

The comparative features of these spectra are more tantalizing than conclusive. The $K\pi\pi$ invariant mass spectrum from the data (Figure 6.7 (a)) shows structure in the neighborhood of 1400 MeV/c^2 compatible with phase space (b) or $K_1(1400)$ production (d), but there is no evidence of peaking around 1270 MeV/c^2 as would be required by the presence of the narrower $K_1(1270)$ (with full width $\sim$ 90 MeV/c^2 [5]). The $K^-\pi^+$ invariant mass spectrum (Figure 6.8) helps little; all three Monte Carlo spectra peak in the neighborhood of the K^* mass, as the data does. In the $\pi^-\pi^+$ spectrum, the peaking in the data (a), though near the ρ mass at 770 MeV/c^2, is clearly broader than that expected in ρ-dominant decays (c), and again more closely resembles phase space (b) or $K_1(1400)$ production (d). Although the limited statistics preclude a firm statement, the data suggest that production of $K_1(1270)$ (with its currently estimated parameters) is not a leading source of τ decays to $K\pi\pi$.

6.6 Extended Maximum Likelihood Method

The matrix inversion method is valuable in that it yields weighted events that can be used to generate estimators for physics distributions, but the errors it yields are only parabolic, which we know to be inadequate for such small event samples as ours. As a means of obtaining better (asymmetrical) errors on the branching fraction estimates, and as a check on the matrix inversion technique, we introduce a parallel analysis scheme making use of an *extended maximum likelihood* method [57].

The difference between the extended maximum likelihood technique for parameter estimation and the standard likelihood technique is that in the extended maximum likelihood paradigm, the total number of events observed is itself treated as a parameter to be determined by the minimization procedure. Because of this, the errors obtained from the fit reflect not only the errors associated with untangling a confused event sample, but also the errors of Poisson statistics.

We construct a likelihood function based once again on the assumption that each track is selected from a parent distribution that is gaussian in dE/dx. (Because the momentum spectrum is mode-dependent, we treat it as an unmeasured

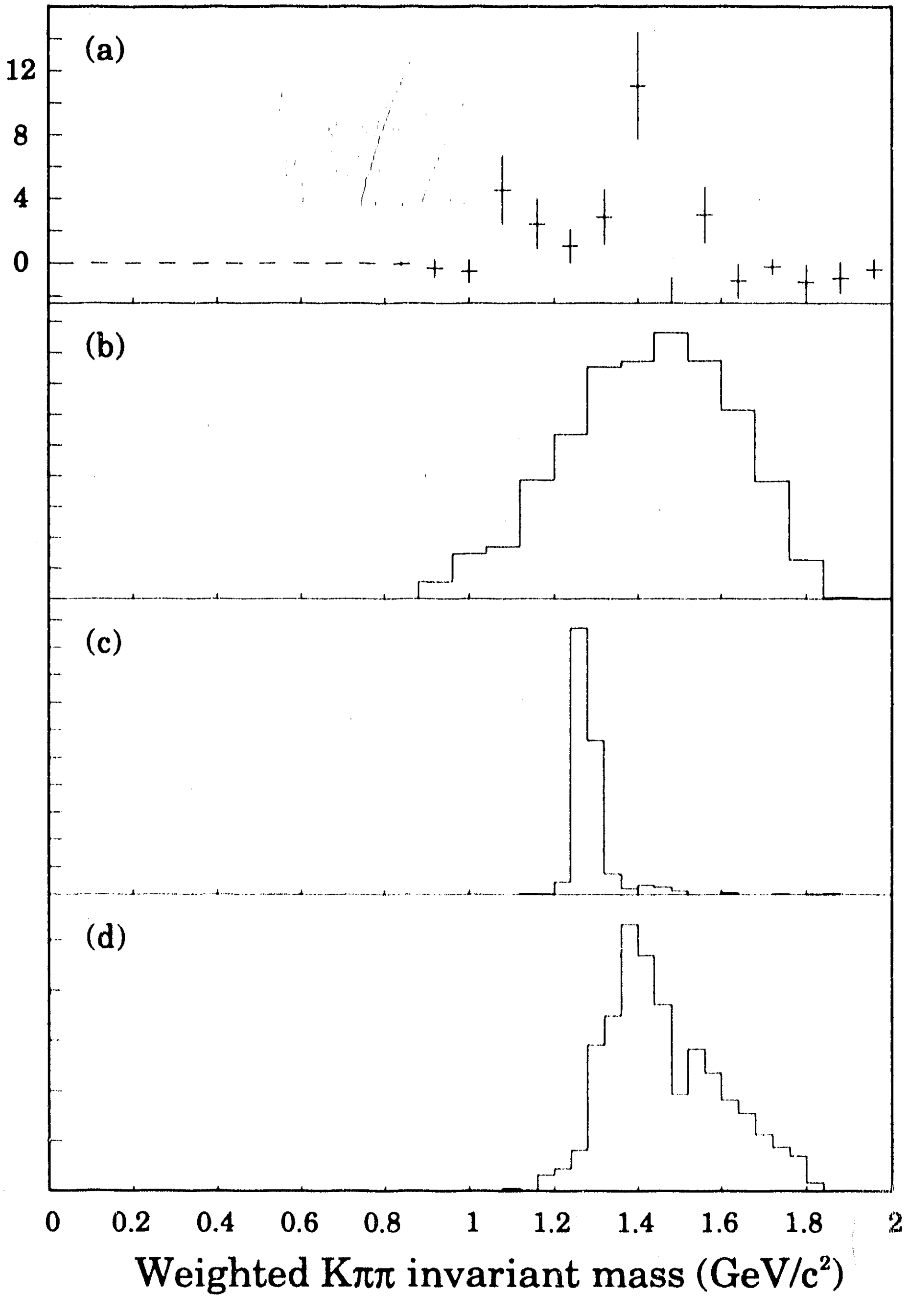

Figure 6.7: Event-weighted $K^-\pi^+\pi^-$ invariant mass spectrum in $K\pi\pi$ events. The spectrum obtained from the data (a) is shown with Monte Carlo simulations of three decay hypotheses: (b) phase space, (c) $\tau^- \to \nu_\tau K_1^-(1270) \to \nu_\tau K^- \rho^0$; and (d) $\tau^- \to \nu_\tau K_1^-(1400) \to \nu_\tau K^{*0}\pi^-$.

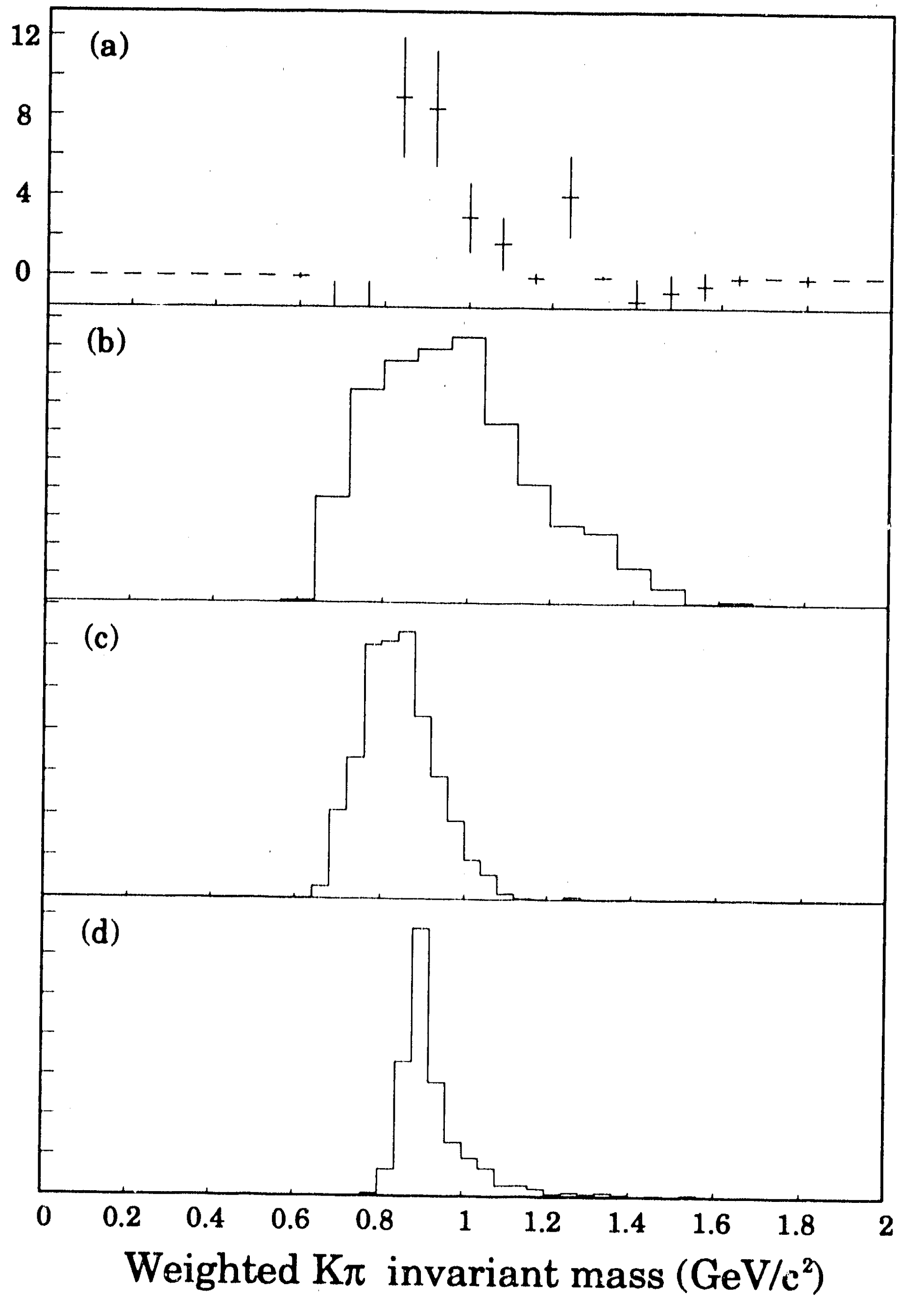

Figure 6.8: Event-weighted $K^-\pi^+$ invariant mass spectrum in $K\pi\pi$ events. The sources of the four spectra are the same as those of Figure 6.7.

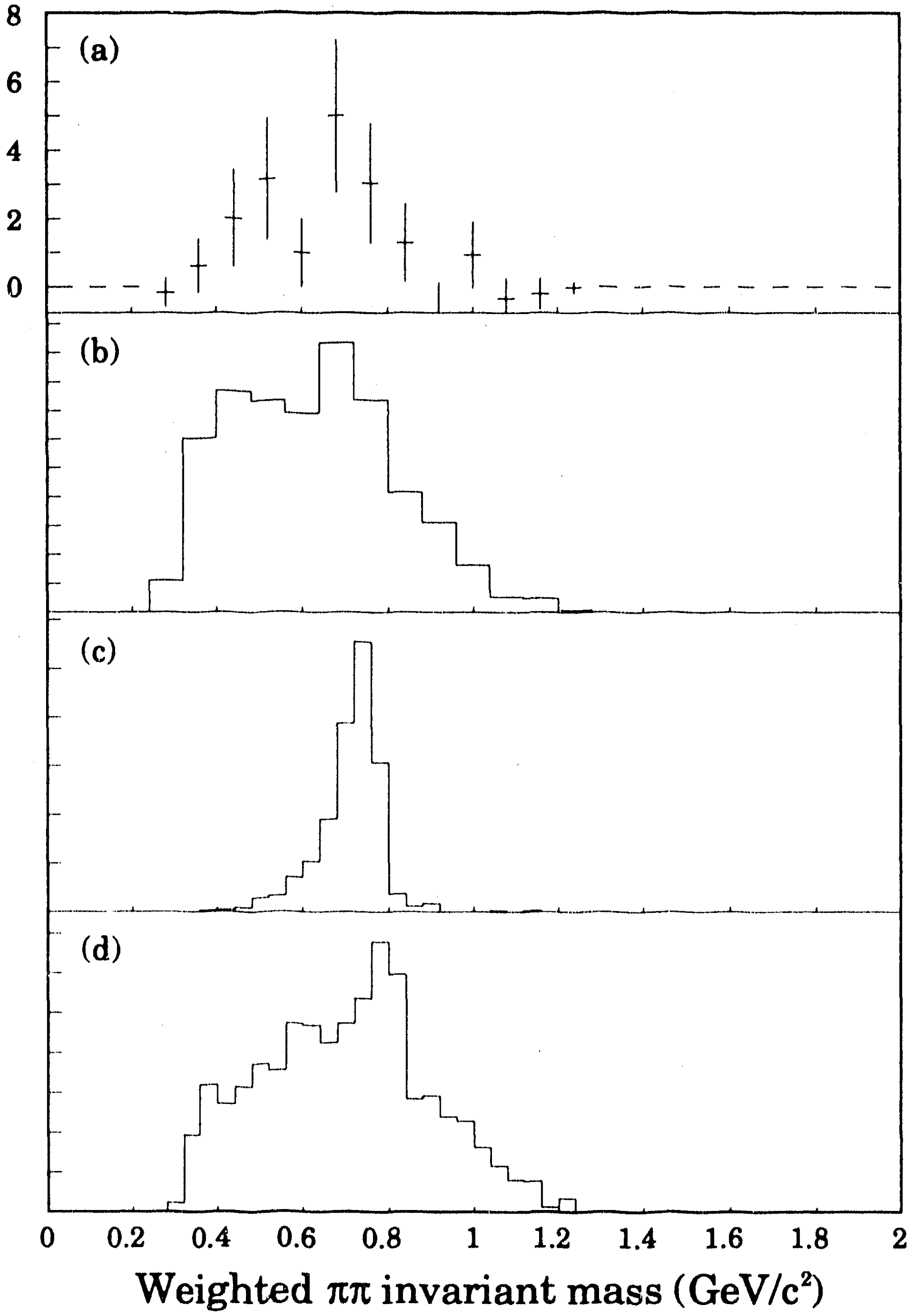

Figure 6.9: Event-weighted $\pi^-\pi^+$ invariant mass spectrum in $K\pi\pi$ events. The sources of the four spectra are the same as those of Figure 6.7.

variable in constructing the likelihood function.) The probability density function (PDF) for observing the measured dE/dx for track i, I_i, if its true species is α, is

$$f(I_i|\alpha)dI_i = \frac{1}{\sqrt{2\pi}\sigma_\alpha} \exp\left(-\frac{(I_i - I_\alpha)^2}{2\sigma_\alpha^2}\right) dI_i. \tag{6.19}$$

Here σ_α is the dE/dx resolution for the measured track assuming that it belongs to species α. The joint PDF for observing all three tracks at their measured values, given that they belong to species α_1, α_2, and α_3, respectively, is

$$\begin{aligned} f(I_1, I_2, I_3|\alpha_1, \alpha_2, \alpha_3)dI_1dI_2dI_3 &= \frac{dI_1dI_2dI_3}{(2\pi)^{\frac{3}{2}}\sigma_{\alpha_1}\sigma_{\alpha_2}\sigma_{\alpha_3}} \\ \times \exp\left(-\frac{(I_1 - I_{\alpha_1})^2}{2\sigma_{\alpha_1}^2}\right) &\exp\left(-\frac{(I_2 - I_{\alpha_2})^2}{2\sigma_{\alpha_2}^2}\right) \exp\left(-\frac{(I_3 - I_{\alpha_3})^2}{2\sigma_{\alpha_3}^2}\right), \end{aligned} \tag{6.20}$$

where again we have made use of the independence of the track measurements.

The observed events belong to a true decay-mode population $\boldsymbol{N}$ (described in Section 6.4.2). The tracks are drawn from a sum of distributions of the form of Equation 6.20 with coefficients proportional to the values we are trying to estimate, the parent branching mode populations N_j. This track distribution is

$$F(I_1, I_2, I_3|\boldsymbol{N}) = \frac{1}{n} \sum_{\text{modes } j} N_j f(I_1, I_2, I_3|j), \tag{6.21}$$

where we have combined the three hypothesis-indices α_i in a single mode-index j according to a scheme like that outlined in Table 6.1.

The canonical likelihood function $\mathcal{L}$ is the product of single-event probability density functions:

$$\mathcal{L} = \prod_{a=1}^{n} \left(\sum_j N_j f^a(I_1^a, I_2^a, I_3^a|j)\right). \tag{6.22}$$

In the extended maximum likelihood technique we regard the parameters N_j as random variables themselves, and introduce an additional term to take account of their Poisson statistics:

$$\mathcal{L}_E = \frac{\exp(-\sum N_j)}{(\sum N_j)!}) \prod_{a=1}^{n} \left(\sum_j N_j f^a(I_1^a, I_2^a, I_3^a|j)\right). \tag{6.23}$$

For each data set, the parameters N_j are estimated by adjusting their values until a global minimum of the function $\mathcal{L}_E$ is found. The minimization is performed using the minimization package MINUIT [68]. The results of the fit are described in Section 6.7.

The fitting procedure yields proper asymmetrical errors on the parameters N_j, corresponding to the variations on the parameters necessary to decrease $\mathcal{L}_E$ by a factor $e^{-1/2}$ from its maximum. The errors obtained using the ordinary likelihood function $\mathcal{L}$ (Equation 6.22) refer only to the error generated by the fitting procedure itself; they do not include the statistical error inherent in the measurement, which would have to be appended in some way. By contrast, the errors found by varying the parameters of the extended likelihood function $\mathcal{L}_E$ include the overall statistical error. In addition, the fit provides detailed error contours showing the correlations among the measured branching modes.

6.7 Preliminary Results

We have outlined two distinct techniques for estimating the numbers of events in each three-prong decay mode. Table 6.2 summarizes the numbers of events in each decay mode as determined by the matrix inversion method and by the extended maximum likelihood fit. No background subtraction or acceptance correction has been made at this point. The numbers of events reported by the two methods for each mode agree within errors. Among the 489 events in the restricted data sample, we observe roughly 20 events in the $K\pi\pi$ mode, four in $KK\pi$, and zero in KKK.

	Low-field		**High-field**	
Mode	*Matrix*	*EMLM*	*Matrix*	*EMLM*
$\pi\pi\pi$	198.8 ± 14.7	197.3 ± 14.2	265.9 ± 16.9	263.9 ± 16.5
$K\pi\pi$	6.2 ± 4.6	$7.7\,^{+4.1}_{-3.3}$	13.6 ± 6.4	$15.9\,^{+5.4}_{-4.5}$
$KK\pi$	0.95 ± 1.3	$0.99\,^{+1.4}_{-0.74}$	3.5 ± 2.5	$3.2\,^{+2.4}_{-1.7}$
KKK	0.0 ± 0.01	0.0 ± 0.5	0.0 ± 0.03	0.0 ± 0.5

Table 6.2: Number of events found in each three-prong decay mode, as reported by the matrix inversion method *(Matrix)* and the extended maximum likelihood method *(EMLM)*.

The following sections describe how branching fractions are extracted from these numbers.

6.8 Backgrounds

Events in the 1+3-prong topology are quite distinctive, and difficult to produce through processes other than tau decay. The background levels are therefore correspondingly low. The main backgrounds in the canonically-selected τ_{1+3} sample of Chapter 4 are

- QCD events with low reconstructed charged multiplicity.
- Tau pairs decaying in the 1+1-prong topology with converted photons from π^0s.
- Two-photon events with four charged prongs and no observed electron tags in the final state.
- Bhabha events with associated converted photons.
- Radiative muon pair events with converted photons.

The background contribution from each of these sources is estimated by Monte Carlo simulation of each process followed by a full detector simulation. Table 6.3 shows the expected background levels from these sources in the sample of events surviving the tight τ_{1+3} cuts described in Chapter 4; Table 6.4 refers to the restricted sample of events surviving the analysis cuts of Section 6.3. In both tables negligible sources of background are omitted.

Source	**Low-field**	**High-field**
Data set	585	783
$q\bar{q}$	14.7	19.8
τ_{1+1}	12.6	16.9
$\gamma\gamma$	1.9	2.5

Table 6.3: Estimated backgrounds in the τ_{1+3} data set.

Source	**Low-field**	**High-field**
Data set	206	283
$q\bar{q}$	1.4	1.9
τ_{1+1}	0.5	0.7
$\gamma\gamma$	$<< 1$	$<< 1$

Table 6.4: Estimated backgrounds in the restricted data set.

In this analysis, the most serious sources of background are those that contain kaons (or protons) on the side of the event that mocks a three-prong tau decay. The observed signals are so small that backgrounds at the level of a single event in the $KK\pi$ channel would spoil the statistical significance of the measurement. This is the reason for the introduction of the requirement that the reconstructed charged multiplicity in the event be exactly four (see Section 6.3, requirement 1). With this requirement, the expected background to the $KK\pi$ channel (which comes entirely from QCD events) is less than 0.25 event in each data set. Table 6.5 shows the breakdown of expected background events by mode as reported by the extended maximum likelihood method.

Mode	**Low-field**	**High-field**
$\pi\pi\pi$	1.6	2.1
$K\pi\pi$	0.2	0.3
$KK\pi$	0.1	0.2
KKK	<< 1	<< 1

Table 6.5: Estimated backgrounds to various τ decay modes in the restricted data set.

6.9 Acceptance corrections

The introduction of the charged multiplicity = 4 cut (Section 6.3) unfortunately enhances the differences in acceptance among the various 1- and 3-prong decay modes. Modes on the 1-prong or 3-prong side that contain π^0s pass the selection cuts with markedly lower efficiency than those without π^0s. We allow for the possibility of correlative effects in the acceptance by modelling 1-prong and 3-prong decays together and reporting an acceptance for the combined event type, rather than assuming that the acceptance is separable into a term specific to the 1-prong mode times a term for the 3-prong mode.

Acceptances for various combinations of 1- and 3-prong decay modes were calculated using a Monte Carlo simulation of the events and their interactions with the detector. The array of event selection efficiencies used to transform the number of observed events in each 3-prong channel into the appropriate branching fraction is shown in Table 6.6. Here the event selection efficiency is just the number of events passing both the τ_{1+3} event selection cuts defined in Chapter 4 and the additional analysis cuts of Section 6.3, divided by the number of events generated.

The integrated luminosity acquired by the PEP4/9 experiment is a quantity known only to about 10% accuracy (see Section 6.10). In order to avoid sensitivity to this large systematic uncertainty, we compute the desired branching fractions not by dividing the number of observed events in each mode by the number expected in our data set but by the number of τ_{1+3} events observed. Then to lowest order the integrated luminosity does not enter the calculation of the branching fraction estimators.

Low-field				
3-prong mode	1-prong mode			
	e	$\mu/\pi/K$	ρ	$\pi\pi^0\pi^0$
$\pi\pi\pi$	14.06%	15.54%	10.34%	7.29%
$\pi\pi\pi\pi^0$	9.16%	11.16%	7.53%	4.79%
$K\pi\pi$	12.28%	13.74%	9.57%	6.60%
$KK\pi$	8.34%	10.89%	7.03%	4.50%
KKK	3.12%	3.41%	2.54%	1.58%
High-field				
$\pi\pi\pi$	21.14%	23.20%	16.31%	13.03%
$\pi\pi\pi\pi^0$	15.53%	17.18%	11.99%	8.85%
$K\pi\pi$	20.52%	20.18%	15.29%	11.20%
$KK\pi$	16.99%	16.45%	12.62%	9.90%
KKK	7.03%	8.11%	5.63%	4.20%

Table 8.6: Overall selection efficiencies for major 1– and 3–prong decay combinations.

The branching ratios are computed by comparing the number of events reconstructed in each mode with the total number of τ_{1+3} events in the final sample. The expected number of 1-prong events is

$$N_{1+3} = 2\sum_{\text{expt}} \int \mathcal{L}dt\sigma_{\tau\tau} \sum_{1-\text{prong } i} BR_i \sum_{3-\text{prong } j} BR_j \epsilon_{\text{trig}}(i,j)\epsilon_{\text{sel}}(i,j)\epsilon_{\text{anal}}(i,j), \quad (6.24)$$

where $\int \mathcal{L}dt$ is the integrated luminosity for a given experimental period, $\sigma_{\tau\tau}$ is the tau-pair production cross section at $\sqrt{s} = 29$ GeV, ϵ_{trig} is the trigger efficiency, ϵ_{sel} is the event selection efficiency, and ϵ_{anal} is the efficiency of the analysis cuts. The efficiencies depend in general on the 1- and 3-prong modes and on the experimental period. Similarly the number of events in each three-prong decay mode j is

$$N_j = 2\sum_{\text{expt}} \int \mathcal{L}dt\sigma_{\tau\tau} \sum_{1-\text{prong } i} BR_i BR_j \epsilon_{\text{trig}}(i,j)\epsilon_{\text{sel}}(i,j)\epsilon_{\text{anal}}(i,j). \quad (6.25)$$

We use the world-average values for the various one- and three-prong branching fractions [5] and solve for the desired quantities BR_j.

In the lowest approximation, the exact values of the three-prong branching fractions BR_j that appear in the denominator are not important; we can initially set the branching fractions to $K\pi\pi$ and $KK\pi$ to zero there. We then obtain estimates for the unknown branching fractions and reinsert them in Equation 6.24. The process converges after a few iterations to the figures given in Section 6.11 below.

6.10 Systematic errors

This is a statistics-limited measurement. For completeness, we document here some systematic uncertainties that will become important if the measurement is repeated with higher statistics. The errors reported here refer to a percentage of the measured branching ratio. Sources are listed in roughly decreasing order of importance.

- dE/dx *calibration.* Both the matrix inversion method and the extended maximum likelihood method assume that dE/dx measurements are drawn from a gaussian distribution of well-known center and width. The loci of expected dE/dx values as functions of momentum, $\langle I_s(p)\rangle$, are known to 0.2% [55]. Displacing all of these curves by this amount yields a relative error of 12% in $BR(\tau \to \nu_\tau K\pi\pi)$ and $BR(\tau \to \nu_\tau KK\pi)$.

- dE/dx *resolution.* The dE/dx resolution of the TPC is parameterized as a function of the number of wire samples used in the measurement and of the track dip angle. The relative systematic uncertainty in the parameterized resolution is 8% [55]. Varying the resolution by this amount leads to a relative error of 10% in $BR(\tau \to \nu_\tau K\pi\pi)$ and $BR(\tau \to \nu_\tau KK\pi)$.

- *Background estimation.* The estimated backgrounds reported in Section 6.8 are small compared to the signals. A generous assignment of 100% uncertainty to the background estimates yields an 8% relative error on $BR(\tau \rightarrow \nu_\tau K\pi\pi)$ and a 3% error on $BR(\tau \rightarrow \nu_\tau KK\pi)$.

- *Efficiency estimation.* Systematic over- or underestimation of event selection efficiencies tends to cancel in the determination of branching fractions. An unbalanced error of 10% in the estimated selection efficiency for either of our modes gives a 10% relative error in the corresponding branching fraction.

- *Luminosity.* The integrated luminosity recorded by the TPC in both the high-field and low-field data sets is known to about 10%. In the determination of branching fractions by comparing reconstructed events in particular modes to the total sample of τ_{1+3} events, the luminosity uncertainty cancels to lowest order. It enters only in the relative weighting of the two experimental periods. 10% uncertainty in the luminosity contributes about 0.5% to the relative error on the branching fractions $BR(\tau \rightarrow \nu_\tau K\pi\pi)$ and $BR(\tau \rightarrow \nu_\tau KK\pi)$.

- *Input branching ratios.* Equations 6.25 and 6.24, used in the determination of branching fractions, require world-average values of various τ branching fractions as input. Allowing the branching ratio $BR(\tau \rightarrow$ *1 charged + neutrals*) to vary by its quoted error of 0.4% [5] leads to a relative error of 0.2% in $BR(\tau \rightarrow \nu_\tau K\pi\pi)$ and $BR(\tau \rightarrow \nu_\tau KK\pi)$.

6.11 Branching Fractions

The background-subtracted and acceptance-corrected branching fraction estimates are listed in Table 6.7. Branching fraction estimates from DELCO [66] are included for comparison. The errors quoted are statistical only.

Mode	*EMLM Events*	*Background*	*DELCO BR (%)*	*TPC BR (%)*
$\pi\pi\pi$	470.3 ± 22.0	3.7		
$K\pi\pi$	$23.6^{+6.6}_{-5.7}$	0.5	$0.22^{+0.16}_{-0.13}$	$0.70^{+0.20}_{-0.17}$
$KK\pi$	$4.3^{+2.7}_{-1.9}$	0.3	$0.22^{+0.17}_{-0.11}$	$0.16^{+0.10}_{-0.07}$
KKK	0.0 ± 0.5	$<< 1$		< 0.23 (95% CL)

Table 6.7: Estimated three-prong branching ratios.

The errors determined by the extended maximum likelihood method for the branching fractions $BR(\tau \rightarrow \nu_\tau K\pi\pi)$ and $BR(\tau \rightarrow \nu_\tau KK\pi)$ are correlated and

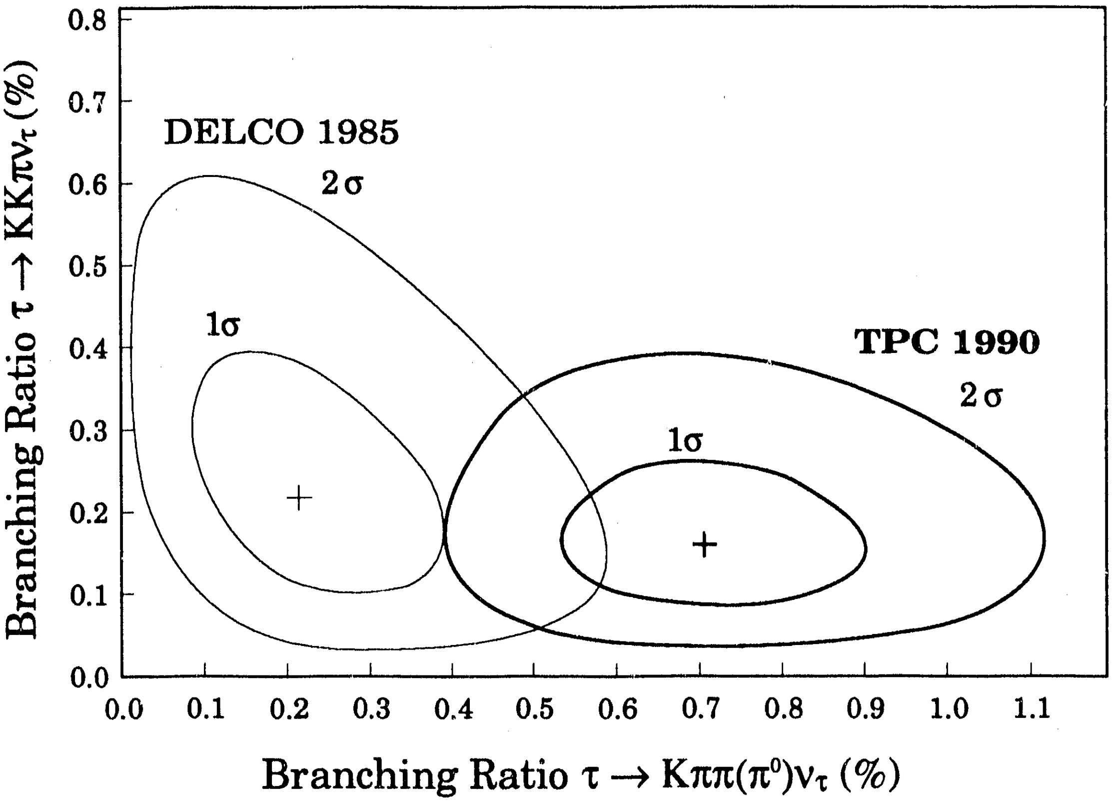

Figure 6.10: Contour plot of the errors on $BR(\tau \rightarrow \nu_\tau K\pi\pi)$ and $BR(\tau \rightarrow \nu_\tau KK\pi)$. The equivalent plot for the DELCO measurement [66] is also shown.

asymmetrical, though not so highly as those of the DELCO measurement. Figure 6.10 shows the error contour for these quantities as they very from their most probable values.

6.12 Discussion

Our estimate for the branching fraction $BR(\tau \rightarrow \nu_\tau KK\pi)$ agrees with DELCO's earlier result quite closely. By contrast, our measurement of $BR(\tau \rightarrow \nu_\tau K\pi\pi)$ differs from the DELCO result by about 2σ. In addition, the sum of $K\pi\pi$ and $KK\pi$ branching fractions from Table 6.7 (0.86%) mildly violates the 1984 TPC limit (< 0.6%, 90% CL) [64]. This higher sum is significant for experiments that cannot distinguish pions from kaons; measurements of $BR(\tau \rightarrow \nu_\tau \pi\pi\pi)$ and related quantities involve the subtraction of the kaon-containing modes. If the sum of kaon-containing modes is in the neighborhood of 0.4%, where DELCO puts it, they

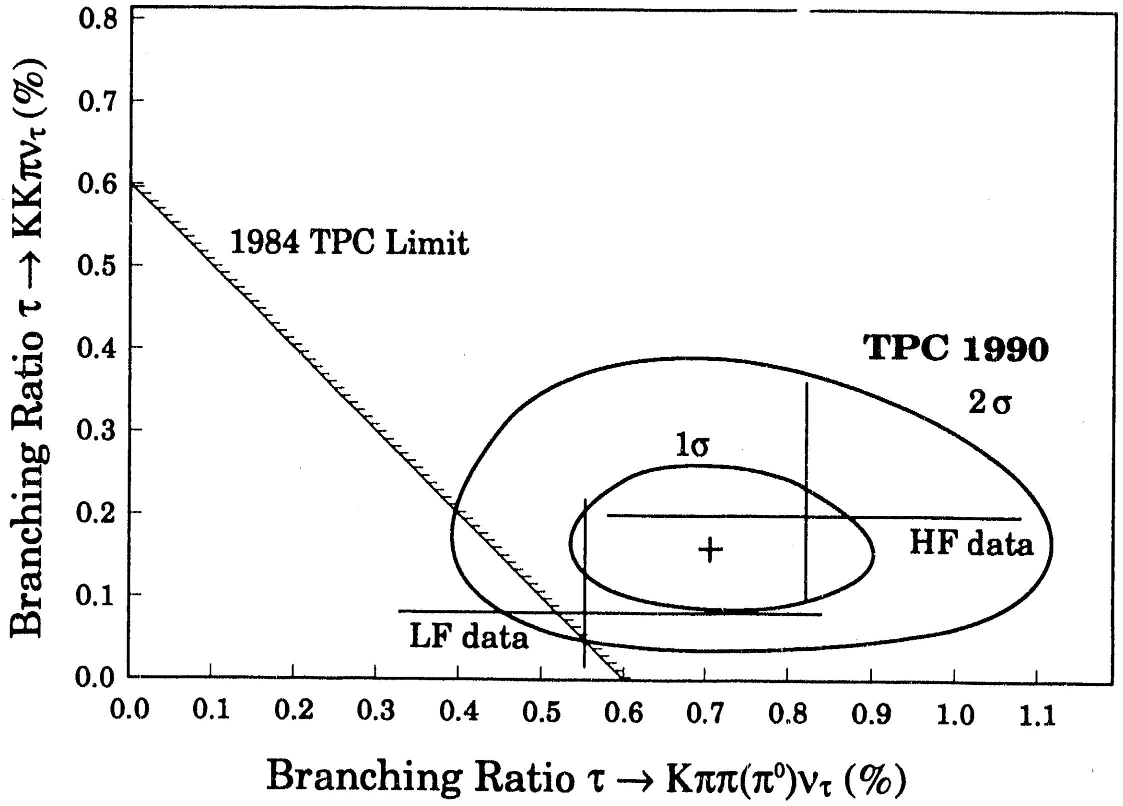

Figure 6.11: The contours of Figure 6.10 plotted with the 1984 TPC upper limit [64]. Separate branching fraction measurements for the low- and high-field data sets are also shown; the error bars represent 1σ.

can be safely ignored by many analyses. If the sum is closer to 1%, as the present analysis suggests, the kaon-containing modes represent a non-negligible fraction of three-prong decays.

Figure 6.11 shows the error contours for the current measurement together with the 1984 TPC upper limit. Also shown are 1σ error bars for branching fraction measurements based on the low-field and high-field data sets separately. The branching fractions measured with the low-field data set alone are consistent with the 1984 limit (based on the same data set, with different cuts.) The results from the high-field and low-field data sets agree with each other within errors. The low-field results are not significantly different from DELCO's. However, for both data sets the current analysis favors a branching fraction for $\tau \to \nu_\tau K\pi\pi$ closer to 0.7% than to DELCO's 0.2%.

We should recall at this point that the total number of events leading to these measurements is quite small: 28 for this analysis, 9 for DELCO's. It is hard to assign great significance to this discrepancy. It remains for higher-statistics experiments to resolve this question.

Chapter 7

Summary

THE PEP4/9 APPARATUS has tracking and charged-particle identification capabilities well suited to the study of the rare kaon-containing decays of the τ lepton. Our π/K separation at high momenta is sufficient to observe these small kaon populations, and we have sufficient data available to be sensitive to branching fractions on the order of 0.2%.

In Chapter 5 we presented an upper limit on the suppressed decay channel $\tau^- \rightarrow \nu_\tau K^- K^0_S$ by observing candidates for $K^0_S \rightarrow \pi^+\pi^-$ and noting the absence of charged kaons among the remaining three-prong tracks. The limit is

$$BR(\tau^- \rightarrow \nu_\tau K^- K^0) < 0.26\% \text{ (95\% CL)}. \tag{5.2}$$

Because the state $K\bar{K}$ is SU(3)-related to the second-class-current signature $\pi\eta$, we are able to make additional statements about the maximum allowable size of second-class currents in τ decays.

In Chapter 6 we presented new measurements of the nonzero branching ratios for the kaon-containing three-prong decay modes $\tau^- \rightarrow \nu_\tau K^- + 2$ charged + neutrals. Our measurement

$$BR(\tau^- \rightarrow \nu_\tau K^- K^+ \pi^- + \text{neutrals}) = 0.16\ ^{+0.10}_{-0.07}\,\% \tag{7.1}$$

is in good agreement with the only other existing measurement; whereas our value

$$BR(\tau^- \rightarrow \nu_\tau K^- \pi^+ \pi^- + \text{neutrals}) = 0.70\ ^{+0.20}_{-0.17}\,\% \tag{7.2}$$

is substantially higher than previously reported. In the $K\pi\pi$ channel, we see no evidence for a substantial contribution from the strange axial vector meson $K_1(1270)$.

Appendix A

Explicit Form of the Track Confusion Matrix

This Appendix presents the derivation of the explicit form of the track confusion matrix used in the matrix-inversion technique described in Section 6.4. It is important to note that the track confusion matrix $\boldsymbol{Q}$ for each track can be written down based on general knowledge of the TPC detector response, without resort to Monte Carlo calculation.

A.1 Notation

A track is measured in the TPC with momentum p_m and ionization energy loss rate I_m. The $\mathrm{d}E/\mathrm{d}x$ resolution σ_I depends both upon the details of the track measurement and on the species to which the track is assumed to belong. We therefore define the symbols σ_π and σ_K to refer to the $\mathrm{d}E/\mathrm{d}x$ resolutions calculated for the pion and kaon hypotheses, respectively. (For reasons outlined in Section 6.10, we will neglect effects associated with the momentum resolution σ_p.) The locus of expected values of I as a function of p for each species $s \in [\pi, K]$, called $I_s(p)$, is known. At a given momentum p_m the fixed distance between expected values of I for kaons and pions, expressed in units of the σ_I computed assuming the species hypothesis s, is called d_s:

$$d_s = \frac{I_K(p_m) - I_\pi(p_m)}{\sigma_s}. \tag{A.1}$$

Neglecting the effects of finite momentum resolution, the quantity χ^2 that represents the closeness of a measured point (p_m, I_m) to a species locus $I_s(p)$ is just the square of the distance from the measured $\mathrm{d}E/\mathrm{d}x$ from its expected value at the measured momentum, measured in units of $\mathrm{d}E/\mathrm{d}x$ resolution:

$$\chi^2_\pi = \frac{(I_m - I_\pi(p_m))^2}{{\sigma_\pi}^2};$$

$$\chi_K^2 = \frac{(I_m - I_K(p_m))^2}{{\sigma_K}^2}. \tag{A.2}$$

A.2 Graphical Representation of the Track Identification Criterion

Recall from Section 6.4.8 that a track is labeled as a kaon if it satisfies

$$\chi_K^2 + b^2 < \chi_\pi^2. \tag{6.18}$$

If we multiply through by $-\frac{1}{2}$ and exponentiate both sides, this becomes

$$e^{-\chi_K^2/2} e^{-b^2/2} > e^{-\chi_\pi^2/2}. \tag{A.3}$$

Insertion of Equation A.2 in this expression yields the explicit gaussian form

$$\exp\left(-\frac{(I_m - I_K(p_m))^2}{2\sigma_K^2}\right) \exp\left(-\frac{b^2}{2}\right) > \exp\left(-\frac{(I_m - I_\pi(p_m))^2}{2\sigma_\pi^2}\right). \tag{A.4}$$

These gaussians in I_m represent (unnormalized) probability density functions for the distributions of ionization measurements around the expected values for the two species hypotheses.

Figure A.1 gives a graphical representation of the kaon identification criterion. The ordinate is the $\mathrm{d}E/\mathrm{d}x$ variable I_m. Two gaussians are shown, one centered at I_π and the other at I_K. The kaon gaussian is diminished in height by a factor $e^{-b^2/2}$. Equation A.4 shows that the track will be identified as a kaon if the smaller kaon gaussian is higher at the measured $\mathrm{d}E/\mathrm{d}x$ value I_m. The shaded area, normalized to the area under the pion curve, represents the probability that a true pion will be misidentified as a kaon by this criterion.

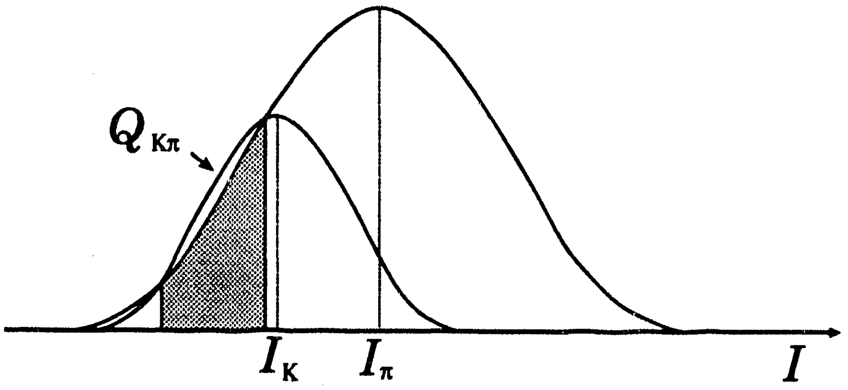

Figure A.1: Graphical representation of kaon identification criterion.

A.3 Evaluation of the Track Confusion Probabilities

The probability that a true pion will be called a kaon by criterion 6.18, called $Q_{K\pi}$ in the notation of Chapter 6, is expressible as an integral over a one-dimensional gaussian probability distribution:

$$Q_{K\pi} = P(\pi \to K) = \frac{1}{\sqrt{2\pi}\sigma_\pi} \int_{I:\chi_\pi^2 > \chi_K^2 + b^2} dI\, e^{-(I-I_\pi)^2/2\sigma_\pi^2} \tag{A.5}$$

The limits of the integral A.5 are the solutions of

$$\frac{(I_m - I_K(p_m))^2}{\sigma_K^2} + b^2 = \frac{(I_m - I_\pi(p_m))^2}{\sigma_\pi^2} \tag{A.6}$$

If we change the variable of integration to $z = (I - I_\pi)/\sqrt{2}\sigma_\pi$ and make use of the variable d_π defined in A.1 above, the limits are the solutions of

$$\frac{\sigma_\pi^2}{\sigma_K^2}(z - \frac{d_\pi}{\sqrt{2}})^2 + \frac{b^2}{2} = z^2 \tag{A.7}$$

or

$$\left(1 - \frac{\sigma_K^2}{\sigma_\pi^2}\right) z^2 - \sqrt{2} d_\pi z + \left(\frac{b^2}{2}\frac{\sigma_K^2}{\sigma_\pi^2} + \frac{d_\pi^2}{2}\right) = 0. \tag{A.8}$$

The roots are

$$z_\pm = \frac{d_\pi}{\sqrt{2}\left(1 - \frac{\sigma_K^2}{\sigma_\pi^2}\right)} \left[1 \pm \frac{\sigma_K}{\sigma_\pi}\sqrt{1 - \left(1 - \frac{\sigma_K^2}{\sigma_\pi^2}\frac{b^2}{d_\pi{}^2}\right)}\right]. \tag{A.9}$$

From Equation A.9 it is clear that there is no root if

$$\left(1 - \frac{\sigma_K^2}{\sigma_\pi^2}\right) > \frac{d_\pi^2}{b^2}. \tag{A.10}$$

This is the situation shown in Figure A.2(a), in which the pion and kaon gaussians are sufficiently close, and the kaon curve sufficiently diminished, that the height of the kaon curve never exceeds the height of the pion curve. No such track will ever be called a kaon.

A general property of quadratic equations of the form $ax^2 + bx + c = 0$ is that the product of the roots is equal to c/a. The coefficients derived from Equation A.8 give

$$z_+ z_- = \frac{b^2\frac{\sigma_K^2}{\sigma_\pi^2} + d_\pi^2}{2\left(1 - \frac{\sigma_K^2}{\sigma_\pi^2}\right)}. \tag{A.11}$$

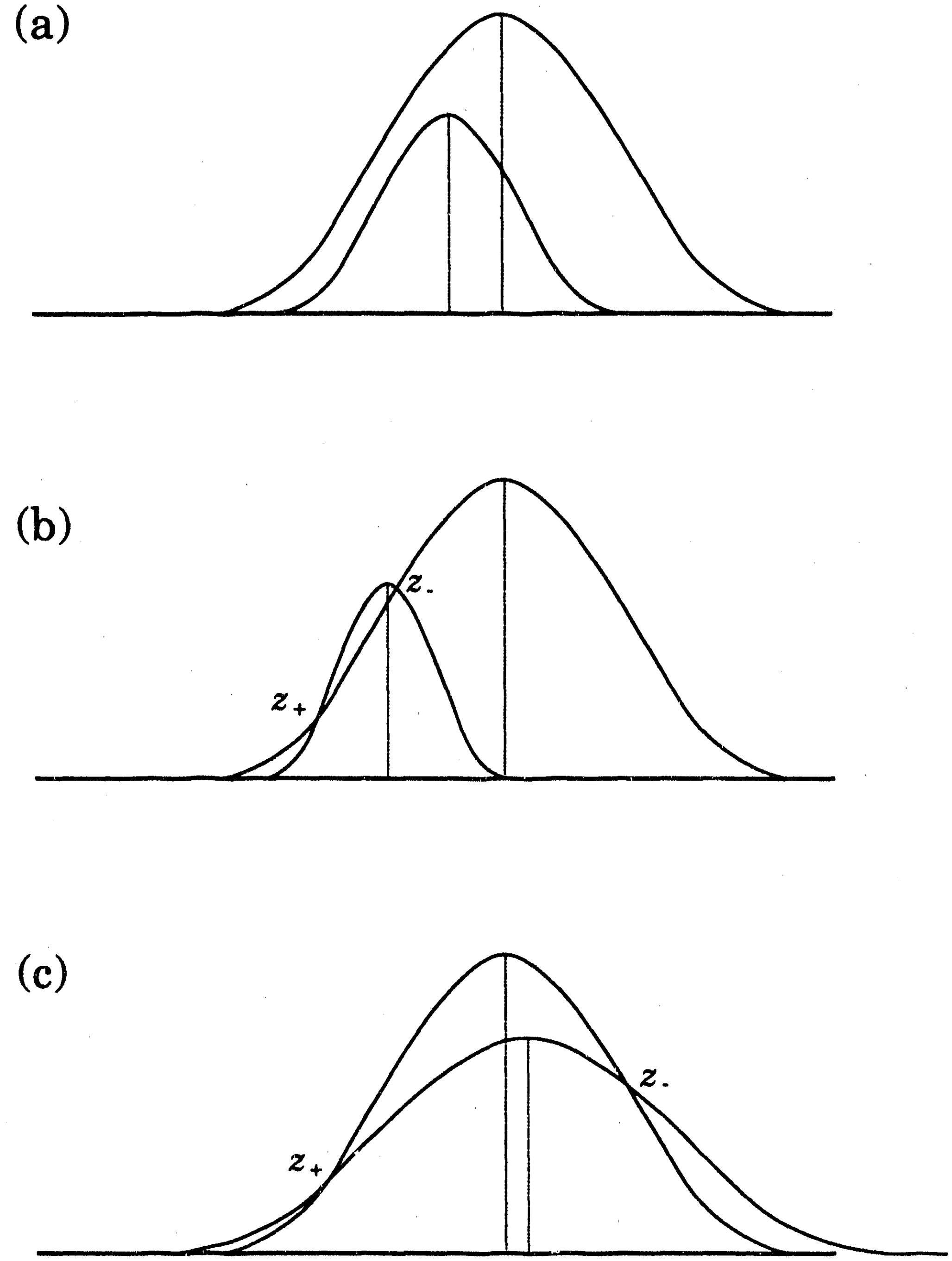

Figure A.2: Three possible configurations in confusion space. (a) No root exists; all tracks are called kaons. (b) $I_\pi > I_K$; both roots have the same sign. (c) $I_\pi < I_K$; the two roots have opposite sign.

The sign of this expression is controlled by the denominator. The absolute $\mathrm{d}E/\mathrm{d}x$ resolution scales with $\mathrm{d}E/\mathrm{d}x$ itself, so $\sigma_K/\sigma_\pi = I_K/I_\pi$. Then Equation A.11 shows that if $I_\pi > I_K$, both roots have the same sign, whereas if $I_\pi < I_K$, the two roots have opposite sign, provided the roots exist. These configurations are illustrated in Figure A.2 (b) and (c).

Figure A.2 (b) illustrates an uncomfortable situation: in the region to the left of the root z_+, tracks are called pions even though they are farther from the pion centroid than from the kaon centroid. In practice the statistics of this experiment are insufficient to populate the extreme gaussian tails, and the contribution of regions such as these to the integrals is negligible.

In the case $I_K > I_\pi$, the probability integral is broken into two intervals:

$$Q_{K\pi} = P(\pi \to K) = \frac{1}{\sqrt{2\pi}}\left(\int_{-\infty}^{z_+} + \int_{z_-}^{\infty}\right) dI\, e^{-z^2} \tag{A.12}$$

or, making use of the definition of the complementary error function erfc,

$$Q_{K\pi} = \tfrac{1}{2}\mathrm{erfc}\,(z_-) + \tfrac{1}{2}\mathrm{erfc}\,(-z_+). \tag{A.13}$$

The forms for the case $I_K < I_\pi$ and for the track confusion matrix element $Q_{\pi K} = P(K \to \pi)$ follow in a similar manner and are given explicitly in the next section.

A.4 Results

The probability that a true pion will be called a kaon by criterion 6.18 is

$$Q_{K\pi} = P(\pi \to K) = \begin{cases} \tfrac{1}{2}\mathrm{erfc}\,(z_-) + \tfrac{1}{2}\mathrm{erfc}\,(-z_+) & (I_K(p_m) > I_\pi(p_m)) \\ \tfrac{1}{2}\mathrm{erfc}\,(z_+) - \tfrac{1}{2}\mathrm{erfc}\,(z_-) & (I_K(p_m) < I_\pi(p_m)) \end{cases} \tag{A.14}$$

where

$$z_\pm = \frac{d_\pi}{\sqrt{2}\left(1 - \frac{\sigma_K^2}{\sigma_\pi^2}\right)}\left[1 \pm \frac{\sigma_K}{\sigma_\pi}\sqrt{1 - \left(1 - \frac{\sigma_K^2}{\sigma_\pi^2}\frac{b^2}{{d_\pi}^2}\right)}\right] \tag{A.9}$$

and

$$d_\pi = \frac{I_K - I_\pi}{\sigma_\pi}. \tag{A.15}$$

The probability that a true kaon will be called a pion is

$$Q_{\pi K} = P(K \to \pi) = \begin{cases} \tfrac{1}{2}\mathrm{erfc}\left(z'_-\right) - \tfrac{1}{2}\mathrm{erfc}\left(z'_+\right) & (I_\pi(p_m) > I_K(p_m)) \\ \tfrac{1}{2}\mathrm{erfc}\left(z'_+\right) - \tfrac{1}{2}\mathrm{erfc}\left(-z'_-\right) & (I_\pi(p_m) < I_K(p_m)) \end{cases} \tag{A.16}$$

where

$$z'_\pm = \frac{d_K}{\sqrt{2}\left(1 - \frac{\sigma_\pi^2}{\sigma_K^2}\right)}\left[1 \pm \frac{\sigma_\pi}{\sigma_K}\sqrt{1 + \left(1 - \frac{\sigma_\pi^2}{\sigma_K^2}\frac{b^2}{{d_K}^2}\right)}\right] \tag{A.17}$$

and

$$d_K = \frac{I_\pi - I_K}{\sigma_K}. \tag{A.18}$$

Appendix B

Covariance Matrix

This section derives the form of the covariance matrix for the matrix-inversion unfolding procedure outlined in Section 6.4.

B.1 Notation

$\boldsymbol{N}$ represents the eight-element vector of true branching mode populations. $\boldsymbol{M}^a$ is the vector containing the observed branching mode for event a. $\boldsymbol{P}^a$ is the 8×8 event confusion matrix defined by Equation 6.10. $\widehat{\boldsymbol{N}}$, the estimator of $\boldsymbol{N}$, is found from

$$\widehat{N}_i = \sum_a \sum_j (P^a)^{-1}_{ij} M^a_j \tag{B.1}$$

(c.f. Equations 6.14 and 6.15).

B.2 Result

The covariance matrix connecting the quantities N_i and $N_{i'}$ is defined from

$$\mathrm{V}[N_i, N_{i'}] = \mathrm{E}[N_i N_{i'}] - \mathrm{E}[N_i]\mathrm{E}[N_{i'}]. \tag{B.2}$$

We must therefore write down the expected values of each N_i and of the arbitrary product of two elements.

For each event $\boldsymbol{P}^a$ is fixed by the measurement variables, so from Equation B.1 we have

$$\mathrm{E}[\widehat{N}_i] = \sum_a \sum_j (P^a)^{-1}_{ij} \mathrm{E}[M^a_j]. \tag{B.3}$$

Similarly for $\mathrm{E}[N_i N_{i'}]$ we have

$$\mathrm{E}[N_i N_{i'}] = \sum_a \sum_{a'} \sum_j \sum_{j'} (P^a)^{-1}_{ij} (P^{a'})^{-1}_{i'j'} \mathrm{E}[M^a_j M^{a'}_{j'}] \tag{B.4}$$

We assume that there is no correlation between events. Then

$$\mathrm{E}[M_j^a M_{j'}^{a'}] = \delta_{aa'}\mathrm{E}[M_j^a M_{j'}^a] \tag{B.5}$$

and

$$\mathrm{E}[N_i N_{i'}] = \sum_a \sum_j \sum_{j'} (P^a)^{-1}_{ij} (P^a)^{-1}_{i'j'} \mathrm{E}[M_j^a M_{j'}^a] \tag{B.6}$$

The elements of $\boldsymbol{M}$ come from a Poisson distribution, and therefore obey

$$\mathrm{E}[M_j^a M_{j'}^a] = \mathrm{E}[M_j^a]\mathrm{E}[M_{j'}^a] + \delta_{jj'}\mathrm{E}[M_{j'}^a] \tag{B.7}$$

Then Equation B.6 becomes

$$\mathrm{E}[N_i N_{i'}] = \sum_a \sum_j \sum_{j'} (P^a)^{-1}_{ij} (P^a)^{-1}_{i'j'} \left[\mathrm{E}[M_j^a]\mathrm{E}[M_{j'}^a] + \delta_{jj'}\mathrm{E}[M_{j'}^a]\right]. \tag{B.8}$$

The covariance matrix is then

$$\begin{aligned} \mathrm{V}[N_i, N_{i'}] &= \mathrm{E}[N_i N_{i'}] - \mathrm{E}[N_i]\mathrm{E}[N_{i'}] \\ &= \sum_a \sum_j \sum_{j'} (P^a)^{-1}_{ij} (P^a)^{-1}_{i'j'} \delta_{jj'} \mathrm{E}[M_{j'}^a] \\ &= \sum_a \sum_j (P^a)^{-1}_{ij} (P^a)^{-1}_{i'j} \mathrm{E}[M_j^a] \end{aligned} \tag{B.9}$$

This is the form that is used in the calculations in Chapter 6.

Bibliography

[1] S.L. Glashow. *Nucl. Phys.* **22**, 579 (1961).

[2] S. Weinberg. *Phys. Rev. Lett.* **19**, 1264 (1967).

[3] A. Salam. In N. Svartholm, editor, *Proceedings of the Eighth Nobel Symposium*, page 367, New York, 1968. Wiley Interscience.

[4] G.S. Abrams *et al.* *Phys. Rev. Lett.* **63**, 724 (1989).

[5] M. Aguilar-Benitez *et al.* *Review of Particle Properties. Phys. Lett. B* **239**, 1 (1990).

[6] M.L. Perl *et al.* *Phys. Rev. Lett.* **35**, 1489 (1975).

[7] R. Brandelik *et al.* *Phys. Lett.* **73B**, 109 (1978).

[8] J. Kirkby. In T. Kirk and H. Abarbanel, editors, *Proceedings of the 1979 International Symposium on Lepton and Photon Interactions at High Energies*, page 107, Batavia, IL, 1979.

[9] W. Bartel *et al.* *Phys. Lett.* **161B**, 188 (1985).

[10] K.G. Hayes *et al.* *Phys. Rev. D* **25**, 2869 (1982).

[11] S. Keh *et al.* *Phys. Lett.* **B212**, 123 (1988).

[12] N. Ushida *et al.* *Phys. Rev. Lett.* **48**, 844 (1982).

[13] Y.S. Tsai. *Phys. Rev. D* **4**, 2821 (1971).

[14] B.G. Bylsma *et al.* *Phys. Rev.* **D35**, 2269 (1987).

[15] F.J. Gilman and S.H. Rhie. *Phys. Rev. D* **31**, 1066 (1985).

[16] W.J. Marciano and A. Sirlin. *Phys. Rev. Lett.* **61**, 1815 (1988).

[17] S. Weinberg. *Phys. Rev.* **112**, 1375 (1958).

[18] W.B. Schmidke *et al.* *Phys. Rev. Lett.* **57**, 527 (1986).

[19] W. Ruckstuhl *et al.* *Phys. Rev. Lett.* **56**, 2132 (1986).

[20] E. Fernandez *et al.* *Phys. Rev. Lett.* **54**, 1624 (1985).

[21] H. Albrecht *et al.* *Z. Physik* **C33**, 7 (1986).

[22] A. Donnachie and H. Mirzaie. *Z. Physik* **C33**, 407 (1987).

[23] S. Bityukov *et al.* *Phys. Lett.* **188B**, 383 (1987).

[24] B.C. Barish and R. Stroynowski. *Physics Reports* **157**, 3 (1988).

[25] H. Albrecht *et al.* *Phys. Lett.* **185B**, 223 (1987).

[26] M. Derrick *et al.* *Phys. Lett.* **189B**, 260 (1987).

[27] C. Daum *et al.* *Nucl. Phys.* **B187**, 1 (1981).

[28] N.A. Törnqvist. *Nucl. Phys.* **B203**, 268 (1982).

[29] T. Das, V.S. Mathur, and S. Okubo. *Phys. Rev. Lett.* **18**, 761 (1967).

[30] E.D. Commins and P.H. Bucksbaum. *Weak interactions of leptons and quarks.* Cambridge University Press, Cambridge, 1983.

[31] M. Oka and K. Kubodera. *Phys. Lett.* **90B**, 45 (1980).

[32] C. Leroy and J. Pestieau. *Phys. Lett.* **72B**, 398 (1978).

[33] R. Tegen. *Z. Phys.* **C7**, 121 (1980).

[34] A. Halprin, B.W. Lee and P. Sorba. *Phys. Rev. D* **14**, 2343 (1976).

[35] E.L. Berger and H.J. Lipkin. *Phys. Lett.* **189B**, 226 (1987).

[36] M. Derrick *et al.* *Phys. Lett.* **189B**, 260 (1987).

[37] H. Albrecht *et al.* *Z. Physik* **C41**, 405 (1986).

[38] K.G. Hayes. *Status of the tau one prong problem.* SLAC report SLAC-PUB-5061, Stanford Linear Accelerator Center, 1989. Presented at the Tau-Charm Factory Workshop, Stanford, California, May 23-27, 1989.

[39] K.G. Hayes and M.L. Perl. *A statistical study of tau decay data.* SLAC report SLAC-PUB-4471, Stanford Linear Accelerator Center, 1988. Submitted to Phys. Rev. D.

[40] William Walton Moses. *Measurement of the Inclusive Branching Fraction* $\tau^- \rightarrow \pi^-\pi^0+$ *neutral meson(s).* PhD thesis, University of California, Berkeley, December 1986.

[41] Patricia R. Burchat. *Decay of the Tau Lepton.* PhD thesis, Stanford University, February 1986. SLAC-292.

[42] H.J. Behrend *et al. Phys. Lett. B* **222**, 163 (1989).

[43] R. Fuzesy, N.J. Hadley, and P.R. Robrish. *Nucl. Instr. Meth.* **223**, 40 (1984).

[44] H. Aihara *et al. IEEE Trans. Nucl. Sci.* **NS30**, 153 (1983).

[45] P. Oddone *et al. Letter of Intent for PEP/TPC High Luminosity Running and TPC Vertex Chamber Proposal.* TPC Note TPC-LBL-85-20, Lawrence Berkeley Laboratory, 1985.

[46] M.T. Ronan *et al. Readout and Trigger Electronics for the TPC Vertex Chamber.* LBL Report LBL-24156, Lawrence Berkeley Laboratory, 1987.

[47] H. Aihara *et al. Nucl. Instr. Meth.* **217**, 259 (1983).

[48] R. I. Koda. *A Test of Quantum Electrodynamics at Small Angles Using the PEP-4 Facility.* PhD thesis, University of California, Los Angeles, 1985. UCLA-85-011.

[49] H. Aihara *et al. IEEE Trans. Nucl. Sci.* **NS30**, 67 (1983).

[50] G. Gidal, B. Armstrong, and A. Rittenberg. *Major detectors in Elementary Particle Physics.* LBL Report LBL-91 Supplement, Lawrence Berkeley Laboratory, 1985.

[51] M.T. Ronan. *The PEP-4 (TPC) Trigger System.* TPC Note TPC-LBL-87-12, Lawrence Berkeley Laboratory, 1987.

[52] J. William Gary. *Tests of Models for Parton Fragmentation in e^+e^- Annihilation.* PhD thesis, University of California, Berkeley, November 1985. LBL-20638.

[53] A. Bay *et al. Steps and Procedures in the Calibration of the Hexagonal Calorimeter.* TPC Note TPC-LBL-90-01, Lawrence Berkeley Laboratory, 1990.

[54] S. Kaye. *The* TPC *Production Manager: An automated offline data flow system.* TPC Note TPC-LBL-87-04, Lawrence Berkeley Laboratory, 1987.

[55] Glen Douglas Cowan. *Inclusive $\pi^\pm$, $K^\pm$, and p, $\bar{p}$ Production in e^+e^- Annihilation at $\sqrt{s} = 29$ GeV.* PhD thesis, University of California, Berkeley, January 1988.

[56] M. Suzuki. *Phys. Rev. D* **36**, 950 (1987).

[57] L. Lyons. *Statistics for Nuclear and Particle Physicists.* Cambridge University Press, Cambridge, 1986. p. 100.

[58] G. Cowan. *Particle Fractions Fitting with the TPC.* TPC Note TPC-LBL-87-07, Lawrence Berkeley Laboratory, 1987.

[59] F.A. Berends *et al. Nucl. Phys.* **B202**, 63 (1982).

[60] J.M. Yelton *et al. Phys. Rev. Lett.* **56**, 812 (1986).

[61] H. Aihara *et al. Phys. Rev. D* **35**, 1553 (1987).

[62] J.B. Gay *et al. Phys. Lett.* **63B**, 220 (1976).

[63] S. Okubo and B. Sakita. *Phys. Rev. Lett.* **11**, 50 (1963).

[64] H. Aihara *et al. Phys. Rev. D* **30**, 2436 (1984).

[65] Wei-Ming Zhang. *Measurement of Tau Branching Ratios.* PhD thesis, Johns Hopkins University, 1986.

[66] G.B. Mills *et al. Phys. Rev. Lett.* **54**, 624 (1985).

[67] W. Bacino *et al. Phys. Rev. Lett.* **41**, 13 (1978).

[68] F. James and M. Roos. *Computer Phys. Comm.* **10**, 343 (1975).

Colophon

This document was generated completely electronically. The text and tables were typeset using LaTeX on the LBL Computing Division's VAXcluster CSA. The figures were all either drawn using Adobe Illustrator on the Macintosh, or generated on the VAX from scientific data and manipulated in Illustrator. The PEP4/9 collaboration long ago standardized on SLAC's Unified Graphics System (UGS) for its VAX graphics package; I was able to extend its functionality with a device driver that delivers UGS graphics in Illustrator's dialect of PostScript. LaTeX DVI files were converted to PostScript with Andrew Trevorrow's PSPRINT driver, and the Illustrator graphics were included using a set of macros of my own design. It seems that it should be easier to do all this, but to my knowledge it isn't yet.

Thanks to Dan Crane for providing the original TOPDRAWER versions of the PEP4/9 detector drawings from Chapter 3, and to Marty Gelbaum of LBL for setting up PSPRINT on the Cluster.

END

DATE FILMED

03 / 06 / 91